UNITED NATIONS EDUCATIONAL, SCIENTIFIC AND CULTURAL ORGANIZATION
INTERNATIONAL ATOMIC ENERGY AGENCY
INTERNATIONAL CENTRE FOR THEORETICAL PHYSICS
I.C.T.P., P.O. BOX 586, 34100 TRIESTE, ITALY, CABLE: CENTRATOM TRIESTE

SMR/1006 - 31

COURSE ON "OCEAN-ATMOSPHERE INTERACTIONS IN THE TROPICS"
26 May - 6 June 1997

"Unstable & damped Equatorial Modes in Simple Coupled Ocean-Atmosphere Models"

"Dynamics of Coupled Ocean-Atmosphere Models: The Tropical Problenms"

presented by

P. CHANG
Physical Oceanography
Texas A&M University
College Station, TX
USA

Reprinted from JOURNAL OF THE ATMOSPHERIC SCIENCES, Vol. 43, No. 6, 15 March 1986
American Meteorological Society

Unstable and Damped Equatorial Modes in Simple Coupled Ocean–Atmosphere Models

ANTHONY C. HIRST

Unstable and Damped Equatorial Modes in Simple Coupled Ocean–Atmosphere Models

ANTHONY C. HIRST

Department of Meteorology, University of Wisconsin–Madison, Madison, WI 53706

(Manuscript received 20 June 1985, in final form 29 October 1985)

ABSTRACT

Free equatorial modes for several simple coupled ocean–atmosphere models are determined. They are found to include unstable and damped modes of large zonal scale and long period. The influence of ocean thermodynamics on unstable modal behavior is systematically explored. The Model I ocean features a local thermal equilibrium. In Model II, linearized temperature advection is the sole ocean thermal process. The Model III ocean features both advective and local thermal processes, while that of Model IV features only local thermal processes. The ocean and atmosphere are each represented by linear shallow water equations on the equatorial β-plane, and are linked by traditional couplings. A finite difference method with variable resolution is used to find eigenvalues and eigenvectors of the coupled systems. Key results are checked via a series method.

Ocean modes are influenced most strongly by coupling, and are damped or destabilized depending on the configuration of induced atmospheric motion relative to oceanic velocities. In Model I, the oceanic Kelvin wave is destabilized while oceanic Rossby waves are damped by the coupling. In contrast, the gravest oceanic Rossby wave is destabilized while the Kelvin wave is damped in Model II. In Model III, coupling facilitates a slowly propagating unstable mode, which has structure intermediate between the Model I unstable Kelvin wave and the Model II unstable Rossby wave. A slow, unstable mode is also present in Model IV, but the growth rate is much reduced in the absence of ocean temperature advection. Growth rates of unstable modes are dependent on a variety of model coefficients. Further experiments include arbitrary shifting and meridional restriction of the atmospheric heating field. The latter experiment provides support for a conjecture concerning the seasonal timing of El Niño.

The results are applied to the equatorial Pacific; climatological background states do not permit unstable modes that seem relevant to El Niño onset. Unstable modes permitted by a background state based on conditions observed prior to an actual El Niño are discussed.

1. Introduction

Mechanisms of tropical climate anomalies have received much attention over the past two decades. This attention results, in part, from the considerable local economic effects of tropical climate anomalies (e.g., Hastenrath and Heller, 1977) and from the awareness that tropical climate fluctuations might teleconnect to the midlatitudes (e.g., Horel and Wallace, 1981). Ocean–atmosphere interactions are often linked to the development of tropical climate anomalies; indeed, characteristics of El Niño–Southern Oscillation (ENSO) episodes suggest that these major ocean-climate disturbances may result from positive ocean–atmosphere feedback (e.g., Gill and Rasmussen, 1983). The possibility of positive ocean–atmosphere feedback warrants investigation into the dynamics of coupled ocean–atmosphere systems.

Conflicting results have been obtained from models that feature idealized ocean–atmosphere coupling and the simplest oceanic and atmospheric dynamics appropriate to the tropics. Free motions in the linear ocean-basin coupled models of Rennick (1983) and Gill (1985) are dominated by westward propagating disturbances. In contrast, motions in the coupled model of Anderson and McCreary (1985) gradually become dominated by disturbances that propagate slowly eastward. Philander et al. (1984) find that disturbances in their linear ocean-basin coupled model amplify rapidly and also propagate slowly eastward. In each of these, the system is initially perturbed and the subsequent (unforced) motion is computed numerically. Ocean thermodynamics appears to be a major determinant of model behavior. In particular, the direction in which disturbances propagate seems associated with the (assumed or determined) importance of sea surface temperature (SST) advection in the generation of SST perturbations. The perturbations in the models of Rennick (1983) and Gill (1985) result solely from advection of a prescribed background SST gradient by anomalous zonal currents. Meanwhile, SST advection does not seem to play a major role in the disturbances of Anderson and McCreary (1985), and is not even included in the local thermal equilibrium assumption of Philander et al. (1984). Atmosphere is linked to ocean in the above coupled models via parameterization of atmospheric heating in terms of the underlying SST perturbation (or total SST as in Anderson and McCreary,

1985), so the importance of ocean thermodynamics in model behavior is not surprising. The actual importance of SST advection during ENSO episodes is suggested in studies by Gill (1983) and Harrison and Schopf (1984).

It seems clear that the variety of results needs to be interpreted in terms of free modes, i.e. modes of motion permitted by the linear dynamical equations for a unforced medium. If an initial perturbation in a medium can be expressed as a sum of free modes (as is generally the case), then subsequent motion will become dominated by the free mode(s) present having the largest growth rate (or smallest decay rate). Thus disturbances observed to dominate in the aforementioned coupled models may reflect the most unstable free modes permitted by the respective linear (or linearized) equations. Analysis of the free mode structures may lead us to better understand the nature of disturbances in such simple coupled models; in particular, the role of assumed ocean thermodynamics may become clearer. None of the aforementioned coupled-model studies include a free mode analysis on the full linear or linearized equations.

In the present study, we systematically investigate the behavior of free equatorial modes in several simple coupled ocean–atmosphere models; each model features a different parameterization for ocean thermodynamics. Model I features a local thermal equilibrium (e.g. Philander, 1984). In Model II, the only permitted thermal process is temperature advection (e.g. Rennick, 1983). Model III includes temperature advection and also a parameterization of local thermal processes, and has Models I and II as extreme physical limits. Finally, we step back and consider a model (Model IV) that features only local thermal processes; it corresponds in form to a linearization of Anderson and McCreary's (1985) cyclic, unbounded model. All models in this study have both oceanic and atmospheric motions governed by the complete linear shallow-water equations on the equatorial β-plane. Models are developed in section 2, where energetics are also discussed. Methods of analysis are outlined in section 3. Basic results for the individual models are presented in section 4. Results of further experiments involving arbitrary shifting or meridional restriction of atmospheric heating are given in section 5. Further results pertinent to modal behavior in general are given in section 6. The results enable us to better understand the nature of instabilities in coupled models and the effect of simple changes in ocean thermodynamics and coupling parameterization on the stability of model waves.

2. Coupled model

The coupled system consists of a baroclinic atmosphere and an ocean mixed layer interacting via (i) wind stress and (ii) atmospheric heating parameterized in terms of the SST perturbation field.

a. The atmosphere

The simplest representation of linearized dynamics for atmospheric motion in response to a heat source $Q(x, y, t)$ is given by

$$U_t - \beta y V + \phi_x + AU = 0 \tag{1a}$$

$$V_t + \beta y U + \phi_y + AV = 0 \tag{1b}$$

$$\phi_t + c_a^2(U_x + V_y) + B\phi = Q. \tag{1c}$$

Independent variables (x, y, t) refer to eastward and northward displacement ($y = 0$ at equator) and time. Beta is the meridional gradient of the Coriolis parameter. Equations (1) represent the baroclinic mode of a two-level model if U is the difference between the upper- and lower-level zonal wind component, V similarly for the meridional wind, and ϕ the perturbation in geopotential thickness between the levels (e.g., Matsuno, 1966). This interpretation is adopted here, since latent heating in the tropics excites mainly baroclinic mode motions (Gill, 1980; Lim and Chang, 1983). Where necessary, we assume that the lower tropospheric wind (U_l, V_l) is given by $(U_l, V_l) = -(U, V)/2$.

Values of the gravity-wave speed parameter c_a quoted in the literature for the fundamental baroclinic mode range from 15 m s^{-1} (Lau, 1981) to 63 m s^{-1} (Philander et al., 1984). Most results presented herein are obtained using $c_a = 30$ m s^{-1}; some comparative studies are made using $c_a = 60$ m s^{-1}. The former value, $c_a = 30$ m s^{-1}, implies an atmospheric Rossby deformation radius of $\lambda_a = (c_a/\beta)^{1/2} = 1170$ km, while $c_a = 60$ m s^{-1} implies $\lambda_a = 1650$ km.

The processes leading to atmospheric momentum loss (e.g., surface drag, cumulus friction and lateral eddy diffusion) are parameterized by Rayleigh friction. Values quoted in the literature for the friction coefficient, A, range from 2.3×10^{-6} s^{-1} (Philander et al., 1984) to 30×10^{-6} s^{-1} (Anderson and McCreary, 1985). Most results presented herein are obtained using $A = 5 \times 10^{-6}$ s^{-1}; some comparative studies are made using $A = 10 \times 10^{-6}$ s^{-1}. The processes leading to perturbation temperature loss (e.g., lateral eddy diffusion, differential radiational cooling and surface heat exchange) are parameterized by Newtonian cooling. Results presented here generally have the cooling coefficient, B, set equal to A. Solutions where $B \neq A$ were found to be qualitatively similar to those when $B = A$ and are not presented in detail. Standard values adopted here for model coefficients are summarized in Table 1.

b. The ocean

1) MODEL DEVELOPMENT

The basic ocean model consists of a mixed layer overlying a deep, cold, quasi-motionless layer. An infinitesimally thin thermocline separates the two ocean layers. Motions and temperature are assumed constant with depth within the mixed layer. The most general

TABLE 1. Values for basic parameters in Models I–IV. Exceptions are specified in the text or captions. The nondimensional wavenumber $k = 0.106$ corresponds to a wavelength of 15 000 km.

Coefficient	Value	Coefficient	Value
A	5.0×10^{-6} s^{-1}	K_S	8.0×10^{-8} s^{-1}
B	5.0×10^{-6} s^{-1}	K_Q	7.0×10^{-3} m^2 s^{-3} K^{-1}
a	1.16×10^{-7} s^{-1}	$\bar{T}_x$ (II, III)	-5.0×10^{-7} K m^{-1}
b	1.16×10^{-7} s^{-1}	K_T (III, IV)	3.5×10^{-9} K m^{-1} s^{-1}
d (II, III, IV)	1.16×10^{-7} s^{-1}	K_E	0
c_0	1.4 m s^{-1}	β	2.2×10^{-11} m^{-1} s^{-1}
c_a	30.0 m s^{-1}	k	0.106

set of equations to be considered here for mixed layer variables is

$$u_t - \beta y v + \alpha g \Delta \bar{T} h_x + \frac{1}{2}\alpha g \bar{h} T_x + \frac{1}{2}\alpha g \bar{T}_x h + au = \tau^x/(\rho_0 \bar{h}) \quad (2a)$$

$$v_t + \beta y u + \alpha g \Delta \bar{T} h_y + \frac{1}{2}\alpha g \bar{h} T_y + av = \tau^y/(\rho_0 \bar{h}) \quad (2b)$$

$$h_t + \bar{h}(u_x + v_y) - K_E T + bh = 0 \quad (2c)$$

$$T_t + \bar{T}_x u - K_T h + dT = 0. \quad (2d)$$

The dependent variables include perturbations in thermocline depth (h), zonal (u) and meridional (v) motion, temperature (T) and zonal (τ^x) and meridional (τ^y) wind stress; $\Delta\bar{T}$ is a typical mixed layer–deep ocean temperature difference. Values and definitions of the constants ρ_0, α and g are given in Table 2.

Equations (2) result from linearization and major simplification of equations given in Appendix A, which contain more complete dynamics and explicit entrainment and surface heating terms. The most important simplifications are as follows. The assumed background state features a thermocline at the uniform depth $\bar{h}$ and a mixed layer temperature ($\bar{T}$) that may display a prescribed uniform zonal gradient ($\bar{T}_x$). All advections are neglected, with the exception of zonal temperature advection, which has been singled out in recent literature. Background motions are assumed not to affect perturbations. Finally, we follow all previously mentioned authors of coupled models and do not consider the direct effect of wind perturbations on surface heating and entrainment. Linearization of explicit entrainment and heating terms yield formulae (Appendix A) for the coefficients a, b, d, K_E and K_T in terms of background state variables. Of the above coefficients, K_T and d are found to be the most sensitive to the assumed background state and increase rapidly as $\bar{h}$ decreases. Representative values of K_T, a, b and d are given in Table 1, however, free modes are computed for a range of K_T and d.

The term $K_E T$ is found to be small relative to other terms in (2c); growth/decay rates and frequencies of modes studied here change by typically less than one percent when K_E is increased from 0 to the largest probable value (10^{-7} m K^{-1} s^{-1}). Henceforth, we set $K_E = 0$. The terms $\alpha g \bar{T}_x h/2$, $\alpha g \bar{h} T_x/2$ and $\alpha g \bar{h} T_y/2$ in (2) are also small; growth/decay rates and frequencies of modes studied here typically change by a few percent when these terms are neglected, nevertheless, the terms are retained in Models II–IV.

The characteristic speed in our ocean model, $c_0 = (\alpha g \bar{h} \Delta \bar{T})^{1/2}$, is generally set at 1.4 m s^{-1} (following Philander et al., 1984); correspondingly, we take $\bar{h} = 70$ m and $\Delta\bar{T} = 14$ K. This value of c_0 may be appropriate for conditions in the eastern equatorial Pacific, and implies an oceanic Rossby deformation radius $\lambda_0 = (c_0/\beta)^{1/2} = 250$ km, which is much smaller than that for the atmosphere. Solutions obtained here with $c_0 = 2.5$ m s^{-1} (appropriate for the first baroclinic mode in the west equatorial Pacific) are qualitatively similar to those for $c_0 = 1.4$ m s^{-1}, and are not further discussed.

Prior to analysis using the full Eqs. (2); we perform analyses using two sets of ocean equations each representing an extreme physical limit of (2). These limits are discussed in the next two subsections.

2) OCEAN MODEL I: LOCAL THERMAL EQUILIBRIUM LIMIT

In the limit where K_T and d are very large, (2d) is expected to reduce to

$$T = \kappa h \quad (3d)$$

where $\kappa = K_T/d$. This limit represents a local thermal balance and is most closely attained when the mixed layer depth is small (Appendix A). The value of κ is given as +0.03 K m^{-1}, based on a regression of SST on mixed layer depth for the far eastern Pacific as detailed in Appendix B. On neglecting the small terms $\alpha g(\bar{T}_x h + \bar{h} T_x, \bar{h} T_y)/2$, Eqs. (2a–c) become

TABLE 2. Symbols and values for physical parameters. Values for m and n follow Garwood (1977), for ν follow Anderson and McCreary (1985).

Symbol	Value	Parameter
α	2.0×10^{-4} K^{-1}	Thermal expansion coefficient of water
ρ_0	1.0×10^3 kg m^{-3}	Density of ocean water
ρ_a	1.2 kg m^{-3}	Density of surface air
C_D	1.3×10^{-3}	Drag coefficient
c_w	4.2×10^3 J kg^{-1} K^{-1}	Heat capacity of water
g	9.8 m s^{-2}	Gravitational acceleration
m	1.25	Wind mixing entrainment calibration coefficient
n	0.3	Thermal mixing entrainment calibration coefficient
ν	2.0×10^3 m^2 s^{-1}	Momentum eddy diffusion coefficient

$$u_t - \beta y v + \alpha g \Delta \bar{T} h_x + a u = \tau^x/\rho_0 \bar{h} \quad (3a)$$

$$v_t + \beta y u + \alpha g \Delta \bar{T} h_y + a v = \tau^y/\rho_0 \bar{h} \quad (3b)$$

$$h_t + \bar{h}(u_x + v_y) + bh = 0. \quad (3c)$$

Equations (1) and (3) comprise Model I, a model identical in form to that of Philander et al. (1984).

3) Ocean Model II: Thermal advection limit

In the limit when $K_T \to 0$ and d remains positive, (2d) reduces to

$$T_t + \bar{T}_x u + dT = 0. \quad (4)$$

Thus SST perturbations (T) result solely from advection by the perturbation current. This limit is most closely attained in general when the mixed layer depth is large and $\bar{T}_x \neq 0$. Equation (4) has the same form as Rennick's (1983) thermodynamic equation. Equations (1), (2a–c) and (4) comprise Model II. Values for the coefficients are given in Table 1. The value of $\bar{T}_x$ is set at 5 K per 10 000 km, typical of the equatorial Pacific (Reynolds, 1982).

4) Ocean Model III: General thermodynamic case

The full Eqs. (1) and (2) comprise Model III. Here SST perturbations result from zonal advection, entrainment and surface heat fluxes; thus Model III has thermodynamics intermediate between Models I and II. Solutions are found for a range of K_T and d, with $\bar{T}_x = -5 \times 10^{-7}$ K m^{-1}. Values for the other coefficients are given in Table 1.

5) Ocean Model IV: Local thermal forcing

Equations for Model IV are as for Model III, except that $\bar{T}_x = 0$. Model IV is expected to have Model I as an extreme physical limit when K_T and d are large.

c. *Windstress and latent heating parameterization*

Perturbation windstress and latent heating are parameterized in terms of atmospheric variables according to the traditional simple assumptions (e.g., Philander et al., 1984):

$$(\tau^x, \tau^y)/(\rho_0 \bar{h}) = -K_S(U, V) \quad (5)$$

$$Q = K_Q T. \quad (6)$$

Solutions are determined for a range of K_Q and K_S; representative values are estimated as discussed later. A value for K_S is estimated using the bulk aerodynamic formula

$$\tau^x \sim \rho_a C_D |\bar{U}_l + U_l|(\bar{U}_l + U_l) - \bar{\tau}^x$$

$$\sim 2\rho_a C_D |\bar{U}_l| U_l = -\rho_a C_D |\bar{U}_l| U.$$

Symbols have their usual meanings and standard values (Table 2); a typical equatorial surface wind speed $|\bar{U}_l| = 4$ m s^{-1}, and $\bar{h} = 70$ m. Thus $K_S = (\rho_a C_D |\bar{U}_l|)/(\rho_0 \bar{h}) = 8 \times 10^{-8}$ s^{-1}, this value being a factor of six smaller than that used by Philander et al. (1984). Estimation of K_Q is more complicated and involves an empirical study of latent heating versus SST, as outlined in Appendix 2. The relationship between latent heating and SST is found to be rather nonlinear; the estimated value of K_Q increases with background SST from 2×10^{-3} m^2 s^{-3} K^{-1} at 26.5°C to 11×10^{-3} m^2 s^{-3} K^{-1} at 29°C. We take $K_Q = 7.0 \times 10^{-3}$ m^2 s^{-3} K^{-1} to be a "representative" value, this value being similar to that of Philander et al. (1984).

An atmospheric model similar to (1) was found by Zebiac (1982) to respond realistically to observed SST anomaly patterns when the large values $K_Q = 150 \times 10^{-3}$ m^2 s^{-3} K^{-1}, $A = B = 15 \times 10^{-6}$ s^{-1} and $c_a = 63$ m s^{-1} are assumed, together with an advecting background wind $\bar{U} = -4$ m s^{-1}. Results determined for these values of K_Q, A, B and c_a are qualitatively similar to results presented in section 4 here and are not further discussed.

d. *Energetics*

Interpretation of modal behavior is aided by an analysis of perturbation energetics. The amount of energy associated with a wavelike perturbation is indicated by an integration of the local perturbation energy over a zonal wavelength and from $y = -\infty$ to $y = +\infty$. A variable $V(x, y, t)$ thus integrated is denoted $\langle V \rangle(t)$.

A quantity proportional to the local perturbation energy for the model atmosphere (1) is $E_a = (U^2 + V^2 + \phi^2/c_a^2)/2$; Eqs. (1) yield

$$\frac{d\langle E_a \rangle}{dt} = \langle \phi Q \rangle / c_a^2 - A\langle U^2 \rangle - A\langle V^2 \rangle - B\langle \phi^2 \rangle / c_a^2. \quad (7)$$

The last three terms on the right-hand side (rhs) of (7) result from prescribed damping and always contribute negatively toward $d\langle E_a \rangle/dt$. The sign of the first term on the rhs of (7) depends on the correlation between the thickness (ϕ) and the latent heating (Q); the atmospheric perturbation gains energy only if strongest latent heating occurs in regions of warm air.

A quantity proportional to local perturbation energy for the Model I ocean (3) is $E_0^{\mathrm{I}} = [u^2 + v^2 + (\alpha g \Delta \bar{T}/\bar{h})h^2]/2$; Eqs. (3) yield (Yamagata, 1985)

$$\frac{d\langle E_0^{\mathrm{I}} \rangle}{dt} = \frac{\langle u\tau^x \rangle}{\rho_0 \bar{h}} + \frac{\langle v\tau^y \rangle}{\rho_0 \bar{h}} - a\langle u^2 \rangle - a\langle v^2 \rangle - \frac{\alpha g \Delta \bar{T}}{\bar{h}} b\langle h^2 \rangle. \quad (8)$$

The last three terms on the rhs of (8) result from prescribed damping and always contribute negatively to-

ward $d\langle E_0^{\mathrm{I}}\rangle/dt$. The sign of the first two terms depends on the correlation between the ocean current velocity and windstress; the oceanic perturbation gains energy only if the windstress (or surface wind) is generally in the same direction as oceanic motion.

A quantity proportional to local perturbation energy for the Model II–IV oceans is $E_0^{\mathrm{II}} = [u^2 + v^2 + (\alpha g\Delta\bar{T}/\bar{h})h^2 + \alpha gTh]/2$. An equation for $d\langle E_0^{\mathrm{II}}\rangle/dt$ derived from (2) includes current–windstress correlation and damping terms [as in (8)] and also several terms that represent ocean perturbation-background state energy transfer and do not involve atmospheric perturbations. The sum of the ocean perturbation-background state terms is small compared to that of the damping terms for all modes studied here. Thus unstable modes in Models I–IV display both a positive $\langle u\tau^x\rangle + \langle v\tau^y\rangle$ (to build the ocean perturbation) and a positive $\langle\phi Q\rangle$ (to build the atmospheric perturbation). The term $\langle\phi Q\rangle$ provides the ultimate energy source for the growing mode, since wind-stress work merely transfers energy inefficiently between ocean and atmosphere [atmospheric wind-stress work terms are subsumed within the terms $A\langle U^2\rangle$ and $A\langle V^2\rangle$ of (7)].

3. Free mode analysis

Eigenvector analyses are performed for the model equations in each of the four models. The methods of analysis for all models are similar; only that for Model I is outlined here.

Equations (1) and (3) are nondimensionalized using a length scale of $\lambda_0 = (c_0/\beta)^{1/2} = 2.5 \times 10^5$ m and a time scale of $\mu_0 = (c_0\beta)^{-1/2} = 1.8 \times 10^5$ s. The nondimensional dependent variables, here denoted by asterisks, are

$$\left.\begin{aligned}(U^*, V^*, u^*, v^*) &= (U, V, u, v)/c_0\\ (\phi^*, h^*, T^*) &= (\phi/c_0^2, h/\bar{h}, T/\bar{T})\end{aligned}\right\}.$$

All variables and coefficients in the following are nondimensional and asterisks are dropped.

Solutions are sought of the form

$$U(x, y, t) = \mathrm{Re}\{U(y)e^{i(kx-\sigma t)}\}$$

where wavenumber k is given and the complex (angular) frequency σ is an eigenvalue to be determined. The coupled system becomes

$$AU - yV + ik\phi = i\sigma U \quad (9a)$$

$$yU + AV + \phi_y = i\sigma V \quad (9b)$$

$$ikc^2U + c^2V_y + B\phi - K_Q{}^Ih = i\sigma\phi \quad (9c)$$

$$K_sU + au - yv + ikh = i\sigma u \quad (9d)$$

$$K_sV + yu + av + h_y = i\sigma v \quad (9e)$$

$$iku + v_y + bh = i\sigma h \quad (9f)$$

where $K_Q{}^I = (\kappa K_Q/\alpha g\Delta\bar{T})\mu_0$ and $c = c_a/c_0$. The boundary conditions are

$$(U, V, \phi, u, v, h, T) = 0 \quad \text{at} \quad y = \pm\infty. \quad (10$$

Methods used here to solve (9) include a finite difference method and a series method, which are outlined in subsections 3a and 3b.

Previous results relating to the eigenproblem approach for coupled models on the equatorial β-plane appear in Hirst (1985) and Yamagata (1985). For example, Yamagata uses a shooting method to solve an eigenproblem similar to that for Model I at several values of k. However Yamagata prescribes the atmosphere to be in equilibrium with the SST pattern [i.e., terms involving σ in (9a–c) are dropped], and also assumes very large values for the coefficients B (of 620×10^{-6} s^{-1}) and K_S (of 50×10^{-8} s^{-1}). Hirst (1985) computed some eigensolutions for Models I and II but assumed smaller values for the coefficients A and B ($A = B = 2.3 \times 10^{-6}$ s^{-1}) and K_Q (of 3.3×10^{-3} m^2 s^{-3} K^{-1}).

a. *Finite difference method*

Equations (9) are solved using a finite difference scheme. First, the transform $y' = \sinh^{-1}(2y)$ is made so that the grid will have higher resolution near the equator ($y = 0$). This higher resolution is desirable in order to properly resolve the oceanic equatorial waves, whose meridional scale is $\lambda_0 = 250$ km. The boundary condition (10) is replaced by

$$(U, V, \phi, u, v, h, T) = 0 \quad \text{at} \quad y' = \pm L. \quad (11)$$

Solutions for modes of low meridional index were found not to change when L was increased beyond about 4.2. We thus set $L = 4.2$.

The derivatives are approximated by centered finite differences, and, on application of the boundary condition (11) and symmetry conditions, Eqs. (9) become the linear algebraic system $\mathbf{M}_1\xi = i\sigma\xi$ where $i\sigma$ and ξ are the eigenvalues and eigenvectors to be found and $\mathbf{M}_1$ is a $(6N - 2) \times (6N - 2)$ or $(6N - 4) \times (6N - 4)$ matrix for the symmetric and antisymmetric eigenvectors respectively; N is the number of internal grid points. The QR method was used to find the eigenvalues and eigenvectors of $\mathbf{M}_1$.

Eigensolutions of $\mathbf{M}_1$ are expected to converge toward those of (9) as N increases. Tests indicating convergence are documented in Appendix C. The results in sections 4, 5 and 6 are generally obtained using the finite difference method with $N = 12$.

b. *Series method*

A series method generalized from a procedure of Philander et al. (1984) provides an alternative means of solving (9). The dependent variables in (9) are replaced by trucated series of parabolic cylinder functions, e.g.

$$U(y) = \sum_{j=0}^{N-1} U_{2j} D_{2j}(\sqrt{2}y)$$

for symmetric solutions, where U_{2j} is a coefficient and D_{2j} is a parabolic cylinder funciton of order $2j$. Parabolic cylinder functions are orthogonal, thus Eqs. (9) are transformed into a sparse set of linear algebraic equations $\mathbf{M}_2\xi = i\sigma\xi$, where $\mathbf{M}_2$ is a $6N \times 6N$ matrix and $i\sigma$ and ξ are the eigenvalues and eigenvectors to be found by the QR method.

Since the parabolic cylinder functions form a complete set, eigensolutions of $\mathbf{M}_2$ are expected to converge toward those of (9) as N increases. Tests indicating convergence are documented in Appendix C. A comparison of results obtained by the two methods indicates correct convergence, further details are in Appendix C.

4. Impact of ocean thermodynamics

In the following, results for Models I–IV are presented sequentially to demonstrate the impact of ocean thermodynamics on modes in coupled models. Attention is restricted to the effects of coupling on oceanic waves of low meridional index (n) (Matsuno, 1966) and to additional modes of simple meridional structure that exist only because of coupling. Oceanic inertia–gravity waves of $n \geq 1$ and atmospheric waves are not significantly affected by coupling in any of the models, while oceanic Rossby waves of $n \geq 3$ are not well resolved by the numerical schemes. Model parameters are henceforth given values listed in Table 1, except where otherwise specified.

Experiments demonstrate that the eigenvalues of the coupled system in all models are functions of the product of the coupling coefficients, $K_Q K_S$, when other coefficients are held constant.

a. Model I

1) Stability and dispersion

The effect of Model I ocean–atmosphere coupling on the frequency and stability of oceanic equatorial waves with a wavelength of 15 000 km ($k = 0.106$) is shown in Fig. 1. At very small $K_Q K_S$, the damping rates of all the waves are very close to the uncoupled oceanic damping rate determined by the coefficients a and b. As $K_Q K_S$ is increased, analytic continuations of the Kelvin, Yanai (i.e. mixed Rossby–gravity) and $n = 0$ inertia–gravity waves become less damped and eventually unstable. Meanwhile, those of the Rossby waves become more damped and are eventually lost when complex meridional structure prevents adequate resolution. Henceforth, the analytic continuation of, for example, the uncoupled oceanic Kelvin wave is referred to as simply the "Kelvin wave." The frequency, and thus phase speed, of all waves decrease as $K_Q K_S$ is increased; however at high values of $K_Q K_S$, the Kelvin wave frequency begins a gradual increase.

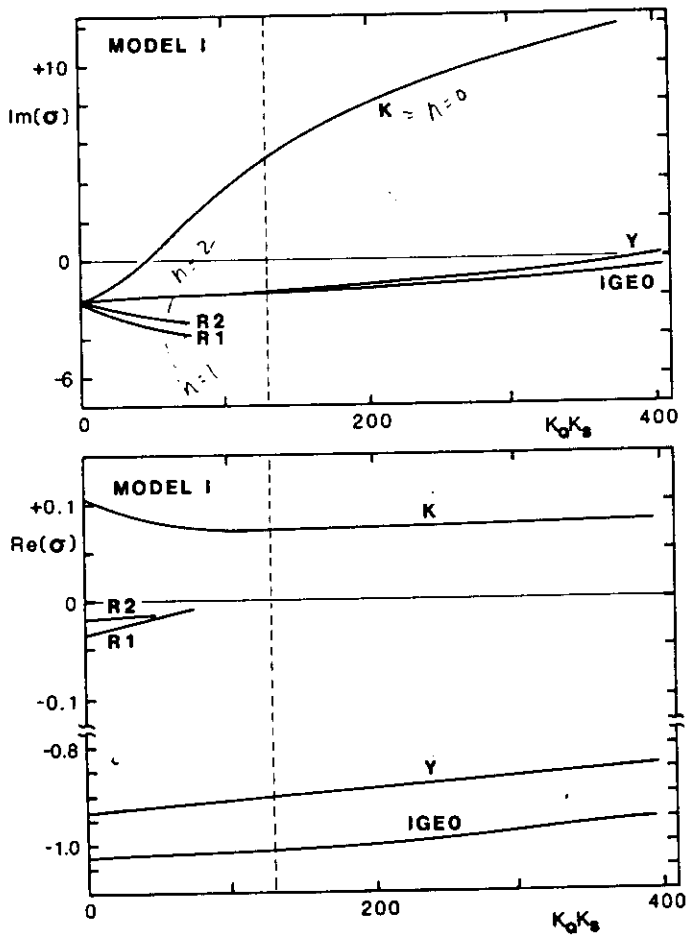

FIG. 1. Growth rates [Im(σ)] and frequencies [Re(σ)] of modes in Model I as functions of the product of coupling coefficients, $K_Q K_S$. Symbols refer to Kelvin (K), $n = 1$ Rossby (R1), $n = 2$ Rossby (R2), Yanai (Y) and $n = 0$ inertia–gravity (IGEO) waves. Im(σ) is in 10^{-2} nondimensional units, $K_Q K_S$ and Re(σ) are in nondimensional units. Im(σ) = $10^{-2} \equiv$ (208 days)$^{-1}$. Dashed line indicates representative $K_Q K_S$.

The growth rates and frequencies of the waves as a function of wavenumber k are shown in Fig. 2 for the representative value of $K_Q K_S$ (Table 1). Kelvin waves of wavelength greater than 6000 km ($k = 0.26$) are unstable, with maximum growth rates at wavelengths around 16 000 km ($k = 0.1$). No other unstable mode was detected; the stabilities of Yanai and IGEO waves (not shown) are not greatly altered and Rossby waves are highly damped, especially at shorter wavelengths. The frequencies of all waves at all wavelengths are decreased by the coupling. In particular, the Kelvin wave is now dispersive; the phase speed increases from about $0.6c_0$ at long wavelengths, where the wave is unstable, toward c_0 at shorter wavelengths.

A stability analysis for modes partly resembling Kelvin waves in a coupled model similar to Model I was performed by Lau (1981); however, he in effect assumed that meridional velocities and Coriolis accelerations are everywhere zero. Such assumptions cannot

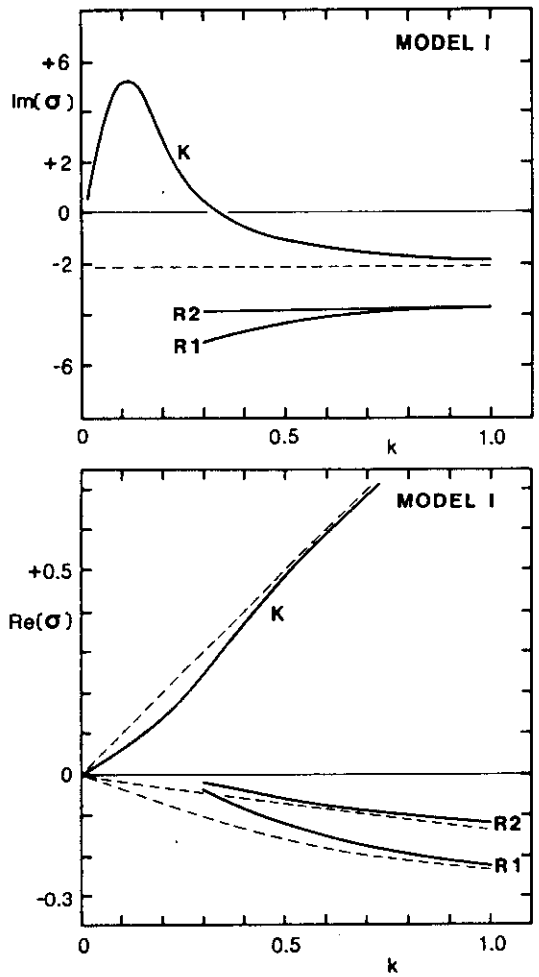

FIG. 2. Growth rates [Im(σ)] and frequencies [Re(σ)] of modes in Model I as functions of wavenumber (k). Symbols as in Fig. 1. Dashed lines indicate computed values in the absence of coupling. Im(σ) is in 10^{-2} nondimensional units, Re(σ) and k are in nondimensional units. A wavelength of 16 000 km corresponds to $k = 0.1$.

be made a priori, since heating by an ocean Kelvin wave will continuously excite atmospheric Rossby and inertia–gravity waves (Matsuno, 1966) which in turn excite higher n ocean waves. The resulting meridional velocities may be significant. Lau (1981) found that his "Kelvin" waves are unstable and stationary at sufficiently large $K_Q K_S$. The results here show that unstable Kelvin waves propagate eastward, albeit more slowly than in the absence of coupling.

The value of $K_Q K_S$ at which the destabilized Kelvin wave is neutral (i.e. Im(σ) = 0) is shown as a function of wavenumber in Fig. 3. The curve computed with $A = B = 5 \times 10^{-6}$ s^{-1} and $c_a = 30$ m s^{-1} is compared to that with $A = B = 10 \times 10^{-6}$ s^{-1} and to that with $c_a = 60$ m s^{-1} in order to determine the dependence of Kelvin wave instability on the values of these parameters. In the first case, very long Kelvin waves (wavelength 20 000 to 40 000 km) are the first to become unstable as $K_Q K_S$ is increased. The larger value of c_a inhibits instability, especially at shorter wavelengths. The larger A and B also inhibits instability, but more so at longer wavelengths. The reduction in Kelvin-wave growth rate with use of a larger c_a, A ($=B$) or k results [via (8)] from an overall reduction in atmospheric response to the oceanic wave. The reduction in atmospheric response is evidenced by smaller values for ratios such as $|U|_{max}/|u|_{max}$, and can in turn be easily explained with reference to the theory for the one layer model response to periodic forcing (Matsuno, 1966). In particular, the effects of coupling on oceanic Kelvin and Rossby modes are strongest at long wavelengths largely because the frequencies of such oceanic modes then differ least from the free frequencies of modes dominant in the atmospheric response (Kelvin and low-n Rossby waves).

Philander et al. (1984) used $c_a = 63$ m s^{-1} in their model, however their value of $K_Q K_S$ was a factor of 7 larger than that considered here. Kelvin waves with wavelength over 4000 km ($k < 0.4$) are found here to be unstable when all coefficients have values as per Philander et al. (1984) (a, b, c_0 as in Table 1, $A = 2.3 \times 10^{-6}$ s^{-1}, $B = 0.8 \times 10^{-6}$ s^{-1}). The instability seen in their model solution appears to be a destabilized oceanic Kelvin wave.

2) STRUCTURE OF FREE MODES

The reason that Model I coupling destabilizes Kelvin waves but damps $n = 1$ Rossby waves is evident in the structure of the coupled Kelvin and Rossby waves as illustrated in Figs. 4a and 4b. For both waves, the response of the atmosphere to heating is as expected (Matsuno, 1966), with equatorial westerlies at and to the west of the heat source here located at the ocean wave "crest" (i.e. maximum positive h). Since the ocean

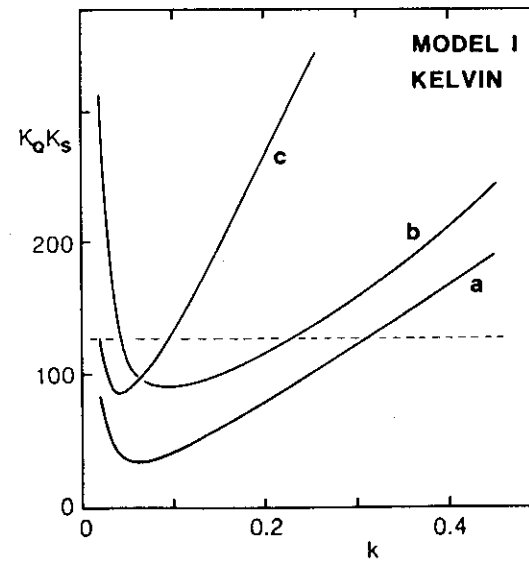

FIG. 3. Value of $K_Q K_S$ at which the Model I Kelvin wave is neutral, as a function of wavenumber k when (a) $c_a = 30$ m s^{-1} and $A = B = 5 \times 10^{-6}$ s^{-1}; (b) $c_a = 30$ m s^{-1} and $A = B = 10 \times 10^{-6}$ s^{-1}; and (c) $c_a = 60$ m s^{-1} and $A = B = 5 \times 10^{-6}$ s^{-1}. $K_Q K_S$ and k are in nondimensional units. Dashed line indicates representative $K_Q K_S$.

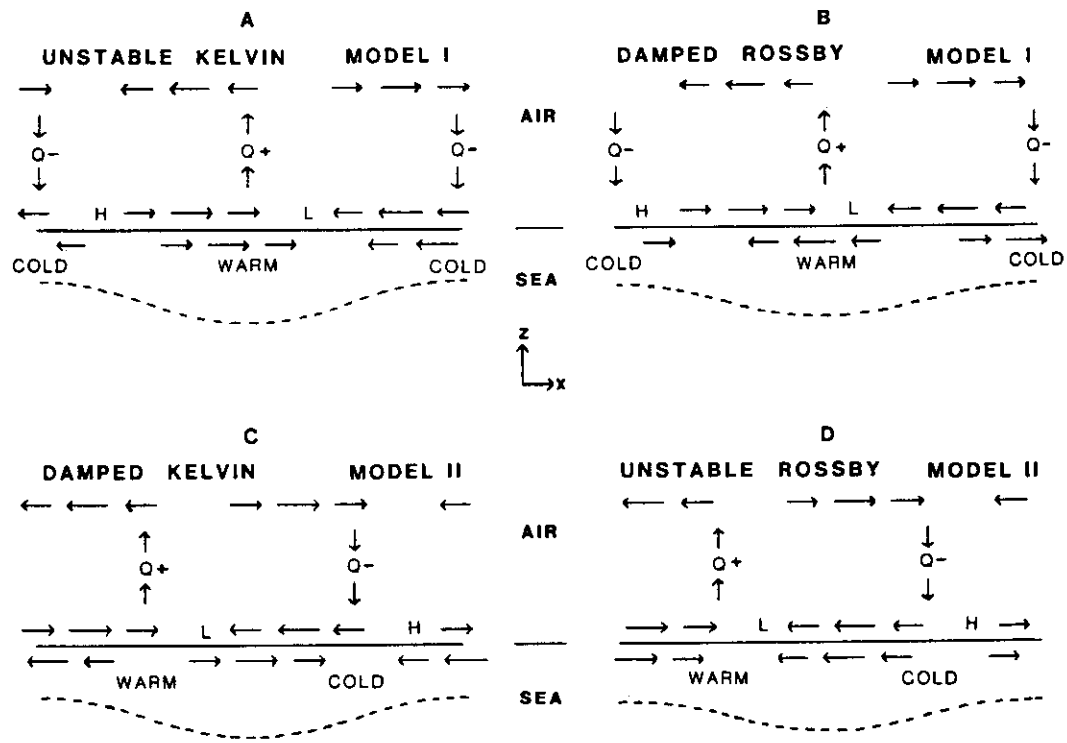

FIG. 4. Schematic illustration of equatorial motion associated with the Kelvin and $n = 1$ Rossby waves in Model I (A and B) and Model II (C and D). The solid horizontal line represents the ocean surface, the dashed curve the bottom of the mixed layer. Arrows indicate ocean current and atmospheric motion perturbations. Maximum positive and negative perturbations of SST are indicated by WARM and COLD, of atmospheric heating by $Q+$ and $Q-$, of surface atmospheric pressure by H and L, respectively.

Kelvin wave crest is associated with eastward oceanic flow, atmospheric westerlies overlie oceanic eastward motion and perturbation energy is transferred to the ocean as per Eq. (11); the oceanic Kelvin wave gains energy and grows. In contrast, equatorial westward oceanic flow coincides with the oceanic Rossby wave crest, so atmospheric westerlies overlie oceanic westward motion, and the oceanic Rossby wave loses energy and decays. More formally, a necessary condition for instability in Model I is that both $\langle \phi Q \rangle$ in (7) and $\langle u\tau^x \rangle + \langle v\tau^y \rangle$ in (8) are positive. Both waves display maximum latent heating in regions of positive thickness perturbation (i.e., low surface pressure), hence $\langle \phi Q \rangle$ is positive. However, only the Kelvin wave also displays a positive $\langle u\tau^x \rangle$ and thus satisfies the instability condition ($\langle v\tau^y \rangle$ is small in both cases).

The horizontal structures of the eastward propagating Kelvin and westward propagating Rossby waves are shown in Figs. 5a and 5b. Atmospheric perturbations extend much farther from the equator than do ocean perturbations, as expected from the disparate values of λ_0 for the two media. Atmospheric thickness perturbations exhibit a shift westward with increasing latitude; smaller values of the atmospheric damping coefficients (A, B) are associated with a larger westward shift. The uncoupled oceanic wave structures are partly retained. The tendency for equatorial currents to be shifted zonally away from the oceanic wave crest is found [via (3a)] to result from direct wind forcing; associated meridional motions cause distortion of the h field so that the equatorial zonal currents remain nearly geostrophic (i.e., "longwave balance" is nearly maintained). Meanwhile, h field distortions at $y \gtrsim 1.5$ are found to result primarily from oceanic (Ekman) pumping associated with shear in the zonal wind stress (i.e., $K_S \partial U/\partial y$). The decline in Kelvin-wave phase speed in the presence of coupling is found [via (3c)] to result from both meridional divergence in front of the ocean wave crest (Yamagata, 1985) and the westward shift in oceanic zonal motion relative to the crest; that for the $n = 1$ Rossby wave speed results mainly from reduced divergence/convergence associated with weaker zonal currents.

Maximum amplitudes of the perturbation quantities for modes illustrated in this work are given in Table 3. All values assume a modest 20 m amplitude in h. The unstable Kelvin wave of Fig. 5a displays nearly zonal oceanic motion, while atmospheric motion is stronger and features a more substantial meridional component. The "representative" values of K_Q and K_S give $|U_l|_{\max}/|u|_{\max} = 4.0$ for the unstable Kelvin wave; larger values of the ratio (K_Q/K_S) are associated with stronger relative atmospheric motion. Smaller values of the coefficient A are associated with a smaller pressure to wind ratio $|P_l|_{\max}/|U_l|_{\max}$.

Further details of unstable Kelvin wave dynamics

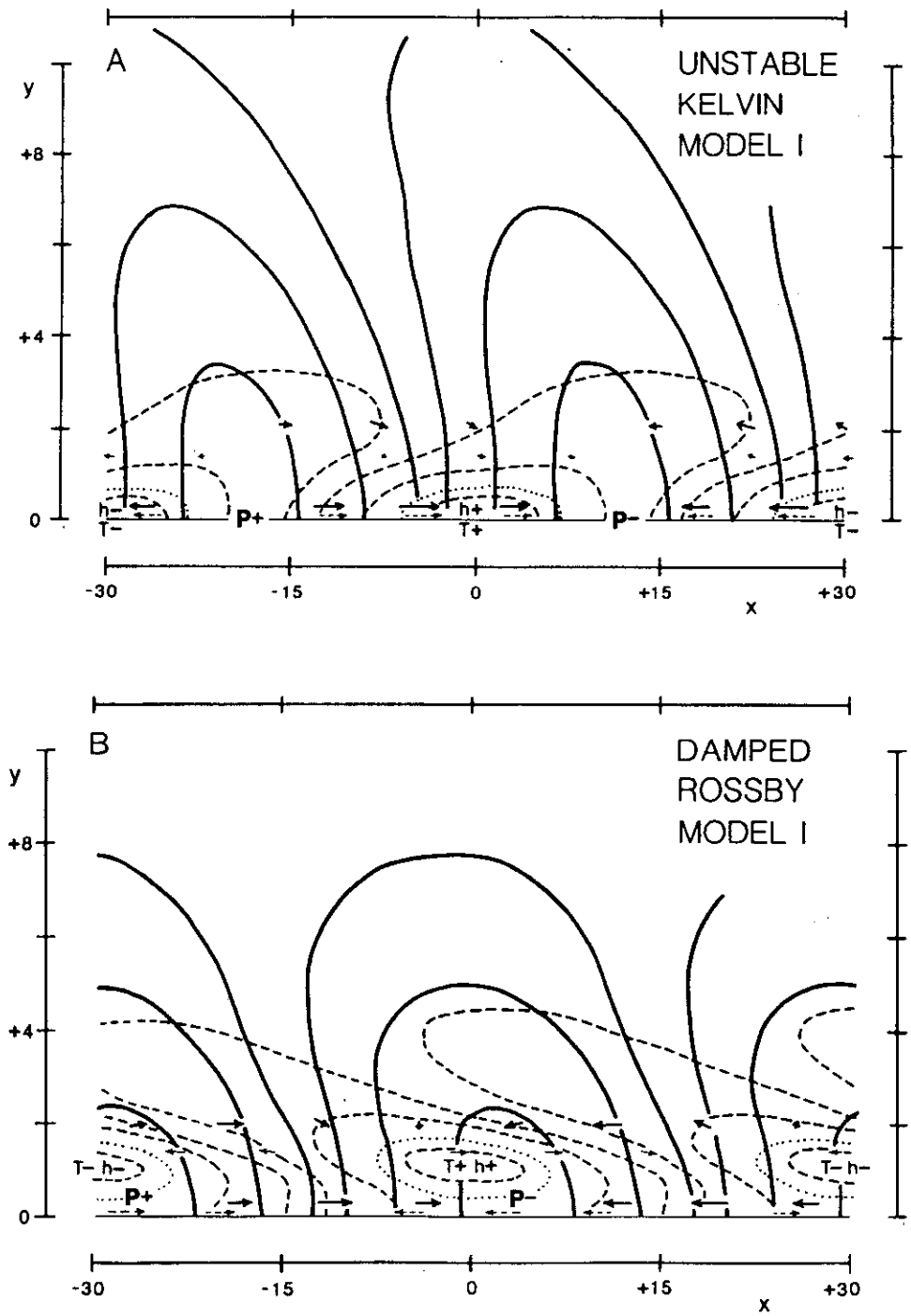

FIG. 5. Eigenfunctions for (*A*) the Kelvin and (*B*) the $n = 1$ Rossby wave, in Model I. Solid, dashed and dotted lines indicate lower tropospheric pressure (P), mixed layer depth (h) and SST (T) perturbation contours; those for P and h are at 90%, 50% and 10% and for T are at 80% of maximum values. The "+" and "−" indicate maximum positive and negative perturbations. Solid and dashed arrows indicate perturbation surface wind and ocean velocity. Coefficients and wavenumber have values as in Table 1, except that $K_Q = 2.5 \times 10^{-3}$ m^2 s^{-3} K^{-1} for the Rossby wave. One unit of nondimensional distance corresponds to 250 km.

can be gained from Table 4, which lists maximum magnitudes attained by terms in the Model I equations at selected latitudes, in association with the mode of Fig. 5a. Listed values are scaled so that the largest magnitude attained within the domain by any term of the respective equation is 100 units. Near the equator, the atmospheric pressure gradient force is nearly balanced by Rayleigh friction, but a long-wave balance is only approximately attained. Also, atmospheric divergence almost completely balances heating, as expected from the scale analysis of Zebiac (1982). Further from the equator ($y \geq 4$), the atmosphere approaches Ekman and long-wave balance, and atmospheric motion becomes more nondivergent. The atmospheric parts of

TABLE 3. Maximum values attained by perturbations associated with selected modes, when maximum h = 20 m. K, R1 and U refer to the Kelvin, n = 1 Rossby and Model III/IV unstable modes, respectively. P_l is the "lower tropospheric pressure" perturbation, defined $P_l = -\rho_a\phi/2$.

Perturbation	Model: Mode:	I K	II R1	II K	III U	IV U
T (K)		0.61	1.67	0.32	0.96	0.30
h (m)		20	20	20	20	20
u (m s^{-1})		0.50	0.87	0.39	0.56	0.26
v (m s^{-1})		0.02	0.05	0.01	0.03	0.01
U_l (m s^{-1})		1.98	2.58	1.12	2.55	1.62
V_l (m s^{-1})		0.49	0.99	0.21	0.79	0.29
P_l (mb)		0.30	0.38	0.15	0.38	0.23

all modes illustrated in this report behave similarly. The relative sizes of oceanic terms resemble those for an uncoupled Kelvin wave, near the equator. In particular, ocean motion is highly divergent and in long-wave balance. Further from the equator ($y \gtrsim 2$), the ocean approaches Ekman balance.

b. Model II

1) STABILITY AND DISPERSION

The effect of coupling on the frequency and stability of oceanic equatorial waves is displayed for Model II in Fig. 6. In contrast to Model I, the n = 1 Rossby wave is destabilized while the Kelvin wave is damped by coupling in Model II. The coupling does not significantly affect Yanai and IGEO waves. Values of σ are found to depend on the product $K_QK_s\bar{T}_x$ when other parameters are held constant and the small terms $\alpha g(\bar{T}_xh + \bar{h}T_x, \bar{h}T_y)/2$ are neglected, a dependence suggested by the simple analysis of Rennick and Haney (1985).

TABLE 4. Maximum magnitudes of terms in Eqs. (1) and (3) (nondimensionalized) at indicated nondimensional latitudes (y) in association with the Model I Kelvin wave. An asterisk indicates that the given magnitude is the maximum for that term within the domain.

y	Terms					Equation
	U_t	$-\ yV$	$+\ \phi_x$	$+\ AU$	$=\ 0$	(1a)
0	9*	0	100*	94*		
4.1	3	60*	82	30		
	V_t	$+\ yU$	$+\ \phi_y$	$+\ AV$	$=\ 0$	(1b)
1.4	2*	68	51	17*		
4.1	1	100*	95*	9		
	ϕ_t	$+\ c^2U_x$	$+\ c^2V_y$	$+\ B\phi$	$=\ K_Q\kappa h$	(1c)
0	1*	35*	86*	6*	100*	
4.1	1	11	13	5	5	
	u_t	$-\ yv$	$+\ h_x$	$+\ au$	$=\ K_sU$	(3a)
0	77*	0	74*	18*	100*	
2.0	6	44*	17	1	51	
	v_t	$+\ yu$	$+\ h_y$	$+\ av$	$=\ K_sV$	(3b)
0.9	1	99*	100*	≪1	4	
2.0	1	30	33	≪1	5	
	h_t	$+\ u_x$	$+\ v_y$	$+\ bh$	$=\ 0$	(3c)
0	67*	100*	34*	16*		
2.0	15	8	10	4		

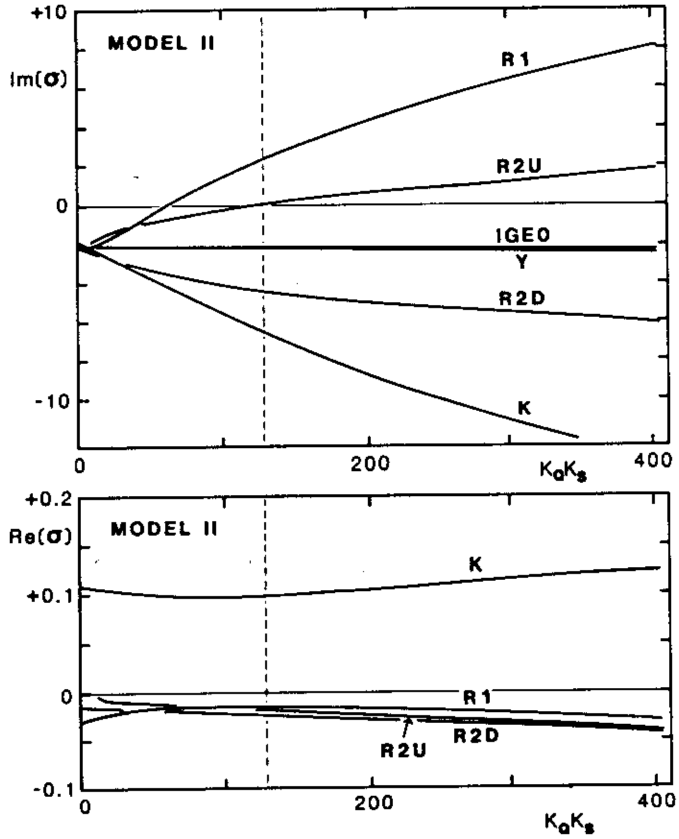

FIG. 6. Growth rates [Im(σ)] and frequencies [Re(σ)] of modes in Model II as functions of K_QK_S. Symbols "R2U" and "R2D" refer to unstable and damped "n = 2 Rossby" modes, respectively. Otherwise as for Fig. 1.

Two antisymmetric modes, whose oceanic structures partly resemble an uncoupled n = 2 Rossby wave, are present in the coupled model. One mode is destabilized and the other is damped (Fig. 6); growth/decay rates are equidistant from the uncoupled decay rate. The modes have almost identical frequencies and are referred to respectively as the unstable and damped n = 2 Rossby modes.

The growth rates and frequencies of the modes as a function of wavenumber k are displayed in Fig. 7 for the representative value of K_QK_s. The growth rate for n = 1 Rossby waves increases monotonically with wavelength. The destabilization of long n = 1 Rossby waves would explain the dominance of basinwide westward-propagating disturbances in the models of Rennick (1983) and Gill (1985). The dispersion diagram suggests that frequencies of Kelvin and Rossby modes do not tend to zero as $k \to 0$, but rather approach small nonzero values.

The effects of coupling in Model II are confined much more strongly to long low-frequency waves (Fig. 7) than in Model I (Fig. 2). This stronger confinement is associated with the use of a prognostic thermal equa-

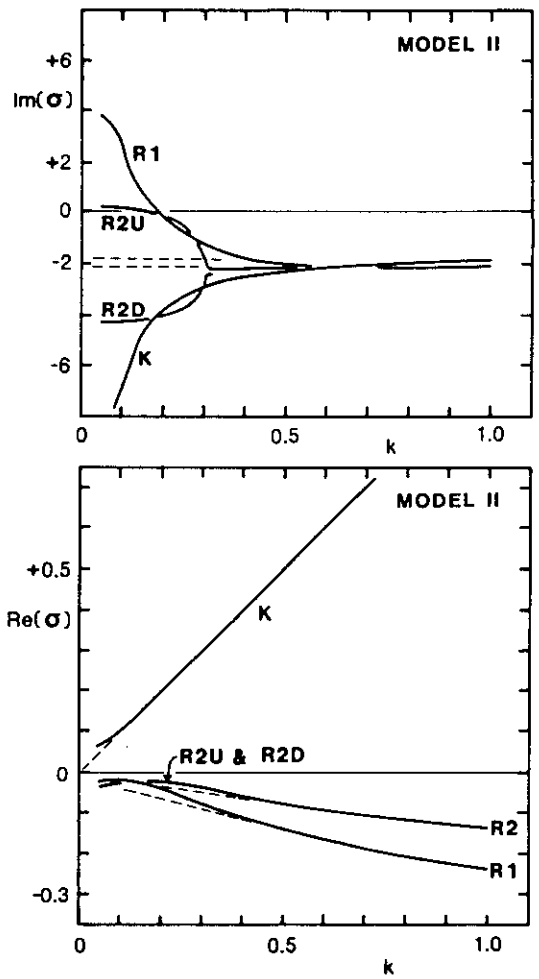

FIG. 7. As in Fig. 6 but as functions of wavenumber (k).

tion (4) instead of the thermal equilibrium assumption (3d) of Model I. Equation (4) yields $|T| = |\bar{T}_x u/(d - i\sigma)| < |\bar{T}_x u/\mathrm{Re}(\sigma)|$. It follows that SST perturbations associated with Kelvin and Rossby waves decrease as k [hence $\mathrm{Re}(\sigma)$] increases; reduced atmospheric forcing together with factors discussed for Model I lead to rapid diminution of atmospheric response and coupling effects. The high frequencies of Yanai and inertia–gravity waves likewise result in weak associated SST perturbations and atmospheric response, hence in ineffective coupling.

Figure 8 shows that larger values for A and B or c_a act to suppress instability, as in Model I. Again the larger value of c_a most suppresses instability at short wavelengths.

Free modes for Model II were also computed in the presence of an *eastward* temperature gradient ($\bar{T}_x = +5 \times 10^{-7}$ K m^{-1}), whence the coupling destabilizes Kelvin waves and damps $n = 1$ Rossby waves.

2) STRUCTURE OF FREE MODES

The marked contrast between the effects of Model I and Model II coupling on the stability of oceanic waves is easily explained with reference to the structure of the free modes illustrated in Fig. 4a–d. We first refer to Figs. 4a and 4c for the Kelvin wave in Models I and II respectively. Equatorial surface westerlies are at and to the west of the heat source (i.e. positive SST anomaly) in both cases. In Model I, the positive SST anomaly coincides with the ocean Kelvin wave crest, so atmospheric westerlies overlie oceanic eastward motion; the oceanic Kelvin wave gains energy and grows. In Model II, advection produces a positive SST perturbation centered a quarter-cycle behind the oceanic Kelvin wave crest, so the atmospheric response is shifted west and easterlies overlie the oceanic eastward motion; the oceanic Kelvin wave loses energy and decays. A similar phase shift of the SST perturbation relative to the ocean flow explains the difference in the stability of the $n = 1$ Rossby wave between Models I and II (Figs. 4b and 4d).

The horizontal structure of the eastward propagating Kelvin and westward propagating Rossby waves is shown in Figs. 9a and 9b, respectively. As in Model I, the atmospheric perturbations exhibit a shift westward with increasing latitude and the uncoupled oceanic wave structures are partly retained. Oceanic motion is shifted zonally away from the oceanic wave crests at the equator in response to direct forcing by the zonal wind. The SST perturbation associated with the Rossby mode is very narrow and falls to 50% of its equatorial value at 1.6° latitude. Such a narrow SST perturbation in this thermal advection limit is expected since the strong zonal current associated with the uncoupled Rossby wave is very narrow (Matsuno, 1966).

c. Model III

1) STABILITY AND DISPERSION

Model III [Eqs. (1) and (2)] is expected to have Models I and II as extreme physical limits. We explore the

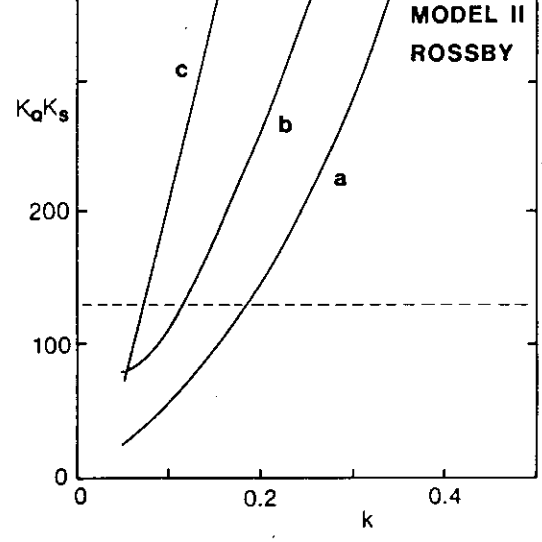

FIG. 8. Value of $K_Q K_S$ at which the $n = 1$ Rossby wave in Model II is neutral, as a function of wavenumber (k) when (a) $c_a = 30$ m s^{-1} and $A = B = 5 \times 10^{-6}$ s^{-1}; (b) $c_a = 30$ m s^{-1} and $A = B = 10 \times 10^{-6}$ s^{-1}; and (c) $c_a = 60$ m s^{-1} and $A = B = 5 \times 10^{-6}$ s^{-1}. Otherwise as for Fig. 3.

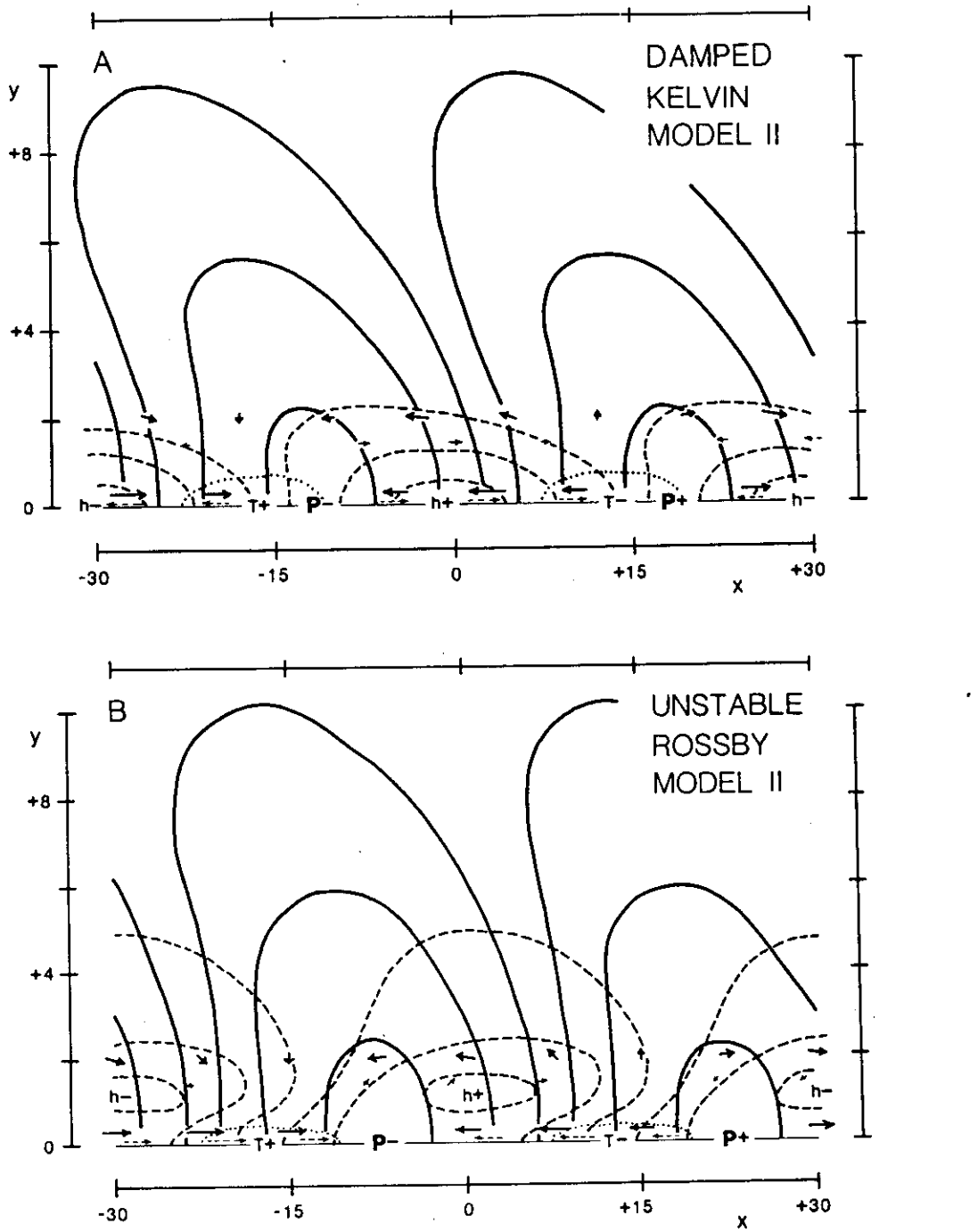

FIG. 9. As in Fig. 5 but for Model II when K_Q and K_S have "representative" values.

transition from limit to limit by determining free modes for Model III at values of (K_T, d) along the path indicated in Fig. 10. We start with very large values of K_T and d with a ratio $K_T/d = \kappa = 0.03$ K m^{-1}, i.e., the expected Model I limit. Then K_T and d are decreased while the ratio K_T/d is kept constant until $d = 1.16 \times 10^{-7}$ s^{-1} [(100 days)$^{-1}$]; d then remains fixed while K_T decreases to zero to complete the transition to the Model II limit. The value of T_x is fixed at -5×10^{-7} K m^{-1} throughout.

Changes in growth rates and frequencies of free modes along the (K_T, d) path are displayed in Fig. 11. The free modes of simple meridional structure in Model III are found to be identical to those in Model I (with the small terms $\alpha g(\bar{T}_x h + \bar{h}T_x, \bar{h}T_y)/2$ included) when $K_T \gtrsim 3 \times 10^{-5}$ K m^{-1} s^{-1} and $d \gtrsim 1 \times 10^{-3}$ s^{-1}, verifying that Model I is a physical limit of Model III. The behavior of free modes in Model III remain similar to that in Model I while K_T and d are larger than 3×10^{-8} K m^{-1} s^{-1} and 1×10^{-6} s^{-1} respectively (Fig. 11a); these values of K_T and d are still larger than the largest probable values (Appendix A). For smaller K_T and d, the phase speed of the unstable (ex-Kelvin) mode slows dramatically and the growth rate decreases slightly. Further, a highly damped mode becomes apparent, whose oceanic part resembles a Kelvin wave.

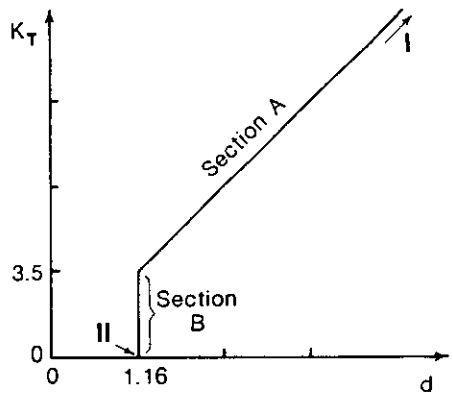

FIG. 10. (K_T, d) path at points along which free modes are determined for Model III, in order to illustrate the transition from the Model I limit (I) to the Model II limit (II). K_T has units 10^{-9} K m^{-1} s^{-1}, d has units 10^{-6} s^{-1}.

As K_T is decreased toward zero while $d = 1.16 \times 10^{-6}$ s^{-1} (Fig. 11b), the unstable mode becomes stationary, then acquires a westward phase speed and becomes the unstable $n = 1$ Rossby wave of Model II. Thus the unstable mode of Model III is analytically related to the principal unstable mode in both Models I and II. However the latter relationship is found to exist only at long wavelengths ($k < 0.12$); when $0.13 < k < 0.2$ both the Model III unstable mode and a destabilized $n = 1$ Rossby wave are present for a range of small K_T. The highly damped mode noted before is analytically related to the damped Kelvin wave of Model II. Both $n = 2$ Rossby modes of Model II are lost as K_T is increased (Fig. 11b); meridional structures become too complicated for adequate resolution.

The behavior of Model III free modes at the corner point ($K_T = 3.5 \times 10^{-9}$ K m^{-1} s^{-1}, $d = 1.16 \times 10^{-6}$ s^{-1}) are displayed in Figs. 12 and 13. This value of (K_T, d) is within the range of values estimated for the tropical Pacific (Appendix A). Figure 12 shows that the unstable mode depends on strong ocean–atmosphere coupling for its existence; all ocean waves present when $K_Q K_S = 0$ are damped by coupling. The highly damped mode noted in Fig. 11a is a damped Kelvin wave. Coupling has very little effect on the oceanic Yanai and $n = 0$ inertia–gravity waves. Figure 13 shows that coupling is most effective at long wavelengths; the unstable mode does not exist at short wavelengths. The frequency of the unstable mode is very low over all the wavelengths at which it exists; eastward propagation is indicated at wavelengths between 4000 km ($k = 0.4$) and 20 000 km, with westward propagation at longer wavelengths.

2) STRUCTURE OF FREE MODES

The horizontal structure of the eastward-propagating unstable mode in Model III is shown in Fig. 14, and as expected it appears to be transitional between the Model I Kelvin wave (Fig. 5a) and the Model II $n = 1$ Rossby wave (Fig. 9b). Both the advective and the $-K_T h$ terms in (2d) contribute toward positioning the positive SST perturbation to the west of the maximum h perturbation; the advective term provides the larger thermal forcing ($|\bar{T}_x u|/|K_T h| \sim 4$). The associated atmospheric pressure and wind patterns are similarly shifted

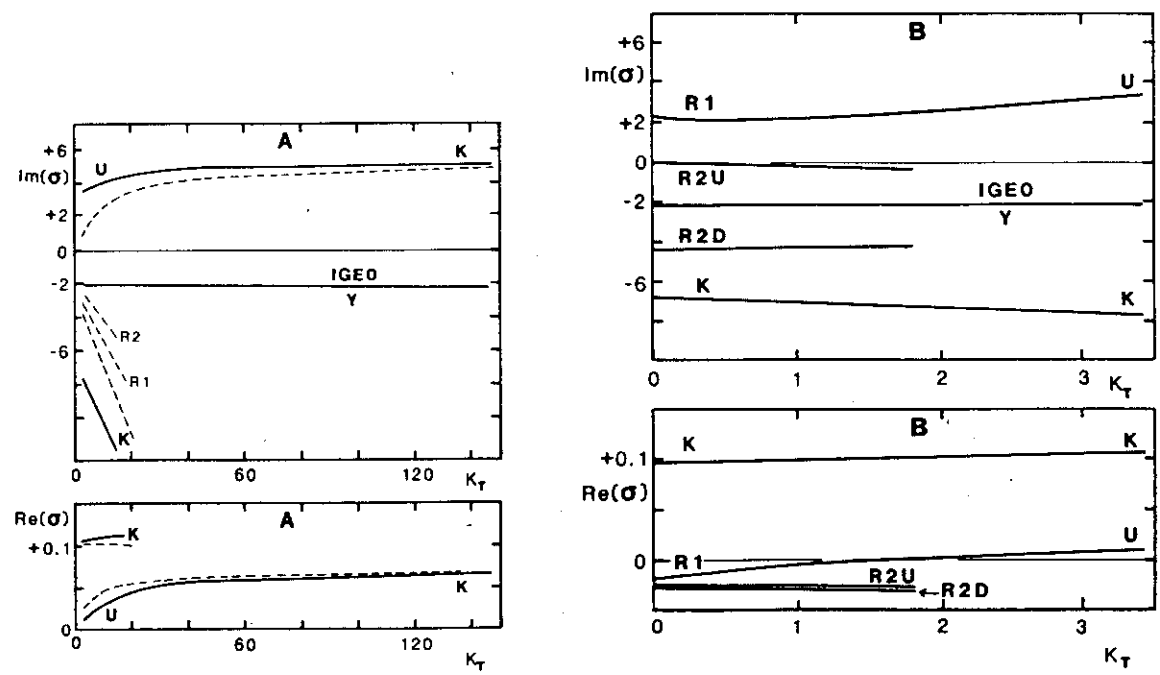

FIG. 11. Growth rates [Im(σ)] and frequencies [Re(σ)] of modes in Model III (solid) and Model IV (dashed) along the (K_T, d) path indicated in Fig. 10. Sections A and B are shown in Figs. 11A and 11B, respectively. Symbols K, R1, R2U and R2D refer to modes as in Figs. 1 and 6; U refers to the unstable mode in Models III and IV. K_T has units 10^{-9} K m^{-1} s^{-1}, units for Im(σ) and Re(σ) are as in Fig. 1.

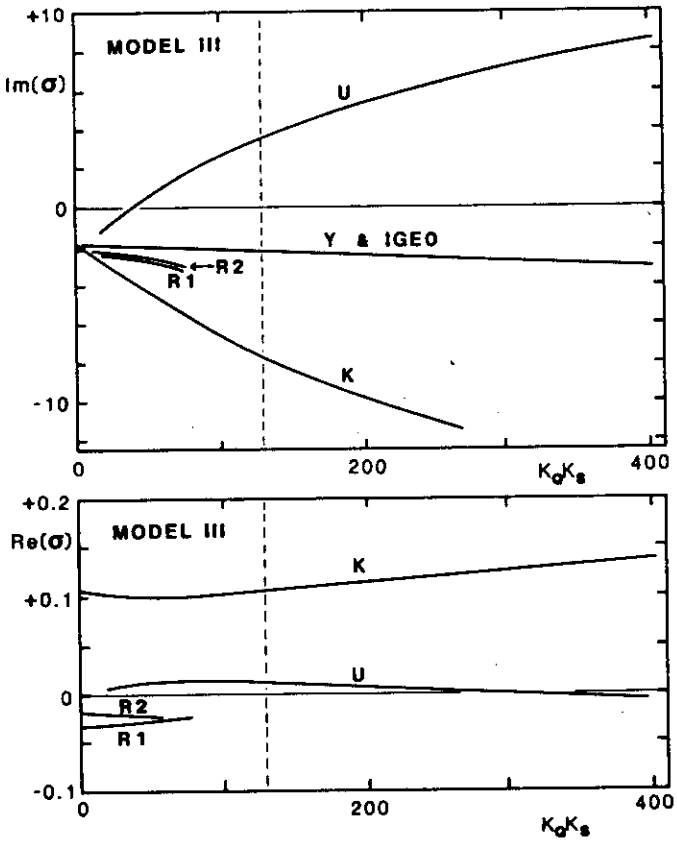

FIG. 12. Growth rates [Im(σ)] and frequencies [Re(σ)] of modes in Model III as a function of K_QK_S. The symbol U refers to the Model III unstable mode. Otherwise as for Fig. 1.

west from their position in Fig. 5a. The equatorial ocean currents in Fig. 14 are largely forced by the wind ($|K_SU|/|h_x + T_x/2| \sim 2$) and are also shifted west from the maximum h perturbation; thus $\langle u\tau^x \rangle$ remains positive. Oceanic convergence is centered near the maximum h perturbation, so wave propagation is slow relative to growth rate. The equatorial structure of the unstable mode resembles that of Lau (1981), except that SST perturbations are located very differently. As K_T is further decreased, the maximum h perturbation moves off the equator to complete the transition to the form in Fig. 9b.

The horizontal structure of the damped Kelvin wave in Model III is not shown since it is almost identical to that of the Kelvin mode in Model II (Fig. 9a).

d. Model IV

Growth rates and frequencies of modes in Model IV, where $\bar{T}_x = 0$, are shown in Fig. 11a along the first leg of the (K_T, d) path (Fig. 10). Both growth rate and frequency of the unstable mode decreases markedly as K_T and d are decreased from the Model I limit to more realistic values (Appendix A). Damped Kelvin and Rossby modes are also present at realistically small K_T and d. We next consider behavior of Model IV free modes at the corner point ($K_T = 3.5 \times 10^{-9}$ K m^{-1} s^{-1}, $d = 1.16 \times 10^{-7}$ s^{-1}).

Growth rates and frequencies as functions of k shown in Fig. 15 somewhat resemble those of Model III (Fig. 13), where $\bar{T}_x = -5 \times 10^{-7}$ K m^{-1}. The unstable mode is again present at long wavelengths, but growth/decay rates of both the unstable and the damped Kelvin modes are much smaller here. Further, the unstable mode now has (slow) eastward propagation at all wavelengths.

Values of σ are found to depend on the product $K_QK_SK_T$ when other parameters are held constant and the small terms $\alpha g(\bar{h}T_x, \bar{h}T_y)/2$ are neglected. The growth rate of the unstable mode decreases as $K_QK_SK_T$ is decreased; the mode (at $k = 0.106$) is neutral when $K_QK_SK_T$ has one half the representative value (Table 1).

The horizontal structure of the unstable mode (Fig. 16) is broadly similar to that of Model III (Fig. 14), however the $|T|_{max}/|h|_{max}$ ratio is now much smaller

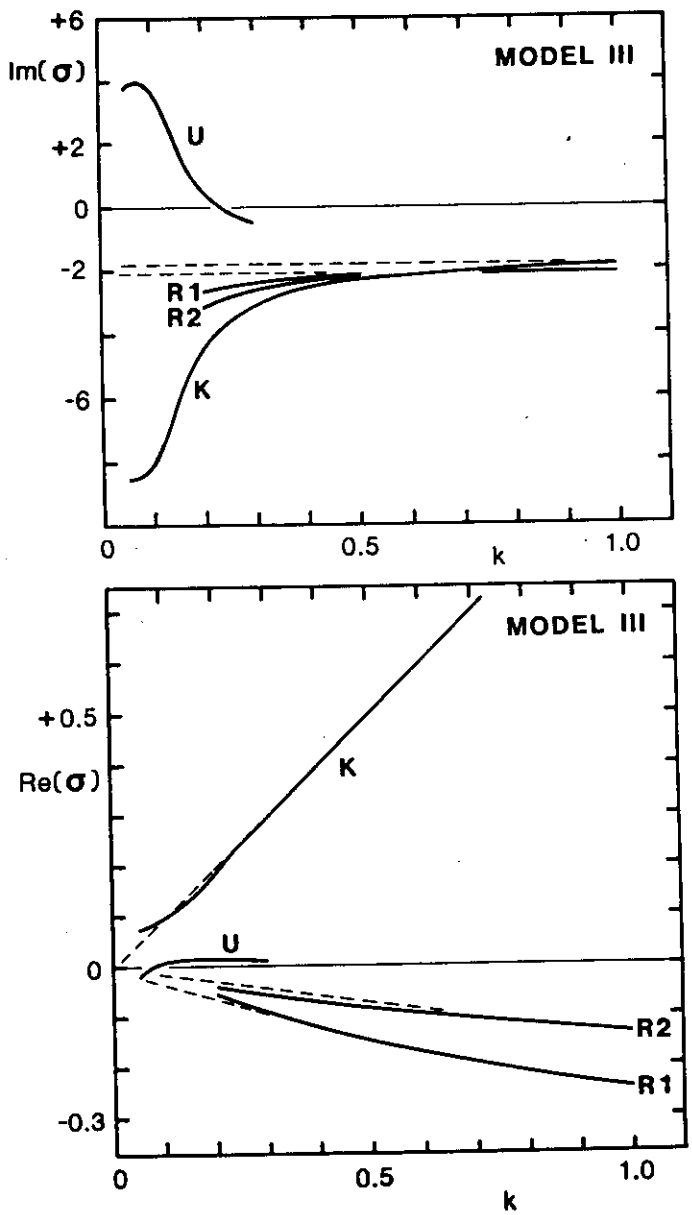

FIG. 13. As in Fig. 12 but as functions of wavenumber k.

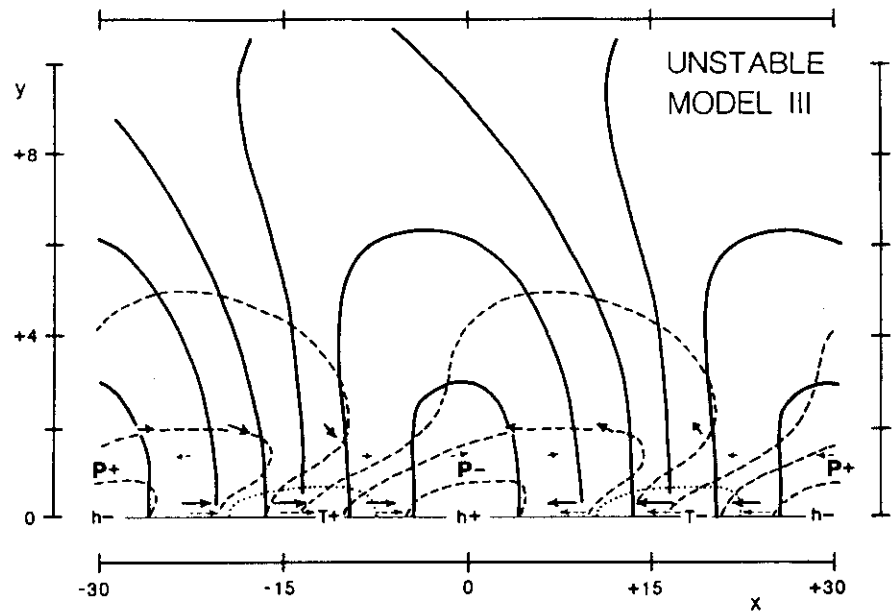

FIG. 14. Eigenfunction for the Model III unstable mode when K_Q and K_S have "representative" values; otherwise as for Fig. 5.

(Table 4). The smaller SST perturbations result from the elimination of zonal advection, which provides the principal thermal forcing in Model III. Smaller SST perturbations lead to weaker atmospheric motion. The reduced growth rate may then be readily explained with the aid of the oceanic energy equation [essentially (8)].

The oceanic structure of the unstable mode at representative K_QK_S (Fig. 16) superficially resembles that of an uncoupled Kelvin wave, but it is not an analytic continuation of the uncoupled oceanic Kelvin wave. When K_QK_S is at ten percent of the representative value, all perturbations associated with the unstable mode extend farther from the equator than in Fig. 16, and the largest T and h perturbations are now located off the equator. When K_QK_S is at one percent of the representative value, the largest T and h perturbations are found at about 40 degrees of latitude. Also, $\mathrm{Re}(\sigma) \to 0$ as $K_QK_S \to 0$ for the unstable mode and, at small K_QK_S, the T perturbations become very large relative to h perturbations in order that the ocean thermal equation (2d) be satisfied. Clearly, neither the structure nor the phase speed of the unstable mode converge toward those of the uncoupled oceanic Kelvin wave as $K_QK_S \to 0$. Thus a mode of somewhat Kelvin-like oceanic structure in a strongly coupled system need not be an analytical continuation of the oceanic Kelvin wave in the corresponding uncoupled system.

Free modes have also been computed for Model IV when K_T is negative. In this case, the Kelvin and $n = 1$ Rossby modes are both destabilized. However there is no slow unstable mode resembling that when $K_T > 0$.

The Model IV equations are of particular interest because they are similar to a linearization of Anderson and McCreary's (1985) cyclic model featuring a zonally unbounded ocean. When advections are neglected, Laplacians in the horizontal diffusion terms are replaced by $-2\lambda_0^{-2}$ (Appendix A), and the entrainment/heat flux terms are linearized, the equations of Anderson-McCreary become identical to those for Model IV, with K_E, b, K_T and d functions of the background state $(\bar{h}, \bar{T})$. Direct linearization is not further pursued here, in part because of ambiguity concerning the appropriate background state and the great sensitivity of the important parameter K_T to it. Nevertheless, we do note some interesting similarities between Anderson and McCreary's disturbance and the results for the unstable mode presented in Figs. 15 and 16. The unstable mode displays a frequency [of $\mathrm{Re}(\sigma) \sim 0.025$] that is almost constant with wavelength for $0.05 < k < 0.2$. Anderson and McCreary's disturbance likewise displays a frequency almost independent of wavelength. The frequency of Anderson and McCreary's disturbance [equivalent to $\mathrm{Re}(\sigma) \sim 0.006$] is smaller than that for the unstable mode in Fig. 15, but that for the unstable mode is found to decrease rapidly as prescribed atmospheric damping (A, B) is increased. When $A = B = 30 \times 10^{-6}$ s^{-1}, $c_a = 60$ m s^{-1} and $K_Q = 33 \times 10^{-3}$ m^2 s^{-3} K^{-1} (as in Anderson and McCreary, 1985), the unstable mode has frequencies [$\mathrm{Re}(\sigma)$] of 0.011 and 0.008 at wavelengths of 15 000 km ($k = 0.106$) and 30 000 km, respectively. The unstable mode in Fig. 16 displays lags of maximum SST ($\pi/4$) and eastward windstress ($\pi/3$) behind maximum h similar to those for Anderson and McCreary's disturbance. Also, the longitude of strongest zonal wind shifts westward with increasing latitude in both cases. The above similarities suggest that the existence and character of Anderson and McCreary's disturbance may in part be explained by linear dynamics.

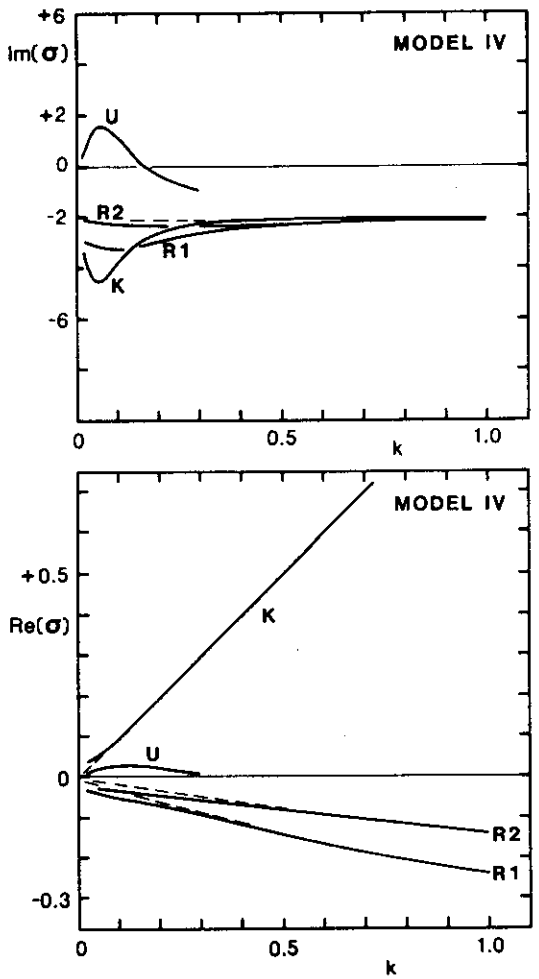

FIG. 15. Growth rates [Im(σ)] and frequencies [Re(σ)] of modes in Model IV as functions of wavenumber k. The symbol U refers to the Model IV unstable mode. Otherwise as for Fig. 2.

5. Sensitivity to heating distributions

a. Zonally shifted latent heating pattern

The sequence of changes in free modes evident as the ocean thermodynamics is varied from the Model I to the Model II limit (Fig. 11) results primarily from the shift in position of the SST anomaly (hence latent heating) relative to oceanic dynamical fields (i.e., u, v, h). Table 5 shows that a similar sequence of changes is observed when the latent heating pattern is shifted (by prescription) progressively farther westward relative to the SST anomaly field, independent of the assumed ocean thermodynamics. The shift in latent heating is effected by multiplying $K_Q T$ in (6) by $e^{i\theta}$, where θ is the prescribed shift in radians. When atmospheric heating approximately overlies the oceanic wave crest, an eastward propagating unstable mode is present which is found (by incremental variation of K_Q) to be a destabilized ocean Kelvin wave. As atmospheric heating is located successively farther to the west, the unstable mode slows, then acquires westward propagation. The mode is a destabilized $n = 1$ Rossby wave when atmospheric heating is centered about one-quarter to one-half a wavelength west from the ocean wave crest. The aforementioned destabilized waves partly retain their uncoupled oceanic structure. In Table 5, "K"/"R1" indicate that the mode has a Kelvin-like/Rossby-like ocean structure; i.e., h is maximum on/off the equator and the strongest eastward/westward current is displaced zonally from maximum positive h by less than 0.2 wavelengths. The above results demonstrate that modal behavior depends on the position of atmospheric heating relative to oceanic dynamical fields, a factor that may be altered by a change in either ocean thermodynamics or the phase relation between atmospheric heating and SST anomalies.

These results are also of interest with regard to the 1982–83 ENSO, during which the pattern of anomalous latent heating (as indicated by OLR) was displaced typically between 10° and 40° of longitude west from that of anomalous SST. This displacement may result from the presence of a climatological westward SST gradient and a nonlinear relationship between SST and latent heating (Appendix B).

b. Meridional restriction of latent heating

Philander et al. (1984) argue that the assumption (6) relating latent heating and underlying SST perturbations is unrealistic since the apparent modulation of latent heating anomalies by climatological atmospheric divergence (e.g., Khalsa, 1983) is ignored. Philander et al. (1984) advocate an alternative assumption that differs from (6) in that (for small perturbations) Q is set equal to zero where climatological lower-tropospheric divergence is positive. Philander et al. do not use their alternative assumption in modeling experiments, however, they invoke it to conjecture that the usual February–March timing of ENSO initiation is linked to the proximity of the eastern Pacific ITCZ to the equator at that time. Climatological wind divergence patterns (Rasmusson and Carpenter, 1982) averaged zonally between 80°W and 130°W indicate a convergence zone (the Intertropical Convergence Zone) lying between 5°S and 11°N in February and between 5°N and 19°N in August, with positive divergence at other latitudes. However, the climatological divergence field in large part mirrors that for SST, and modulation of the SST anomaly–latent heating relationship may be alternatively explained in terms of the nonlinear relationship between total latent heating and SST (Appendix B, Section 2). At SST less than 26°C, latent heating is essentially zero and temperature perturbations no longer imply heating perturbations, i.e., $K_Q \sim 0$. It is only in February–April that the band of water over 26°C in the eastern Pacific extends southward over the equator (Reynolds, 1982). In August, SST is less than 26°C south from about 5°N; there the appropriate value of K_Q is zero. The effect of setting meridional limits for latent heating on ocean–atmosphere instability is reported in this subsection; the seasonal shift in the convergence zone is simulated by setting

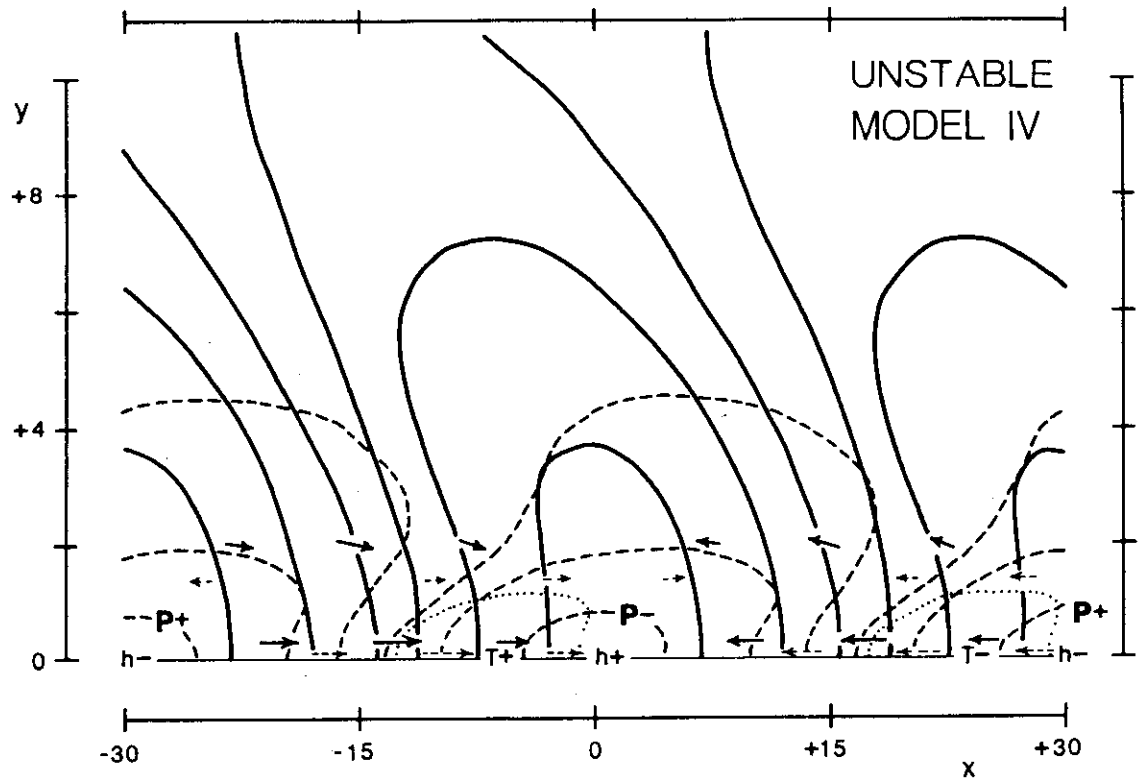

FIG. 16. As in Fig. 14 but of Model IV.

$Q \equiv 0$ outside a "latent heating zone" 16 degrees of latitude wide and centered at successively higher latitudes. Within this zone, $Q = K_Q T$ as per (6) and K_Q is simply set equal to the representative value (Table 1).

The relationship between position of the latent heating zone and growth rate is shown in Fig. 17 for the Model I Kelvin wave. The restriction in latent heating has almost no effect on growth rate when the latent heating zone is centered near the equator (as in February). The growth rate declines rapidly as the zone is shifted northward, especially when the southern boundary crosses the equator. The effects of coupling are small when the latent heating zone lies entirely in the Northern Hemisphere. Results for Models II–IV are analogous; no unstable modes were found in any model when the latent heating zone was in its "August" position (5° to 21°N). Conditions permitting anomalous latent heating close to the equator are apparently essential for the existence of equatorial coupled instabilities.

TABLE 5. Growth rates [Im(σ)] and frequencies [Re(σ)] of the most unstable symmetric mode when atmospheric heating is shifted zonally from the SST perturbation. I, II and III refer to ocean thermodynamics of Models I, II and III, respectively; "shift" indicates the distance (360° = one wavelength) that heating is shifted east (+) or west (−) from the SST perturbation.

Shift (deg)	I		III		II	
	Im(σ)	Re(σ)	Im(σ)	Re(σ)	Im(σ)	Re(σ)
+90	+27	+143 K	+41	+82 K	+27	+75 K
+68	+38	+129 K	+41	+64 K	+23	+53 K
+45	+45	+112 K	+39	+45 K	+20	+27
+22	+50	+93 K	+37	+27 K	+22	+3
0	+53	+72 K	+35	+11	+23	−16 R1
−22	+53	+49 K	+30	−2 R1	+20	−30 R1
−45	+52	+26 K	+23	−13 R1	+14	−43 R1
−68	+51	+3 K	+15	−22 R1	+8	−53 R1
−90	+47	−17	+8	−28 R1	−1	−59 R1
−112	+42	−38 R1	−0	−32 R1	−10	−64 R1

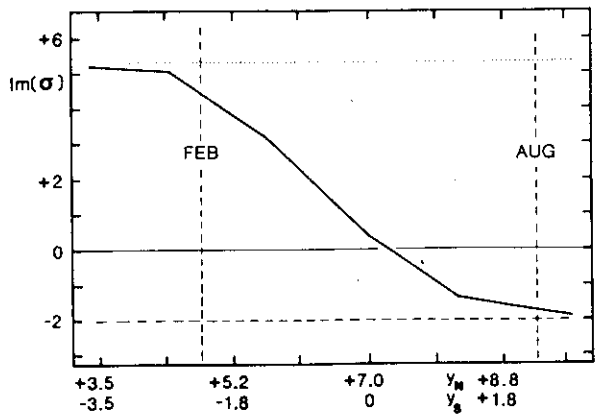

FIG. 17. Dependence of growth rate [Im(σ)] for Model I Kelvin wave on position of a zone to which latent heating is restricted. y_N and y_S indicate positions of the northern and southern zone boundaries, in nondimensional units. "FEB" and "AUG" indicate extreme annual positions of observed convergence zone. Im(σ) is in 10^{-2} nondimensional units. Values of Im(σ) when latent heating is suppressed or permitted everywhere are indicated by thin dashed and dotted lines, respectively.

Horizontal structures of unstable modes when the latent heating zone is at its "February" position (5°S to 11°N) are essentially unchanged from those in Figs. 5, 9, 14 and 16. When the zone lies between 0.3°S and 15°N, maximum wind and ϕ perturbations are shifted slightly to the north of the equator and a cross equatorial wind, southerly in regions of heating, is present.

The importance of equatorial latent heating in the destabilization of waves is further demonstrated in Fig. 18, which shows the dependence of growth rate for the Model I Kelvin wave on the width of a zone (centered on the equator) in which $Q \equiv 0$. Elsewhere, $Q = K_Q T$. Coupling is ineffective when latent heating is kept more than 500 km ($y = 2$) from the equator; the wave decays at near the uncoupled rate. Unstable modes in Models II–IV are similarly affected. Conversely, growth rates are hardly decreased when latent heating is restricted to a zone only 1000 km wide centered on the equator ($-2 < y < +2$). The dependence of instability on equatorial latent heating is consistent with the structure of unstable modes in Figs. 5, 9, 14 and 16, where the major contribution to $\langle \phi Q \rangle$ is made within a few degrees of the equator.

These results demonstrate that a suppression of latent heating within a few degrees of the equator inhibits ocean-climate instability, and thus supports hypotheses concerning seasonal timing of ENSO onset.

6. Further sensitivity characteristics

a. Equilibrium atmosphere

Anderson and McCreary (1985), Gill (1985) and Yamagata (1985) all prescribe their atmospheres to be in equilibrium with the underlying SST perturbation pattern, by neglecting the terms U_t, V_t and ϕ_t in (1). An investigation is conducted here into the behavior of symmetric modes in a Model I featuring such an atmosphere. First we neglect the terms involving σ in (9a–c) and then use a finite difference form of the remaining diagnostic relations to find (by matrix inversion) U and V as functions of h. Then U and V are eliminated from (9d–f), and we proceed using the finite difference method (section 3a) on (9d–f) to obtain eigenvalues and eigenvectors. Resulting growth/decay rates and frequencies for the Kelvin wave and for the $n = 1$ Rossby wave over the range $0.02 < k < 1$ were all within 0.7×10^{-2} nondimensional units of respective values obtained using the full Eqs. (9a–c) (Fig. 2). This close agreement is consistent with results in Table 4; the atmosphere is nearly in equilibrium primarily because the prescribed atmospheric damping time scale ($A^{-1} \sim 2.3$ days) is very much less than the heating time scale ($|\sigma|^{-1} \sim 23$ days for the Kelvin wave when $k = 0.106$).

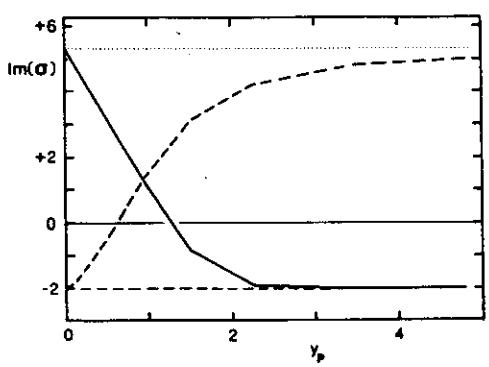

FIG. 18. Growth rate [Im(σ)] of the Model I Kelvin wave as a function of the meridional width of an equatorially centered zone from which latent heating is excluded (solid line) or to which latent heating is restricted (dashed line). The half-width of the zone, y_P, is in nondimensional units. Otherwise as for Fig. 17.

b. Advecting background wind

Here we explore the effect of advection by a background zonal wind ($\bar{U}$) that is horizontally and vertically uniform. First, the terms $\bar{U}U_x$, $\bar{U}V_x$ and $\bar{U}\phi_x$ are added to (1a), (1b) and (1c), respectively. Free modes are then computed for Models I–IV with $\bar{U} = \pm 4$ m s^{-1}; other coefficients and wavenumber are as in Table 1. The above values of $\bar{U}$ are typical of the climatological zonal wind averaged vertically through the troposphere over the equatorial Pacific, as estimated via Arkin et al. (1983). Introduction of atmospheric advection changes growth/decay rates only slightly (typically by less than twenty percent), however phase speeds are more significantly affected. Phase speeds [Re(σ)/k] for each of the Model I Kelvin, Model II $n = 1$ Rossby and the Models III and IV unstable modes are increased by between +0.1 and +0.2 m s^{-1} when $\bar{U}$ is increased from zero to +4 m s^{-1}. Thus the above modes propagate more quickly eastward (or more slowly westward) in the presence of a background westerly wind; a background easterly wind has the opposite effect on modal propagation. Hence the Model II $n = 1$ Rossby wave is nearly stationary when $\bar{U} = +4$ m s^{-1} and the unstable mode of Model III is nearly stationary when $\bar{U} = -4$ m s^{-1}, for wavenumber $k = 0.106$. These results further illustrate the sensitivity of modal behavior to atmospheric background state.

c. Estimate of nonlinear temperature advection effects

Eigenfunctions obtained for the linear models can be used to estimate the potential importance of some nonlinear processes that have been neglected; here we discuss advection of the SST perturbation (T) by the perturbation currents (u, v). Maximal sizes attained by terms in the linear ocean thermal equation (2d) in association with selected modes are compared in Table 6 to maximal sizes that the T advection terms (uT_x, vT_y) would have given the same fields. When the maximum T is 0.5 K, zonal T advection is a factor of 2–4 smaller than the dominant linear forcing, thus the zonal T advection term would become dominant when the maximum T associated with the growing disturbance surpasses 1–2 K. The meridional T advection term would be smaller, but not generally insignificant. The

TABLE 6. Comparison between maximum magnitudes attained by terms in (2d) and maximum magnitudes that uT_x and vT_y would attain given the same fields. Terms are scaled so that the dominant term has a maximum magnitude of 100 units. Magnitudes for nonlinear terms assume a maximum T of 0.5 K.

Term	Model: / Mode:	II R1	II K	III U	IV U
T_t		60	100	67	69
$\bar{T}_x u$		100	91	100	—
$K_T h$		—	—	25	100
dT		45	17	39	50
uT_x		28	34	22	48
vT_y		20	2	11	8

value of the T advection terms would display a zonal wavelength half that of the linear wave.

d. *Change in prescribed oceanic damping*

It is easy to show from the model equations that a change in the oceanic damping coefficients (a, b and d) simply results in an equivalent shift in growth/decay rates while frequencies are left unaltered, provided that the coefficients A and B are changed by a like amount.

7. Discussion

The present work demonstrates that disturbances observed in several coupled ocean–atmosphere models can be explained in terms of unstable free modes, and clearly reveals the considerable impact of ocean thermodynamics and distribution of atmospheric heating on modal behavior. Real world applications are discussed in this section, but first we briefly review limitations on such applications arising from the simplicity of the models. First, eigenmode analyses as performed here require that all coefficients be constant zonally. In reality, the background state in the western equatorial Pacific is very different to that farther east, and appropriate values for model coefficients would likewise change zonally (e.g., appendix A). The zonal variation occurs over a distance of the same order as the wavelengths of the most unstable long waves. Second, growing disturbances in an ocean basin would presently be affected by the zonal boundaries. Third, real growing disturbances would soon be influenced by nonlinear processes, in particular nonlinearities in the mechanisms of SST anomaly generation (section 6c and Appendix A) and in the relationship between atmospheric heating and SST (appendix B, section 2). One effect of nonlinear ocean thermal processes may be to ultimately limit the intensification of the disturbances, as in the model of Anderson and McCreary (1985). Nonlinearities in atmospheric heating reduce the effect of cold SST anomalies on atmospheric heating, and hence may limit development of cold water events. Fourth, even in the context of linear theory, more than one vertical mode is probably significant in the ocean's thermal and kinetic response to anomalous wind forcing (e.g., Busalacchi and Cane, 1985). Motions in all oceanic vertical modes included in a linear coupled model are linked via the atmosphere; it would be interesting to determine the effect of a second oceanic vertical mode on the instabilities reported herein. Finally, the dependence of SST on windspeed (via modulation of entrainment and surface heat loss rates) has been neglected in the present study, but could be represented by a crude linear parameterization if the presence of a background mean wind is assumed.

Despite these limitations, it is instructive to relate the free mode results to real world situations; the results indicate background conditions that may favor instability and suggest early behavior of resulting disturbances. The presence and behavior of unstable model in Models I–IV depend on coefficient values, which in turn depend on the prescribed background state. Real world occurrence of such instabilities would require the presence of a suitable background (i.e., large-scale initial) state. Aspects of a background state that favor instability include high SST (large K_Q), shallow thermocline/mixed layer (large K_S and K_T), large east–west SST gradient ($|\bar{T}_x|$ large), weak net surface heat flux (K_T large) and strong background surface winds (large K_S and K_T).

We now discuss the potential for instability in the equatorial Pacific as indicated by free mode analysis, by first taking background states based on climatology and then taking as a background state the state observed immediately prior to an actual ENSO episode. Analysis for the oceanwide equatorial duct is unfortunately not possible because of large zonal changes in background state; we divide the equatorial ocean into the "central west Pacific" (5°N–5°S, 160°E–140°W) and the "eastern Pacific" (5°N–5°S, 130°W–80°W). The value of K_Q is assumed to depend solely on background SST, and values for other coefficients are estimated as per section 2 and appendix A.

Background states based on climatology of the central west equatorial Pacific are considered first. Climatological values for January–February are listed in Table 7. Values for zonal SST gradient ($\bar{T}_x$) and longitudinally averaged SST ($\overline{\text{SST}}$) are from Reynolds (1982), for net surface heat flux ($\bar{I}_0 - \bar{F}_0$) is from Ramage et al. (1980; January–February 1972 and 1973 average), surface zonal wind ($|\bar{U}_l|$) and friction velocity ($\bar{u}_*$) are from Wyrtki and Meyers (1975). Also, we assume $h \sim 120$ m (e.g. Gill, 1982). The above values are taken to define a background state, and free modes were computed for the Model III equations with appropriate coefficient values (Table 7). No unstable modes were found at wavelengths less than 20 000 km. The $n = 1$ Rossby mode of (for example) wavelength 12 000 km becomes unstable at a value of $K_Q K_S$ about twice that considered appropriate here. Similar results were obtained when coefficient values are chosen based on central western Pacific climatology for other times of the year. The value of K_T is always small, primarily

TABLE 7. Values of model coefficients estimated (as per section 2) for background states based on January–February climatology and January–February 1972 conditions for the central western equatorial Pacific.

Background states			Model coefficients		
Variable	Climatology	1972	Coefficient	Climatology	1972
$\overline{SST}$ (°C)	27.5	28.0	K_Q (10^{-3} m^2 s^{-3} K^{-1})	4.0	7.0
$\lvert\bar{U}_l\rvert$ (m s^{-1})	4.0	5.2	K_S (10^{-8} s^{-1})	5.2	6.7
$\bar{u}_*$ (10^{-3} m s^{-1})	6.5	8.0	K_T (10^{-9} K m^{-1} s^{-1})	0.63	0.92
$\bar{I} - \bar{F}_0$ (W m^{-2})	+5	+7	a (=b) (10^{-7} s^{-1})	0.5	0.5
$\bar{h}$ (m)	120	120	d (10^{-7} s^{-1})	0.8	0.8
$\bar{T}_x$ (10^{-7} K m^{-1})	−3.8	−4.8	c_0 (m s^{-1})	1.83	1.83

because of the deep thermal mixed layer (we assume $\bar{h} \sim 120$ m throughout), and the ocean thermodynamics are near the thermal advection limit (i.e. Model II). Conditions most conducive to instability occur in May (highest overall $\overline{SST}$) and in September (largest $\bar{T}_x$), and in both cases $n = 1$ Rossby waves of wavelength greater than about 13 000 km are unstable. However, it seems unlikely that instabilities of wavelength more than double the zonal extent of the region under study (6600 km) would develop therein. We have also ignored possible inhibition resulting from the climatological band of equatorial divergence east from 180° (at its strongest in September–October and weakest in January–April; Wyrtki and Meyers, 1975). In any case, a growing Rossby wave would propagate west and soon reach the western boundary without creating a basin-wide disturbance. Eastward propagating unstable modes (which would have greater relevance to ENSO onset) are not found at any time of year.

Conditions in the eastern equatorial Pacific appear to be unfavorable for instability during most of the year (section 5b), in part because SST < 26°C (i.e. $K_Q \sim 0$). Climatological SST is at its highest during February–April ($\overline{SST} \sim 26.5$°C), but then $\bar{T}_x \sim 0$ (Reynolds, 1982); K_T is large (Appendix A), and the ocean thermodynamics are as in Model IV. According to Model IV results (section 4d), any permitted unstable mode will travel eastward and not affect the Pacific basin at large.

Thus climatological background states do not permit instabilities that seem relevant to ENSO, according to our model results. Such a finding is not surprising, the fact that ENSO episodes occur relatively infrequently (about once per four years on average) suggests by itself that climatological patterns are at most marginal for ENSO related instability. Background conditions conducive to such instability may occur only once every few years (as suggested by Rennick and Haney, 1985).

It is of interest, then, to consider as a background state the large-scale state immediately prior to an actual ENSO episode. We define the "background" state immediately prior to the 1972–73 ENSO episode in terms of January–February 1972 average values (Table 7) for relevant variables in the central western equatorial Pacific, from data of Ramage et al. (1980). Again we assume $\bar{h} \sim 120$ m. The above background state is more conducive to instability than the climatological state, since the $\overline{SST}$ is higher, east–west temperature gradient is steeper and surface winds are stronger. A result of the larger $\bar{u}_*$ is that K_T is much larger than that for climatology, and the ocean thermodynamics are moved away from the thermal advection limit. Free modes computed using appropriate coefficients (Table 7) include both a destabilized $n = 1$ Rossby wave and a mode similar in behavior to the Model III unstable mode. Both modes are unstable at wavelengths greater than about 11 000 km; the latter has very slow eastward propagation (phase speed $\leqslant 0.12$ m s^{-1}) at wavelengths less than 20 000 km. The latter mode is not an analytic continuation of any uncoupled ocean wave, and has structure resembling that in Fig. 14, except that ocean perturbation patterns are rather complicated at latitudes of less than two degrees ($y < 0.8$). In the eastern Pacific during January–February 1972, $\bar{T}_x \sim 0$ again, and any permitted instability should propagate eastward according to Model IV results. According to our results, the eastern equatorial Pacific cannot be the sole region for ENSO initiation. Of the various modes considered in the present work, it appears that the Model III unstable mode is the most likely to be relevant to ENSO onset, in part because it propagates slowly (east or west) or develops in situ, depending on wavelength and the exact value of ocean thermal coefficients. We note that in terms of actual SST (Philander and Rasmusson, 1984) and wind anomaly patterns, the 1972–73 and the composite Rasmusson and Carpenter (1982) ENSO episodes appear as in situ developments spanning the Pacific basin, without indication of westward propagation.

Results for Model III are of particular interest with respect to the ocean thermodynamics of observed ENSO episodes. Harrison and Schopf (1984) show that the initial development of SST anomalies during both the Rasmusson and Carpenter (1982) composite ENSO and the atypical eastward propagating ENSO in 1982–83 could result from temperature advection by anomalous currents associated with observed anomalous wind. The SST perturbations associated with the unstable mode in Model III likewise result primarily from temperature advection by anomalous currents (Table 6), no matter whether the mode is developing in situ or propagating slowly eastward.

Some features of the unstable modes illustrated here (Figs. 5, 9, 14 and 16) are qualitatively similar to the anomaly patterns observed during ENSO episodes (Rasmusson and Carpenter, 1982; Arkin et al., 1983). In particular, the largest perturbations of SST and zonal wind lie on the equator, and the maximum positive perturbation for eastward wind lies west of that for SST. However, perturbations are confined more closely to the equator than are anomalies observed during ENSO events. For example, the magnitude of an observed SST anomaly has typically declined to 50% of its equatorial value at between 5° and 10° latitude, while that associated with the Model IV unstable mode (Fig. 16) has declined a like amount at 4.6° latitude. The SST perturbations associated with the other unstable modes illustrated herein are still more narrow. Also, strong meridional winds often observed on either side of the equatorial SST anomaly are not apparent in the unstable mode solutions.

8. Conclusion

Unstable modes are excited by idealized ocean–atmosphere coupling in models that allow a dynamic response in both the atmosphere and ocean. In some cases, unstable modes can be related to particular ocean waves which have been destabilized by coupling. The effect of coupling on the stability of ocean waves depends on the position of induced atmospheric heating in relation to the oceanic velocities. The Kelvin wave is destabilized and Rossby waves are damped when atmospheric heating is centered near the oceanic wave crest (as in Model I). In contrast, the $n = 1$ Rossby wave is destabilized and the Kelvin wave is damped when atmospheric heating is centered a quarter- to a half-wavelength west from the oceanic wave crest (as in Model II). At intermediate positions of atmospheric heating (as in Model III), waves present in the uncoupled ocean are damped on application of coupling; however coupling excites a slowly propagating unstable mode that has structure intermediate between the destabilized waves referred to previously. The position of atmospheric heating relative to ocean dynamical fields may be altered by a change in ocean thermodynamics (as in the sequence of Models I–III–II) or by a change in the (specified) phase relation between atmospheric heating and SST perturbations.

The effectiveness of coupling depends on a variety of model coefficients; larger values of ocean thermal forcing and coupling coefficients and smaller values of damping coefficients and the atmospheric Rossby deformation radius are associated with increased growth rates for unstable modes. Coupling most affects long zonal wavelength and low-frequency modes, for reasons given in sections 4a and 4b. The behavior of low-frequency modes is not significantly altered when the atmosphere is set to be in equilibrium with the SST field, verifying the validity of this commonly used assumption. Coupling is ineffective when atmospheric heating is suppressed within 5° of the equator; this finding supports ideas concerning seasonal timing of ENSO initiation.

The results demonstrate that the behavior of modes in coupled ocean–atmosphere models is crucially dependent on the parameterization of (i) SST and (ii) large-scale latent heating. In particular, the results for Model I explain the occurrence of amplifying eastward-propagating perturbations in the ocean basin coupled model of Philander et al. (1984), while those for Model II explain the dominance of westward propagating perturbations in the ocean basin coupled models of Rennick (1983) and Gill (1985). The slowly propagating unstable mode in Model IV displays several features in common with the disturbance observed in Anderson and McCreary's (1985) nonlinear coupled model. Instability can occur in coupled ocean–atmosphere models under a wide range of model parameterization, but behavioral and structural particulars are very sensitive to changes in that parameterization. Proper parameterization of large-scale latent heating and SST anomalies would seem essential for successful modeling of ENSO events.

Acknowledgments. Hearty thanks to Prof. John A. Young for much useful advice, to Eva Singer for typing the manuscript and to Tony Wendrichs for drafting. Comments on an earlier draft by Drs. T. Yamagata, E. Sarachik and an anonymous reviewer are also appreciated. This study was supported by NSF Grant ATM-144-S482.

APPENDIX A

Development of Perturbation Ocean Model

The simple perturbation ocean models considered in this work are obtained from the following, more complete equations for mixed layer motion;

$$\hat{u}_t + \hat{u}\hat{u}_x + \hat{v}\hat{u}_y - \beta y\hat{v} + \alpha g\Delta\hat{T}\hat{h}_x + \frac{1}{2}\alpha g\hat{h}\hat{T}_x = \frac{\hat{\tau}^x}{\rho_0\hat{h}} - \frac{\hat{w}_e\hat{u}}{\hat{h}} + \nu\nabla_H^2\hat{u} \quad (12a)$$

$$\hat{v}_t + \hat{u}\hat{v}_x + \hat{v}\hat{v}_y + \beta y\hat{u} + \alpha g\Delta\hat{T}\hat{h}_y + \frac{1}{2}\alpha g\hat{h}\hat{T}_y = \frac{\hat{\tau}^y}{\rho_0\hat{h}} - \frac{\hat{w}_e\hat{v}}{\hat{h}} + \nu\nabla_H^2\hat{v} \quad (12b)$$

$$\hat{h}_t + \hat{u}\hat{h}_x + \hat{v}\hat{h}_y + \hat{h}(\hat{u}_x + \hat{v}_y) = \hat{w}_e + \nu\nabla_H^2\hat{h} \quad (12c)$$

$$\hat{T}_t + \hat{u}\hat{T}_x + \hat{v}\hat{T}_y = \frac{f_2(\hat{h})\hat{I}_0 - \hat{F}_0}{\rho_0 c_w\hat{h}} - \frac{\hat{w}_e\Delta\hat{T}}{\hat{h}} + \nu\nabla_H^2\hat{T} \quad (12d)$$

$$\hat{w}_e = \frac{2m\hat{u}_*^3}{\alpha g\hat{h}\Delta\hat{T}} + \frac{n}{\rho_0 c_w\Delta\hat{T}}(\hat{F}_0 - f_1(\hat{h})\cdot\hat{I}_0). \quad (13)$$

The hat (^) denotes a total variable, which is the sum at a background value (to be denoted by an overbar) and a fluctuating perturbation (left unmarked), e.g., $\hat{h} = \bar{h} + h$. The left-hand side of (12) follows directly from Anderson and McCreary (1985). On the right-hand side of (12), windstress $(\hat{\tau}^x, \hat{\tau}^y)$ acts as a body force in the mixed layer. Entrainment is permitted through the base of the mixed layer; the entrainment velocity, $\hat{w}_e$, is assumed to obey (13), the Kraus-Turner formula calibrated by Garwood (1977). Entrainment damps horizontal motion and cools and deepens the mixed layer (e.g. Niiler and Kraus, 1977). The value of $\hat{T}$ is also affected by the net energy flux $(\hat{F}_0 - \hat{I}_0)$ through the ocean surface, where $\hat{F}_0$ is the sum of sensible, latent and longwave radiant heat loss and $\hat{I}_0$ is the net downward insolation flux at the ocean surface. All variables are subject to small horizontal eddy diffusion. Values and definitions for the constants ρ_0, α, g, ν, c_w, m and n are given in Table 2. In (13), $\hat{u}_*$ is the friction velocity

$$\hat{u}_* = (\rho_a C_D/\rho_0)^{1/2}|\hat{\mathbf{V}}_l|,$$

$\hat{f}_1(\hat{h})$ is a function required to account for the effects of penetrating radiation on $\hat{w}_e$, and $f_2(\hat{h})$ represents the proportion of $\hat{I}_0$ absorbed within the mixed layer.

Equations (2) are derived by linearizing (12) about the background state and adopting the further simplifications indicated in Section 2b1. We also assume long waves, and thence we approximate $\nabla_H{}^2 u \sim \partial^2 u/\partial y^2 \sim -2\lambda_0{}^{-2}u$, for example. Finally, we replace $\hat{\tau}^x/(\rho_0\hat{h})$ and $\hat{\tau}^y/(\rho_0\hat{h})$ by $\tau^x/(\rho_0\bar{h})$ and $\tau^y/(\rho_0\bar{h})$.

Formulae for estimating values of the coefficients K_E, K_T, a, b and d in (2), determined via linearization of the heat flux and entrainment terms in (12) with w_e as in (13), are

$$a = \frac{\bar{w}_e}{\bar{h}} + \frac{2\nu}{\lambda_0{}^2}$$

$$b = \frac{2\nu}{\lambda_0{}^2} + \frac{2m\bar{u}_*^3}{\alpha g\bar{h}^2\Delta\bar{T}} + \frac{n\bar{I}_0 f_1'(\bar{h})}{\rho_0 c_w \Delta\bar{T}}$$

$$d = \frac{2\nu}{\lambda_0{}^2} + \frac{1}{\rho_0 c_w \bar{h}}\left\{(1+n)\frac{\partial F_0}{\partial T} - [f_2(\bar{h}) + nf_1(\bar{h})]\frac{\partial I_0}{\partial T}\right\}$$

$$K_E = \frac{-2m\bar{u}_*^3}{\alpha g\bar{h}\Delta\bar{T}^2} - \frac{n}{\rho_0 c_w \Delta\bar{T}^2}[\bar{F}_0 - f_1(\bar{h})\bar{I}_0] + \frac{n}{\rho_0 c_w \Delta\bar{T}}\left[\frac{\partial F_0}{\partial T} - f_1(\bar{h})\frac{\partial I_0}{\partial T}\right]$$

$$K_T = \frac{4m\bar{u}_*^3}{\alpha g\bar{h}^3} + \frac{(1+n)\bar{F}_0}{\rho_0 c_w \bar{h}^2} - \frac{[f_2(\bar{h}) + nf_1(\bar{h})]\bar{I}_0}{\rho_0 c_w \bar{h}^2} + \frac{[f_2'(\bar{h}) + nf_1'(\bar{h})]\bar{I}_0}{\rho_0 c_w \bar{h}}.$$

TABLE 8. Values of regression coefficients determined using climatic data across the Atlantic Ocean for the indicated latitude and month.

Coefficient	January equator	July equator	October 10°N	Average
$\frac{\partial F_0}{\partial SST}$ (W m^{-2} K^{-1})	+11.5	+14.6	+27.5	+17.9
$\frac{\partial I_0}{\partial SST}$ (W m^{-2} K^{-1})	+5.5	+6.4	−3.6	+2.7

According to Garwood (1977)

$$f_1(h) = 1 + \frac{I(-h)}{I_0} - \frac{2}{h}\int_{-h}^{0}\frac{I(z)}{I_0}\,dz.$$

Also, $f_2(h) = 1 - I(-h)/I_0$. We define $I(z)$ as the net downward insolation flux at depth $|z|$ and $I_0 = I(0)$. For evaluations of $f_1(\bar{h})$ and $f_2(\bar{h})$, we use the formula of Paulson and Simpson (1977)

$$I(z) = I_0[Re^{\gamma_1 z} + (1-R)e^{\gamma_2 z}]$$

where $R = 0.58$, $\gamma_1 = (0.35\text{ m})^{-1}$, $\gamma_2 = (23\text{ m})^{-1}$.

The values of $\partial F_0/\partial T$ and $\partial I_0/\partial T$ depend on complicated atmospheric processes (Albrecht, 1981) beyond the scope of this study. Real values are crudely estimated here via a regression analysis using monthly climatic data for the equatorial Atlantic; details are given in Appendix B. The estimated values of $\partial F_0/\partial T$ and $\partial I_0/\partial T$ are given in Table 8.

Values of a, b, d, K_E and K_T have been computed for several background states and are given in Table 9. Values adopted for $\bar{I}_0$ and $\bar{F}_0$ are based on annual means for the Atlantic ("western" and "central") or February–March values at 90°W and 100°W ("far eastern") (Hastenrath and Lamb, 1978); $\Delta\bar{T}$ is set at 14 K in each case; values of K_T, a and d are unaffected by different choice of $\Delta\bar{T}$.

APPENDIX B

Regression Studies

1. SST and thermocline depth

The proportionality constant κ relating h to T in Model I is determined by a regression of SST on thermocline depth. Data are time series of two-monthly mean SST and depth of selected isotherms for the eastern (80–95°W) equatorial Pacific from 1971 through 1973, presented by Gill (1982). This period includes the 1972–73 ENSO. The "thermocline depth" at each time point is taken to be an average of the 16° and 20°C isotherm depths. The mean thermocline depth was 68.5 m. The rather noisy raw data was smoothed using a two-point running mean prior to regression analysis. The resulting $\kappa = +0.03$ K m^{-1} and the correlation coefficient is +0.60. Similar estimates of κ are obtained using values of d and K_T from the "central Pacific" or "Far East Pacific" columns of Table 9.

2. Determination of K_Q: Outward longwave radiation (OLR) on SST

An indication of the actual relationship between local latent heating and underlying SST is given by a plot of outward longwave radiation (OLR) versus underlying SST shown in Fig. 19 for the equatorial Pacific between 150°E and 120°W. It is well known that OLR is strongly related to precipitation amounts over tropical oceans (e.g., Lau and Chan, 1983). The relation between OLR and SST is rather nonlinear; a crude value for the coefficient K_Q is obtained via a regression of OLR on SST using only those data in Fig. 19 for which $26° < \text{SST} < 30°\text{C}$. The gradient of the least squares line is -19.8 (W m^{-2}) K^{-1} and the correlation coefficient is -0.81. No published empirical formula relating monthly mean OLR to monthly rainfall appears to be available; we take the proportionality constant to be -5.58 (mm month^{-1}) (W m^{-2})$^{-1}$ after Shukla (personal communication, 1984). Thus rainfall is estimated to increase with SST at the rate of 110 (mm month^{-1}) K^{-1}. A value of $K_Q = 7.0 \times 10^{-3}$ m^2 s^{-3} K^{-1} is then determined using the thermodynamic equation and hydrostatic approximation for the atmosphere.

The most appropriate value of K_Q depends strongly on assumed background SST ($\overline{\text{SST}}$), because of the nonlinear relationship between SST and OLR (Fig. 19). Our adopted value of K_Q may be reasonable for a background state where $\overline{\text{SST}} \sim 28°\text{C}$. Analyses similar to that above but using only those data where $25°\text{C} \leq \text{SST} \leq 28°\text{C}$ or where $28°\text{C} \leq \text{SST} < 30°\text{C}$ (appropriate for $\overline{\text{SST}} \sim 26.5°\text{C}$ and for $\overline{\text{SST}} \sim 29°\text{C}$) yield K_Q values of 1.9×10^{-3} m^2 s^{-3} K^{-1} and 11.1×10^{-3} m^2 s^{-3} K^{-1}, respectively.

3. Surface fluxes versus windspeed and SST

Values of $\partial F_0/\partial T$ and $\partial I_0/\partial T$ are empirically determined using monthly climatic data for the equatorial Atlantic made available by Hastenrath and Lamb (1977). No corresponding data for the equatorial Pacific appears to be available. Values of SST, surface wind speed ($|\mathbf{V}_s|$), F_0 and I_0 were read at 5° longitude intervals across the Atlantic at the equator in July and October and at 10°N in January. In each case, sizable zonal SST differences were present at the designated latitude. Multiple regression analyses for F_0 on SST and $|\mathbf{V}_s|$ and for I_0 on SST and $|\mathbf{V}_s|$ were performed for each month. Three values for each of $\partial F_0/\partial|\mathbf{V}_s|$, $\partial I_0/\partial|V_s|$, $\partial F_0/\partial\text{SST}$ and $\partial I_0/\partial\text{SST}$ were computed thus. Averaged values of $\partial F_0/\partial\text{SST}$ and $\partial I_0/\partial\text{SST}$ are used for $\partial F_0/\partial T$ and $\partial I_0/\partial T$, respectively. Relevant individual and average values are shown in Table 7. The average

$$\partial F_0/\partial|\mathbf{V}_s| = +9.4 \text{ W m}^{-2} (\text{m s}^{-1})^{-1},$$

and

$$\partial I_0/\partial|\mathbf{V}_s| = +2.4 \text{ W m}^{-2} (\text{m s}^{-1})^{-1}.$$

TABLE 9. Values of coefficients in Eqs. 2 estimated for several different background states using formulae in appendix A.

	"West Pacific"	"Central Pacific"	"Far East Pacific"
$\bar{h}$ (m)	130	70	30
$\bar{u}_*$ (10^{-3} m s^{-1})	5	8	5
$\bar{F}_0$ (W m^{-2})	175	160	120
$\bar{I}_0$ (W m^{-2})	190	195	195
$f_1(\bar{h})$	0.85	0.75	0.64
$f'_1(\bar{h})$ (10^{-3} m^{-1})	1.1	2.3	3.8
$f_2(\bar{h})$	1.00	0.98	0.89
$f'_2(\bar{h})$ (10^{-3} m^{-1})	0.06	0.9	4.9
λ_0 (10^5 m)	3.0	2.5	2.1
a (10^{-7} s^{-1})	0.5	0.7	1.0
b (10^{-7} s^{-1})	0.5	0.7	1.0
d (10^{-7} s^{-1})	0.7	1.3	2.6
K_E (10^{-8} m K^{-1} s^{-1})	6.3	2.8	4.5
K_T (10^{-9} K m^{-1} s^{-1})	0.05	3.5	6.6

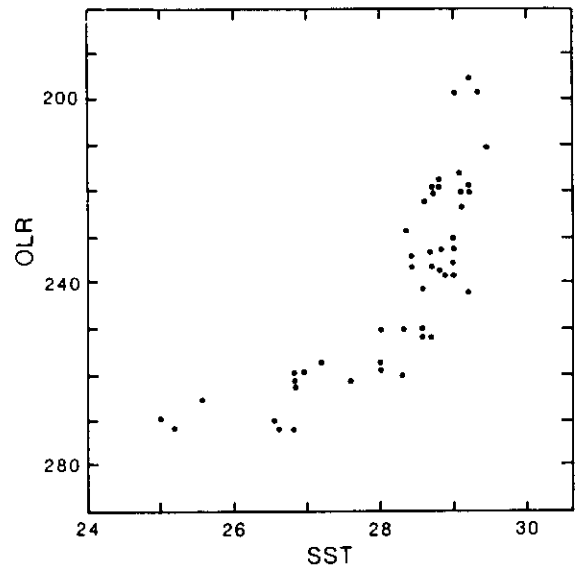

FIG. 19. Plot of outward longwave radiation (OLR; W m^{-2}) versus underlying SST (°C) in the equatorial Pacific. OLR and SST values represent averages between 5°N and 5°S and over monthly periods, given by Arkin et al. (1983). Values here are from 150°E, 180°, 150°W and 120°W at two month intervals over the period September 1981–July 1983.

APPENDIX C

Numerical convergence of methods

Results obtained via the finite difference (f.d.) method are compared to those obtained via the series method in order to check for correct numerical convergence. One such comparison is shown in Fig. 20 for the Model I Kelvin wave. Here values of σ computed by firstly the f.d. method and secondly the series method are plotted versus $1/N$, where N is the number of grid points (within the interval $0 \leq y' < +4.2$) or number of parabolic cylinder functions used. All other parameters and wavelengths are held constant. Both methods display convergence towards about the same

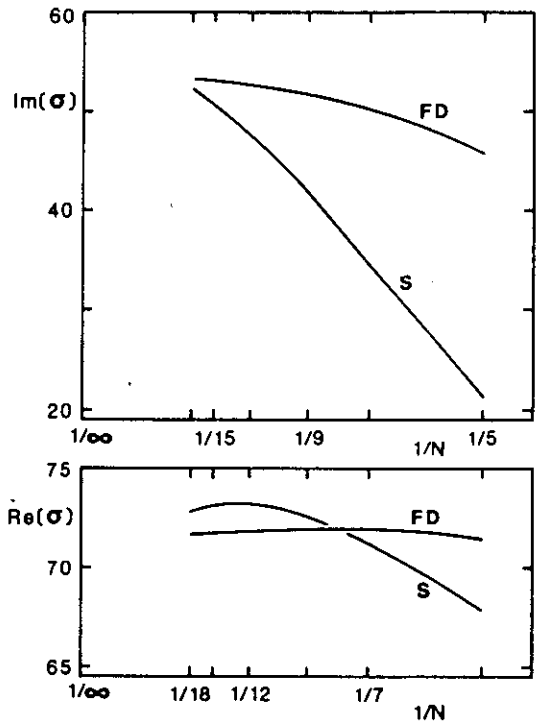

FIG. 20. Values of growth rate [Im(σ)] and frequency [Re(σ)] computed for the Model I Kelvin wave by the finite difference method (FD) and by the series method (S) as functions of $1/N$, where N is the number of internal grid points or symmetric parabolic cylinder functions used. Im(σ) and Re(σ) have units as in Fig. 1.

value [Im(σ) = +0.55, Re(σ) = +0.073] as N increases; the f.d. method displays the faster convergence. Similar comparisons involving other low n-modes in Models I–IV likewise indicate convergence agreement, however, the series method displays slow convergence at small k and at large c_a and A. The general agreement between the methods provides evidence for their correct convergence. Correct convergence of the f.d. method was further verified by a comparison of results obtained in the absence of coupling and known analytical values (Matsuno, 1966).

The accuracies of results in section 4 (computed using the f.d. method with $N = 12$) are estimated using convergence curves for the f.d. method such as that in Fig. 20. In each case, a true value of σ is estimated via linear extrapolation to $N = \infty$ using the σ values at $N = 15$ and $N = 18$. The difference between this "true value" and the value at $N = 12$ gives an estimate of the error in the $N = 12$ value. This procedure is expected to give an upper bound on the error since the f.d. method displays convergence of order greater than or equal to one [i.e. error in $\sigma \propto (\Delta y')^p$ with $p \geq 1$]. The f.d. method is found to undervalue the size of growth/decay rates for all modes except the damped Rossby modes in Model IV. When $N = 12$, errors in growth/decay rates are all less than 4% of the difference between estimated true value and prescribed ocean dissipation rate, except for $n = 2$ Rossby modes of Model II where errors are much larger (20%). The f.d. method also undervalues the frequency of Rossby modes by an amount that increases with meridional index and with $1/N$; similar undervaluation occurs even in the absence of coupling. When $N = 12$, errors in frequencies for the Kelvin and Model IV unstable modes are less than 1%, for the $n = 1$ Rossby and Model III unstable modes are between 3% and 7%, and for the $n = 2$ Rossby modes are 8% (Model IV) and 30% (Model II) of the estimated true value.

Eigenvectors for low n-modes obtained via the finite difference method similarly displayed satisfactory convergence.

REFERENCES

Albrecht, B. A., 1981: Parameterization of trade-cumulus cloud amounts. *J. Atmos. Sci.*, **38**, 97–105.

Anderson, D. L. T., and J. P. McCreary, 1985: Slowly propagating disturbances in a coupled ocean-atmosphere model. *J. Atmos. Sci.*, **42**, 615–629.

Arkin, P. A., J. D. Kopman and R. W. Reynolds, 1983: *1982–1983 El Niño/Southern Oscillation Event Quick Look Atlas.* Climate Analysis Center, NOAA/National Weather Service, Washington, DC, 79 pp.

Busalacchi, A. J., and M. A. Cane, 1985: Hindcasts of sea level variations during the 1982–83 El Niño. *J. Phys. Oceanogr.*, **15**, 213–221.

Garwood, R. W., 1977: An oceanic mixed layer capable of simulating climatic stress. *J. Phys. Oceanogr.*, **7**, 455–468.

Gill, A. E., 1980: Some simple solutions for heat-induced tropical circulation. *Quart. J. Roy. Meteor. Soc.*, **106**, 447–462.

——, 1982: Changes in thermal structure of the equatorial Pacific during the 1972 El Niño as revealed by bathythermograph observations. *J. Phys. Oceanogr.*, **12**, 1373–1387.

——, 1983: An estimation of sea-level and sea-current anomalies during the 1972 El Niño and consequent thermal effects. *J. Phys. Oceanogr.*, **13**, 586–605.

——, 1985: Elements of coupled ocean-atmosphere models for the tropics. *Coupled Ocean-Atmosphere Models*, J. C. J. Nihoul, Ed., Elsevier Oceanography Series, **40**, Elsevier, 303–327.

——, and E. M. Rasmusson, 1983: The 1982–83 climate anomaly in the equatorial Pacific. *Nature*, **306**, 229–234.

Harrison, D. E., and P. S. Schopf, 1984: Kelvin-wave-induced anomalous advection and the onset of surface warming in El Niño events. *Mon. Wea. Rev.*, **112**, 923–933.

Hastenrath, S., and L. Heller, 1977: Dynamics of climate hazards in northeast Brazil. *Quart. J. Roy. Meteor. Soc.*, **103**, 77–92.

——, and P. J. Lamb, 1977: *Climatic Atlas of the Tropical Atlantic and Eastern Pacific Oceans.* University of Wisconsin Press, 113 pp.

——, and ——, 1978: *Heat Budget Atlas of the Tropical Atlantic and Eastern Pacific Oceans.* University of Wisconsin Press, 90 pp.

Hirst, A. C., 1985: Free equatorial instabilities in simple coupled atmosphere-ocean models. *Coupled Ocean-Atmosphere Models*, J. C. J. Nihoul, Ed., Elsevier Oceanography Series, **40**, Elsevier, 153–165.

Horel, J. D., and J. M. Wallace, 1981: Planetary-scale atmospheric phenomena associated with the Southern Oscillation. *Mon. Wea. Rev.*, **109**, 813–829.

Khalsa, S. J. S., 1983: The role of sea surfce temperature in large-scale air–sea interaction. *Mon. Wea. Rev.*, **111**, 954–966.

Lau, K. M., 1981: Oscillations in a simple equatorial climate system. *J. Atmos. Sci.*, **38**, 248–261.

——, and P. H. Chan, 1983: Short term variability and atmospheric teleconnections from satellite-observed outgoing longwave radiation. Part I: Simultaneous relationships. *J. Atmos. Sci.*, **40**, 2735–2750.

Lim, H., and C. P. Chang, 1983: Dynamics of teleconnections and Walker circulations forced by equatorial heating. *J. Atmos. Sci.*, **40**, 1897–1915.

Matsuno, T., 1966: Quasi-geostrophic motions in the equatorial area. *J. Meteor. Soc. Japan.*, **44**, 25–42.

Niiler, P., and E. B. Kraus, 1977: One-dimensional models of the upper ocean. *Modelling and Prediction of the Upper Layers of the Ocean*, E. B. Kraus, Ed., Pergamon, 143–172.

Paulson, C. A., and J. J. Simpson, 1977: Irradiance measurement in the upper ocean. *J. Phys. Oceanogr.*, **7**, 952–956.

Philander, S. G. H., and E. M. Rasmusson, 1984: On the evolution of El Niño. *Trop. Ocean-Atmos. Newslett.*, **24**, D. Halpern, Ed., JISAO, University of Washington, 16.

——, T. Yamagata and R. C. Pacanowski, 1984: Unstable air-sea interactions in the tropics. *J. Atmos. Sci.*, **41**, 604–613.

Rammage, C. S., C. W. Adams, A. M. Hori, B. J. Kilonsky and J. C. Sadler, 1980: *Meteorological Atlas of the 1972–73 El Niño.* UHMET 80-03, Dept. of Meteorology, University of Hawaii, 101 pp.

Rasmusson, E. M., and T. H. Carpenter, 1982: Variations in tropical sea surface temperature and surface wind fields associated with the Southern Oscillation/El Niño. *Mon. Wea. Rev.*, **110**, 354–384.

Rennick, M. A., 1983: A model of atmosphere-ocean coupling in El Niño. *Trop. Ocean-Atmos. Newslett.*, **15**, D. Halpern, Ed., JISAO, University of Washington, 2–4.

——, and R. L. Haney, 1985: Stability of some simple coupled models. *Trop. Ocean-Atmos. Newslett.* **29**, D. Hansen, Ed., NOAA/AOML, Miami, 18–19.

Reynolds, R., 1982: A monthly averaged climatology of SST. NOAA Tech. Rep. NWS-31, 35 pp.

Wyrtki, K., and G. Meyers, 1975: The trade wind field over the Pacific Ocean. HIG-75-1, Hawaii Institute of Geophysics, University of Hawaii, 103 pp.

Yamagata, T., 1985: Stability of a simple air–sea coupled model in the tropics. *Coupled Ocean-Atmosphere Models*, J. C. J. Nihoul, Ed., Elsevier Oceanography Series, **40**, Elsevier, 637–657.

Zebiak, S. E., 1982: A simple atmospheric model of relevance to El Niño. *J. Atmos. Sci.*, **39**, 2017–2027.

Annu. Rev. Fluid Mech. 1994. 26 : 617–59

DYNAMICS OF COUPLED OCEAN-ATMOSPHERE MODELS: The Tropical Problem

J. David Neelin

Department of Atmospheric Sciences, University of California, Los Angeles, California 90024

Mojib Latif

Max-Planck-Institut für Meteorologie, D-20146 Hamburg 13, Federal Republic of Germany

Fei-Fei Jin

Department of Meteorology, University of Hawaii at Manoa, Honolulu, Hawaii 96822

KEY WORDS: Ocean-atmosphere interaction, climate variability, El Niño/Southern Oscillation

INTRODUCTION

Large-scale ocean-atmosphere interaction plays a crucial role in natural climate variability on a broad range of time scales and in anthropogenic climate change. The development of coupled ocean-atmosphere models is thus widely regarded as essential for simulating, understanding, and predicting the global climate system. Although these efforts typically benefit from years of previous work with atmospheric and oceanic models, coupling the two components represents a major step because of the new interactions introduced into the system. These can produce new phenomena, not found in either medium alone, the mechanisms for which present exciting theoretical problems. The removal of artificial negative feedbacks

0066–4189/94/0115–0617$05.00

produced by fixed boundary conditions in the uncoupled case also provides a stringent test of physical processes represented in both component models.

Pioneering work on coupling oceanic and atmospheric general circulation models (GCMs) began during the late 1960s and the 1970s (Manabe & Bryan 1969, Bryan et al 1975, Manabe et al 1975, Manabe et al 1979, Washington et al 1980). The difficulties encountered in obtaining accurate climate simulations with these models were sufficient that use of such coupled GCMs (CGCMs) did not gain momentum until the late 1980s and early 1990s. While the anthropogenic warming problem drove the development of global models (e.g. Gates et al 1985, Schlesinger et al 1985, Sperber et al 1987, Bryan et al 1988, Manabe & Stouffer 1988, Washington & Meehl 1989, Stouffer et al 1989, Manabe et al 1990, Cubasch et al 1992, Manabe et al 1992), evidence that ocean-atmosphere interaction is responsible for the El Niño/Southern Oscillation (ENSO) phenomenon provided a driving force in the development of models aimed at the tropical regions, both CGCMs and less complex models.

In this article, we consider the dynamics of coupled models relating to internal variability of the climate system that arises through ocean-atmosphere interaction. We focus on the tropical problem because it has been more thoroughly studied than the extratropical problem, and the crucial role of coupling has been clearly demonstrated. The field has developed to a stage that can be well summarized, and where short-range climate prediction is becoming a reality. A briefer section provides an indication of developments for the problem of coupled extratropical variability, which is in its infancy.

Despite the importance of coupled models to the study of anthropogenic global warming, we do not address this question beyond providing an indication of some of the difficulties these models face. It is the subject of many articles (e.g. Mitchell 1989, Houghton et al 1990, Gates et al 1992 and references therein) and merits a separate review. For other general references on coupled models, we note a review of global CGCMs (Meehl 1990a), a textbook on the tropical problem (Philander 1990), edited volumes on climate modeling (Trenberth 1993, Schlesinger 1990), and selected conference proceedings (Nihoul 1985, 1990; Charnock & Philander 1989).

COUPLED OCEAN-ATMOSPHERE MODELS

A hierarchy of complexity exists in climate models, the most complex being the atmospheric, oceanic, and coupled general circulation models (AGCMs, OGCMs, and CGCMs; for these and other acronyms, see Table 1). GCMs are generally based on the primitive equations (a filtered version

of the Navier-Stokes equations; e.g. Washington & Parkinson 1986), with detailed parameterizations of sub-grid-scale processes (e.g. turbulent mixing, and for AGCMs radiative transfer and moist convection). These attempt to simulate an approximation to both the climatology and natural variability. A variety of models based on further approximations are used for particular applications; often these are formulated as anomaly models about a specified climatology. Coupling considerations tend to be similar—we outline the procedures as applied to GCMs. The class of models often used in global warming studies in which the ocean acts only as a heat capacitor—and has no active dynamics—is not discussed.

For climate time scales, a division of the coupled system at the ocean-atmosphere interface is not easy to defend. Incoming solar (shortwave) radiation is primarily absorbed at the ocean surface and energy is lost through evaporation, infrared (longwave) radiation, and sensible heat fluxes to the atmosphere, which in turn re-emits longwave radiation to space. The one-dimensional equilibrium of these processes (and the strength of the negative feedback to perturbations from this equilibrium) provides a first approximation to the climate, modified of course by three-dimensional transports and feedbacks in both media. Interrupting this exchange at the ocean surface is questionable on time scales longer than a few months (shorter for some phenomena). Historically, however, this division permitted atmospheric and oceanic modelers to concentrate purely on problems in their respective media, as necessitated by the complexity of these subsystems. Since the parameterization of sub-grid-scale processes is one of the most crucial aspects of climate modeling, this separate development may be partially justified by arguing that the difference in density and effective heat capacity is sufficient that individual parameterizations of fast sub-grid processes may be developed initially in uncoupled models. The limitations of this approach will no doubt be re-examined when coupled models reach a more mature stage. Surface heat flux boundary conditions for uncoupled ocean models are particularly problematic (e.g. Bretherton 1982, Seager et al 1988) since the negative feedback on sea surface temperature (SST) involves the atmospheric response.

Table 1 Acronyms used in the text

ENSO	El Niño/Southern Oscillation
GCM	General Circulation Model
AGCM/CGCM/OGCM	Atmospheric/Coupled/Ocean GCM
HCM	Hybrid Coupled Model
ICM	Intermediate Coupled Model
SSO regime	Standing-SST Oscillatory regime
SST	Sea Surface Temperature

In a typical coupling scheme for an ocean-atmosphere model, the ocean model passes SST to the atmosphere, while the atmosphere passes back heat flux components, freshwater flux, and horizontal momentum fluxes (*surface stress*—oceanographic usage refers only to stress tensor components associated with vertical fluxes of horizontal momentum). Land temperature is necessarily computed interactively, with parameterizations ranging from the zero heat-capacity approximation to more complex land-surface models (e.g. Dickinson 1983). The numerical coupling interval (over which interfacial variables are averaged before being passed) is chosen for computational convenience or to satisfy assumptions of physical parameterizations. Although heat fluxes are calculated using the atmospheric boundary-layer parameterizations based on SST from the previous interval, the important dependence of heat flux on SST is retained as long as the heat flux coupling interval is sufficiently small.

The atmospheric response to SST is rapidly redistributed vertically, especially in convective regions, and is nonlocal horizontally on time scales longer than dynamical adjustment times—on the order of a few days to a month. For most purposes, the atmosphere can be assumed to be in statistical equilibrium with given SST (and land/ice/snow) boundary conditions on time scales longer than a season. The ocean responds on a wide range of time scales, from days (for some features of the mixed layer) to millenia (for the deep-ocean thermal adjustment). It is thus common to characterize the ocean as having the *memory* of the system. For global coupled models where the deep ocean is integrated to equilibrium, asynchronous coupling techniques are sometimes used (e.g. Manabe et al 1979).

Climate drift—i.e. departure of the model climatology from the observed (and from the climate simulated by the component models in uncoupled tests)—is a common problem in coupled models. It often appears as a slow adjustment away from initial conditions towards an internal equilibrium, hence the term "drift;" it may also refer to cases of faster adjustment and to the error at equilibrium. Although numerics contribute, climate drift arises primarily from the cumulative effects of errors in the sub-grid parameterizations; as such the process of correcting it based on careful physical arguments can be slow and painstaking. In cases where the sources of drift are well separated from mechanisms governing the geophysical phenomena of interest, it has been argued (e.g. Manabe & Stouffer 1988, Sausen et al 1988) that correcting the drift by a *flux correction* may permit progress even with an imperfect model. Roughly speaking, the model's equilibrium climatology of all or some of the interfacial variables is subtracted and replaced with observed values that are passed between subsystems; effectively the model is only used to compute

anomalies from climatology. The success of flux-correction techniques depends on the problem.

Coupled models designed for the tropical problem do not treat the deep-ocean thermohaline circulation which maintains cold waters at depth. Typically the ocean basin is simply interrupted at some latitude, using a sponge layer (with temperature and salinity strongly constrained toward climatological values) to avoid effects of the artificial boundaries propagating into the region of interest via wall-trapped Kelvin waves. Observed climatological SST is specified in the ocean regions which are not actively modeled. Other models simulate the upper ocean only, with motionless deep waters (e.g. Gent & Cane 1989). Additional design specifications for the tropical problem include the use of sufficiently high-resolution ocean components to resolve equatorial wave dynamics with characteristic meridional scales of order 2° latitude. For the global problem, the ocean models typically are used with coarser resolution because of the necessity of very long integrations for equilibration.

THE TROPICAL PROBLEM

Background

Ocean-atmosphere interaction is particularly amenable to study in the tropics because at large scales each medium is strongly controlled by the boundary conditions imposed by the other. The upper ocean circulation is largely determined by the past history of the wind stress with little internal variability; likewise the major features of the tropical atmospheric circulation are determined by the SST, with internal variability largely confined to time scales less than 1–2 months. This contrasts to the midlatitude situation where internal variability of both atmosphere and ocean is large.

THE BJERKNES HYPOTHESIS Because the ENSO phenomenon is the largest signal in interannual climate variability, it has dominated the literature; here we bring in other aspects of the tropical problem where possible. The reigning paradigm for ENSO dynamics is that it arises through ocean-atmosphere interaction in the tropical Pacific (although its influence extends globally and interactions with other parts of the climate system are by no means excluded), as first hypothesized by Bjerknes (1969). The essence of Bjerknes' postulate still stands as the basis of present day work—that ENSO arises as a self-sustained cycle in which anomalies of SST in the Pacific cause the trade winds to strengthen or slacken, and that this in turn drives the changes in ocean circulation that produce anomalous SST. Within this paradigm, one may still distinguish a variety of mech-

anisms that potentially contribute to the maintainance and time scale of the cycle; these have provided challenges for both theory and simulation.

MODEL HIERARCHY Beginning at about the same time as Bjerknes' hypothesis was formulated, the foundations for modeling the tropical coupled system were laid through the study of the individual physical components. The dynamics of the equatorial ocean response to wind stress were examined in shallow-water models representing the upper ocean (e.g. Moore 1968; Cane & Sarachik 1977, 1981; McCreary 1976), modified shallow-water models (e.g. Cane 1979, Schopf & Cane 1983), and ocean general circulation models (OGCMs; e.g. Philander & Pacanowski 1980, Philander 1981). And in the atmosphere, it was demonstrated semi-empirically that simple atmospheric models with steady, damped shallow-water dynamics could provide a reasonable approximation to the low-level tropical atmospheric response to SST anomalies (e.g. Matsuno 1966, Gill 1980, Gill & Rasmusson 1983). There is still disagreement as to the best formulation of these simple atmospheric models (Zebiak 1986, Lindzen & Nigam 1987, Neelin & Held 1987, Neelin 1989a, Allen & Davey 1993) but their simulation of anomalous wind-stress feedbacks to the ocean from given SST is given credence by AGCM simulations (e.g. Lau 1985, Palmer & Mansfield 1986, Mechoso et al 1987, Shukla & Fennessey 1988, and references therein).

As a result of the development of complementary models of varying degrees of complexity, the tropical coupled problem has benefited from a full hierarchy of models. The basis for a more quantitative understanding of coupled ocean-atmosphere interaction was initially provided by coupled models constructed from variations on modified shallow-water ocean and simple atmospheric models: both in simple linear versions (Lau 1981a; Philander et al 1984; Gill 1985; Hirst 1986, 1988; Wakata & Sarachik 1991; Neelin 1991) and in nonlinear versions (e.g. Cane & Zebiak 1985, Anderson & McCreary 1985, Zebiak & Cane 1987, Battisti 1988, Battisti & Hirst 1989, Schopf & Suarez 1988, Yamagata & Masumoto 1989, Graham & White 1990). The simplest linear shallow-water models, together with some useful models that condense the dynamics even further, are loosely referred to as *simple models*, while the more complex and carefully parameterized of the modified shallow-water models are often referred to as *intermediate coupled models* (ICMs). The next step up the model hierarchy, in order of increasing complexity, is the *hybrid coupled models* or *HCMs*. These consist of an ocean GCM coupled to a simpler atmospheric model (e.g. Neelin 1989b, 1990, Latif & Villwock 1990, Barnett et al 1993), the justification being that the ocean contains both the memory and limiting nonlinearity of the system—the atmosphere is thus treated as the fast component of a stiff system. The most complex models are the coupled GCMs in which

both components include relatively complete sub-grid parameterization packages (e.g. Philander et al 1989, 1992; Lau et al 1992; Sperber & Hameed 1991; Gordon 1989; Meehl 1990b; Nagai et al 1992; Mechoso et al 1993; Neelin et al 1992). It should be noted that the divisions in the hierarchy are not sharp and some of the lowest-resolution CGCMs may not be much more complex than the best ICMs. Many of these models produce interannual variability through coupled interactions which have significant parallels to ENSO dynamics.

Our approach here is to summarize basic phenomenological features from a modeler's point of view (i.e. we do not attempt a complete review of the large observational literature) in the *Observations* section, and then to present a cross-section of model results in the *Simulation* section, which includes selected intermediate models as well as CGCMs and HCMs. The *Theory* section makes use of intermediate and simple models to outline basic mechanisms of interaction, describes the manner in which different mechanisms combine and contribute to the sensitivity of the coupled system, and details the current understanding of the bifurcation structure. Many of the theoretical considerations prove useful in understanding results of the more complex models.

Observations

Aspects of El Niño and the Southern Oscillation were known individually long before any connection was made. The term "El Niño," which originated with Peruvian fishermen, now refers to strong warmings of surface waters through the eastern and central equatorial Pacific that last about a year (e.g. Rasmusson & Carpenter 1982, Deser & Wallace 1990). Although it is common to refer to these as "events," they exhibit a distinct oscillatory behavior now understood to be part of a low frequency cycle. The Southern Oscillation was discovered by Walker (1923), and its global scale was inferred early on (Belarge 1957) from correlation maps of sea-level pressure anomalies which exhibit anomalies of opposite sign in the eastern and western hemisphere. The larger scale of this pattern relative to the SST anomaly is typical of the atmosphere's nonlocal response to boundary conditions. The strong relationship between interannual variability of SST and sea-level pressure may be seen in Figure 1.

As a background to understanding ENSO-related interannual variability, a brief description of the time-mean circulation is required. Differential forcing of the atmosphere by the SST boundary condition thermodynamically drives direct circulation cells: convection tends to organize roughly over the warmest SST, producing regions of strong surface convergence (known as intertropical convergence zones). The zonally-symmetric (i.e. averaged around latitude circles) component of this circulation

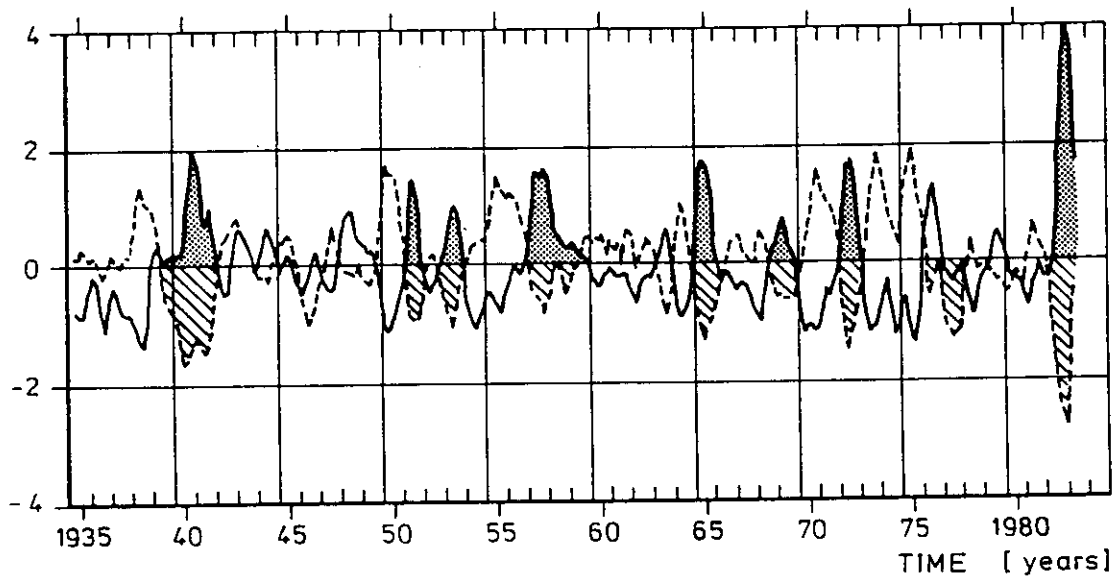

Figure 1 Time series of the Southern Oscillation Index, which measures the atmospheric sea-level pressure gradient across the tropical Pacific basin (*dashed curve*), and sea surface temperature (SST) anomalies at Puerto Chicama, Peru (*solid curve*). Both series are normalized by their standard deviation; shading indicates major ENSO warm phases (high SST, low Southern Oscillation Index). After Rasmusson (1984).

is referred to as the *Hadley circulation*, the zonally-asymmetric component as the *Walker circulation*. The Hadley circulation contributes an easterly (i.e. westward) component to tropical surface winds. This is strongly reinforced over the tropical Pacific by the Walker circulation driven by the strong SST gradient across the basin between the warm waters in the west and the cooler eastern waters.

The westward wind stress has a strong impact on the ocean circulation. The input of momentum is balanced, in a vertical average, largely by pressure gradients in the upper ocean. A sea-level gradient of about 40 cm across the Pacific is compensated by a slope in the *thermocline* (the interface that separates the well-mixed, warm surface waters from the cold waters at deeper levels) which slopes upward to the east. Within the upper ocean, the differential deposition of stress by vertical viscosity drives westward surface currents along the equator, and Ekman drift due to the Coriolis force to either side of the equator drives a narrow band of upwelling along the equator, especially under the regions of strong easterlies in the eastern/central Pacific. The combination of upwelling and shallow thermocline produces the *equatorial cold tongue* in the east, while the deep thermocline in the west is associated with warm SST—the western Pacific *warm pool*.

The important dependence of SST in the equatorial cold tongue region on wind-driven ocean dynamics (rather than just on air-sea heat exchange) and the Walker circulation response to anomalies in the SST pattern form the key elements of the Bjerknes hypothesis. Consider an initial positive SST anomaly in the eastern equatorial Pacific. This anomaly reduces the zonal SST gradient and hence the strength of the Walker circulation, resulting in weaker trade winds at the equator. This leads to a deeper thermocline and reduced currents and produces higher surface temperatures in the cold tongue region, further reducing the SST gradient in a positive feedback which can lead to instability of the climatological state via ocean-atmosphere interaction. The cyclic nature of the unstable mode depends on the time scales of response within the ocean. The details of what produces the cycle are subtle, as elaborated in the *Theory* section, but a concise observational picture motivated by theoretical considerations is provided by Latif et al (1993b).

Figure 2 shows characteristic anomaly patterns of three crucial quantities: zonal wind stress, SST, and the depth of the thermocline or upper ocean heat content, as measured by depth of the 20°C isotherm. The patterns represent an estimate of the dominant coupled ENSO mode as obtained by principal oscillation pattern analysis (Hasselmann 1988)—specifically, the leading eigenvector of the system matrix obtained by fitting a first-order Markov process to the data, where oscillations are represented by the cycle of patterns in temporal quadrature. The right panels show conditions during the warm phase of the ENSO cycle, i.e. during El Niño (the cold phase simply has reversed signs under this technique). Most of the tropical Pacific is covered by anomalously warm surface waters (Figure 2*d*), with maximum anomalies in the eastern equatorial Pacific. These SST anomalies are highly consistent with the patterns obtained by other techniques, including the well-known Rasmusson & Carpenter (1982) composites. The positive SST anomaly is accompanied by a westerly (eastward) zonal wind stress anomaly (Figure 2*b*) which reduces the mean Walker Circulation. Consistent with this feature, the tilt in the thermocline is reduced as indicated by the negative anomalies in the upper ocean heat content which are centered off the equator (Figure 2*f*).

The phase differences necessary to maintain the oscillation exist between sea surface temperature and wind on the one hand and upper ocean heat content on the other. As described in the *Theory* section, the ocean is not in equilibrium with the atmosphere and carries information associated with past winds that permits continuous oscillations. This feature is clearly seen during the transition phase in upper ocean heat content (Figure 2*e*) which shows a pronounced equatorially-trapped signal in the western Pacific. This signal appears not to be related to the contemporaneous

winds (Figure 2*a*), but rather was generated by anomalous eastward winds of the preceding cold phase (Figure 2*b*, but with reversed signs). Equatorial wave dynamics dictate that the heat content anomalies at latitudes larger than a few degrees propagate westward and reflect at the western maritime boundary into the equatorial wave guide. The transition phase SST (Figure 2*c*) does not show a clear signal; variations in SST can therefore be described to first order as a standing oscillation. Thus, it is the subsurface memory of the ocean that is crucial to ENSO (see e.g. Latif & Graham 1992 and Graham & White 1990 for additional observations).

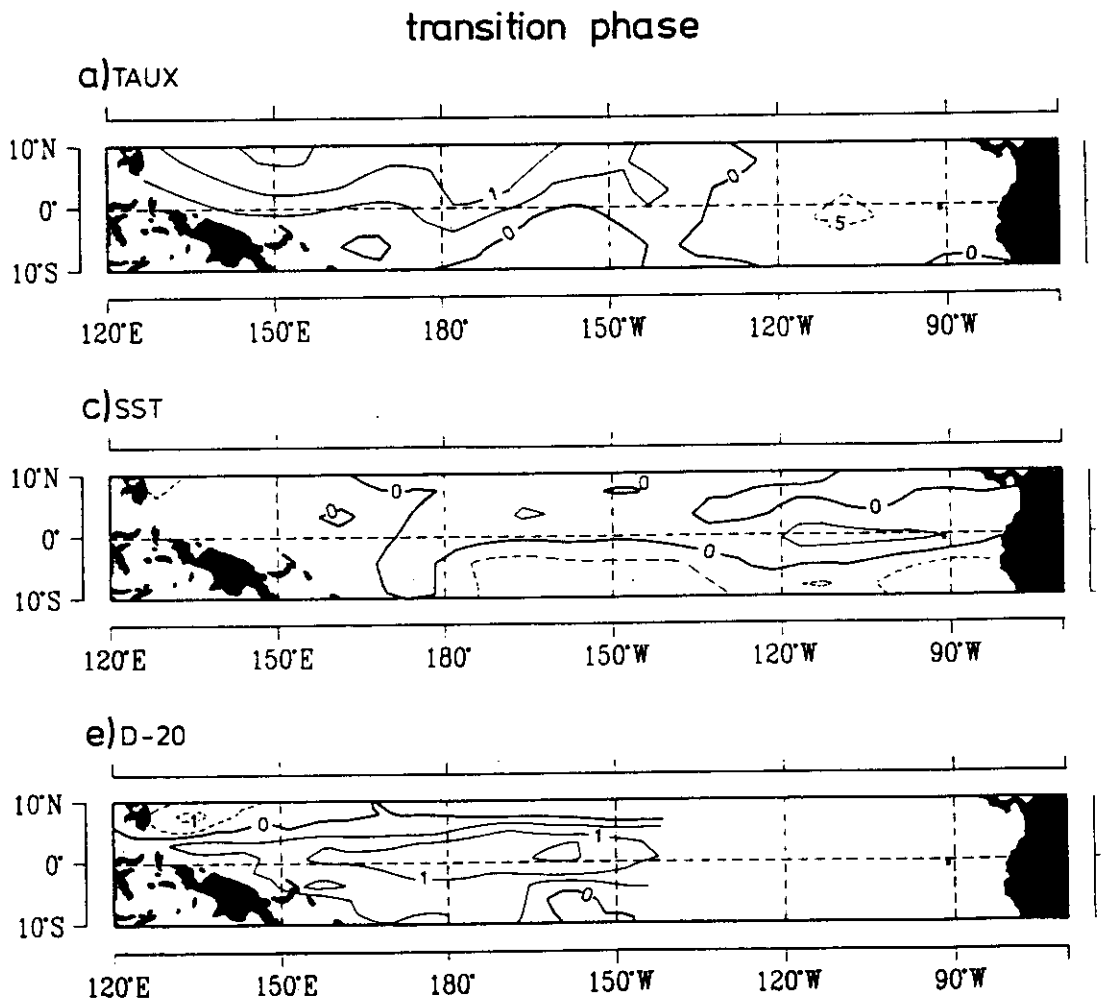

Figure 2 Spatial patterns of the dominant mode of ENSO variability as represented by the leading principal oscillation pattern (see text). The oscillation is represented by two time phases in quadrature during the cycle: transition phase (panels *a*, *c*, *e*) and extreme phase (panels *b*, *d*, *f*). (*a*), (*b*) wind stress anomaly, (*c*), (*d*) sea surface temperature anomaly, (*e*), (*f*) heat content anomaly as measured by the depth of the 20°C isotherm (blank areas in the eastern Pacific are due to lack of subsurface data). After Latif et al (1993b).

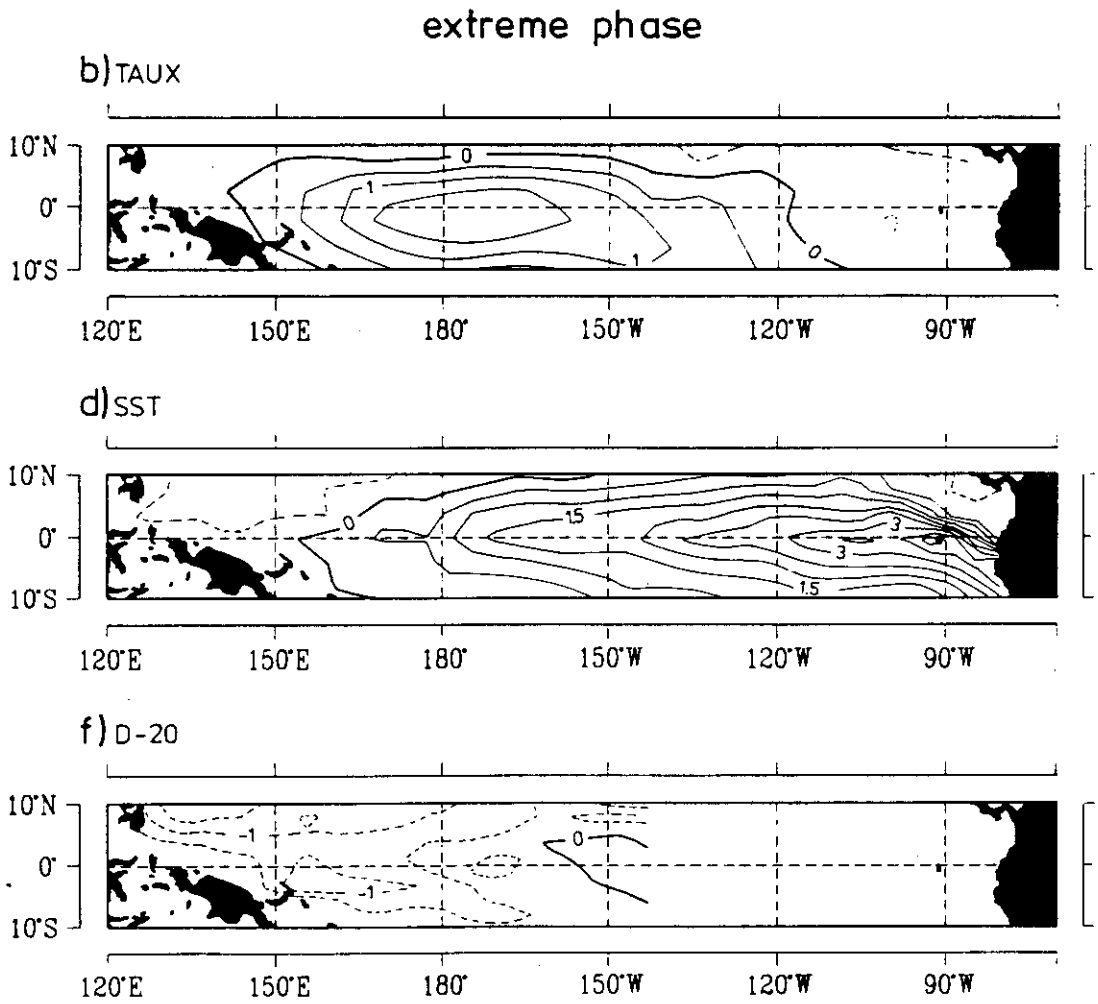

Figure 2 (continued).

The transition phase zonal wind stress (Figure 2*a*) shows a pronounced westerly anomaly centered over the northwestern Pacific so that the evolution in zonal wind stress is also characterized by a slowly eastward-propagating feature. The role of this propagation in maintaining the ENSO cycle, however, is still a controversial issue. Several authors have argued that this feature indicates a link to circulation systems over India, in particular the Monsoon (e.g. Barnett 1983).

A complementary view of the oceanic side of this feedback is provided by time-longitude plots of SST and a measure of thermocline depth anomalies along the equator (Figure 3). The time series is limited by the length of the records of ocean subsurface temperature. Even without statistical techniques, it is easy to pick out the dominant standing oscillation pattern

in SST (although some hints of propagation may be noted—see e.g. Gill & Rasmusson 1983, Barnett et al 1991), and the characteristic signature of subsurface memory—the lead of the heat content anomalies in the western part of the basin relative to the eastern part. Several coupled ocean-atmosphere models simulate variability patterns to those described above.

There is evidence that the spectral peak associated with ENSO may have a quasi-biennial component in addition to the dominant low-frequency

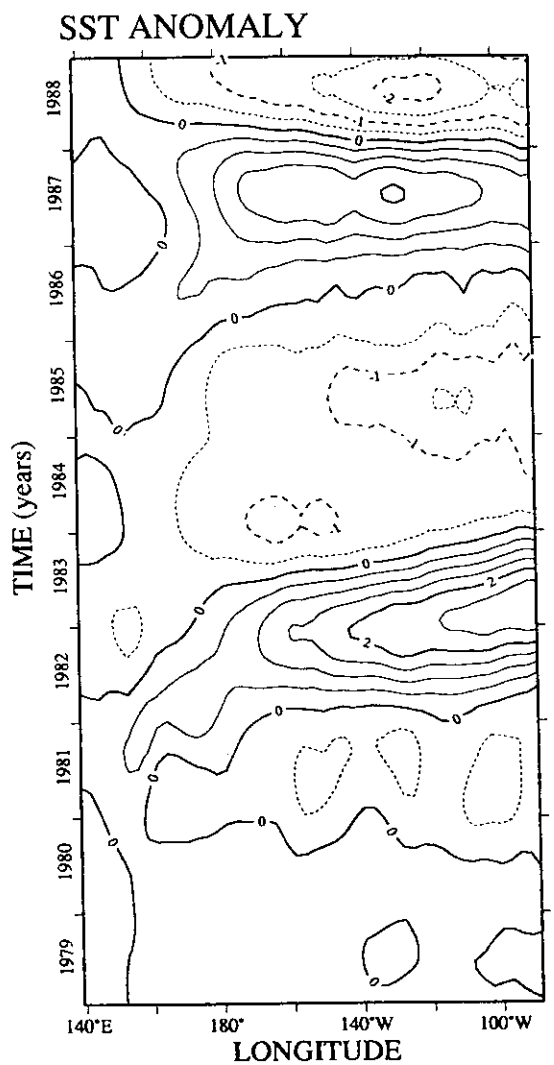

Figure 3 Time-longitude plot of observed anomalies along the equator. (*Left*) SST (contour interval 0.5°C). (*Right*) heat content integrated above 275 m (contour interval 100 °C m). The data have been low-pass filtered to remove variability on time scales smaller than 17 months. Data sets are described in Reynolds (1988) and Barnett et al (1993), respectively.

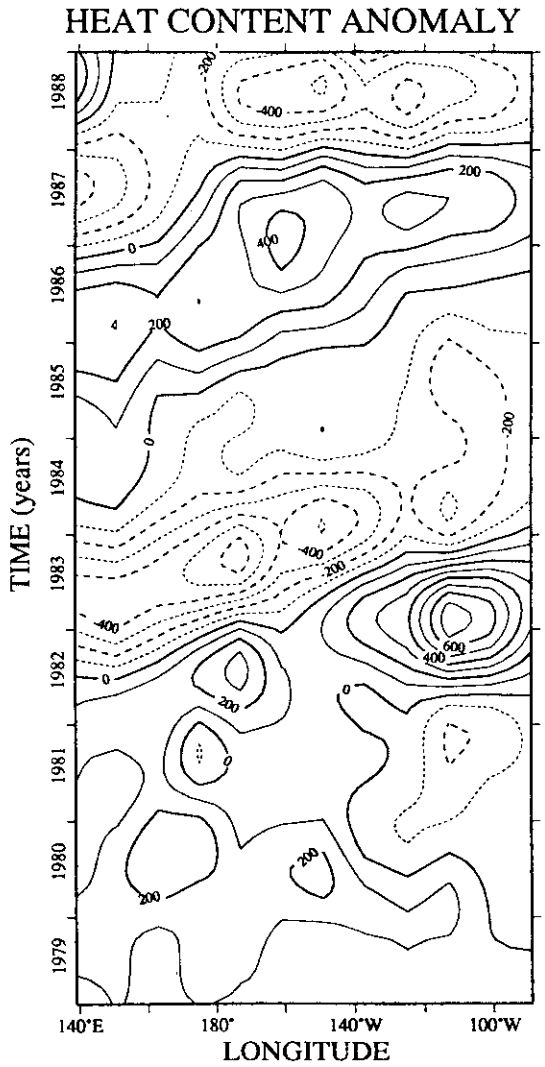

Figure 3 (continued).

(3–6 year) component, e.g. Rasmusson et al (1990), Latif et al (1993b). Spatial structures and interactions between assumed spectral bands have been examined, e.g. by Barnett 1991, Ropelewski et al 1992. For further discussion of ENSO observations see, for instance, Cane (1986), Rasmusson & Wallace (1983), Philander (1990), and references therein. Discussion of the seasonal cycle and interannual variability in the tropical Atlantic may be found in Lamb et al (1986), Lough (1986), Wolter (1989), Servain & Legler (1986), Philander & Chao (1991), Houghton & Tourre (1992), and Servain (1991), while Zebiak (1993) gives evidence that the latter may in part share similar dynamics to ENSO.

Models and Simulation

AN INTERMEDIATE MODEL The intermediate coupled model of Cane & Zebiak (1985, with Zebiak & Cane 1987; collectively CZ hereafter) has proven influential in ENSO studies and has provided the first successful ENSO forecasts with a coupled model (see *Prediction* section). A version of the ocean component is described in the *Theory* section. The atmosphere (Zebiak 1986) is one of several simple atmosphere models which attempt to improve on that of Gill (1980); drawbacks include lack of a moisture budget and formulation with discontinuous derivatives, but similar results are obtained with different atmospheric models (Jin & Neelin 1993a, N. Graham, personal communication). Figure 4 shows the SST and thermocline depth anomalies over one period of the simulated ENSO cycle from the linearized version of the CZ model used by Battisti & Hirst (1989) to examine the essential dynamics. The typical stationary oscillation in SST may be seen, with the lead of the western-basin thermocline-depth anomaly relative to the eastern basin characterizing the subsurface memory. The details of the transition between west and east differ from those observed because the simulated winds are shifted relative to observed winds, but the cycle is not strongly sensitive to this. Simulated ENSO events tend to resemble each other strongly in this model, and Battisti (1988) and CZ disagree over the degree of irregularity that can be generated by internal model dynamics, but there is reasonable consensus that basic elements of ENSO dynamics are captured.

INTERCOMPARISON OF GCM SIMULATIONS A recent comparison (Neelin et al 1992) of the tropical simulations of seventeen coupled ocean-atmosphere models, contributed by a dozen institutions worldwide, represents a snapshot at a relatively early stage of a rapidly developing field. We review some of the results, with the caveat that in the brief time since their collection, several of the models have made great progress in the accuracy of simulation and new models have been developed which are not yet published. The comparison was intended to give a feel for the sensitivity of the system modeled (possible in part because the models were not yet optimized), to point out common problems, and to provide a forum for discussing the broad range of coupled-model behavior.

The models were selected on the basis of having at least one component of sufficient complexity to be called a GCM, (i.e. CGCMs and HCMs), with two representatives of the ICMs—those of Cane & Zebiak (1985) and Schopf & Suarez (1988), the latter differing from a GCM principally by lack of a moisture budget. Some of the models are global, designed for global warming studies; others have a dynamically-active ocean only in the tropical Pacific, and were designed for the tropical problem. SST was

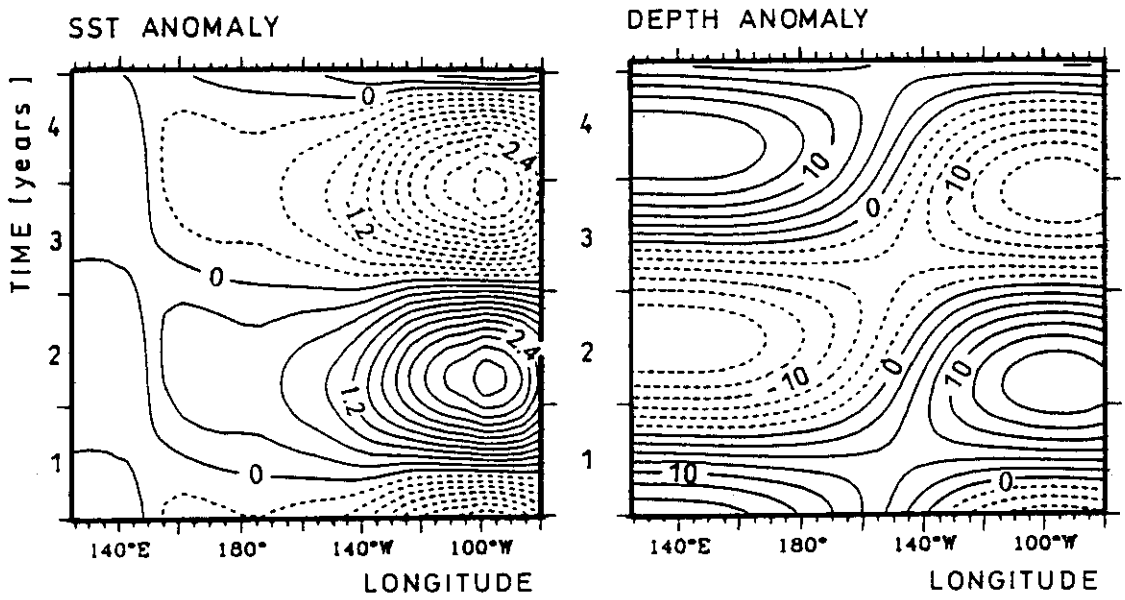

Figure 4 Time-longitude plot of anomalies along the equator from the Battisti & Hirst (1989) linearized version of the Cane & Zebiak (1985) intermediate coupled model. (*Left*) SST (contour interval 0.3°C). (*Right*) thermocline depth (contour interval 2.5 m). After Battisti & Hirst (1989).

chosen as the principle variable of comparison because of its crucial role in mediating the interactions.

Table 2 provides a summary of the results, augmented with more recent results where published, roughly classified according to the type of interannual variability and the simulation of climate in the equatorial Pacific. Models are listed as in Neelin et al (1992); the most closely related independent references available are Endoh et al (1991), Gent & Tribbia (1993), Gates et al (1985), Gordon (1989), Latif et al (1988), Latif et al (1993a), Lau et al (1992), Meehl (1990b), Neelin (1990), Philander et al (1992), Schopf & Suarez (1988), Sperber & Hameed (1991), Zebiak & Cane (1987). Many of the models exhibit climate drift. Some of the models, especially those with simplified atmospheres, sidestep this problem by flux correction. The category "Modest drift" as used here means only that the degree of drift in SST was relatively small by current (subjective) standards and comparable to that of uncoupled components. Interannual variability is weaker than observed in many of the models—the category "Weak interannual variability" means too weak to be classified.

Climate drift occurs in a variety of forms. A general cooling of large parts of the ocean basin is the most common form of slow drift. Fast climate drift is characteristically a coupled-dynamical effect leading to an

Table 2 Summary of models grouped according to common behavior for both tropical climatology and interannual variability as reflected in the sea surface temperature field (after Neelin et al 1992)

Variability	Climate		
	Modest drift	Flux corrected	Other
Weak interannual variability		Latif et al-1 Neelin-2[b,c] Oberhuber et al-1[d]	Gordon & Ineson-2[a] Gates et al[d,e] Cubasch et al[d,e] Oberhuber et al-2[d,e]
Interannual variability with zonal propagation of SST anomalies	Lau et al[d]	Neelin-1[b]	Meehl & Washington[a,d,f] Gates & Sperber[a,d,f] Tokioka et al[a,f]
Interannual variability with standing SST anomalies	Philander et al Gent & Tribbia Nagai et al (1992)[g] Mechoso et al (1993)[g]	Zebiak & Cane[b] Allaart et al[b,c]	Schopf & Suarez[a,b] Latif & Sterl[a]

[a] Slow cooling of warm regions.
[b] Model with simplified atmospheric component.
[c] Multiple climate states known or suspected.
[d] Model with global-domain ocean component.
[e] Weak zonal gradient; weak cold tongue.
[f] Cold tongue extended or cold tongue/warm pool boundaries displaced.
[g] Dates given for recently added references; otherwise see Neelin et al (1992).

overly-weak or overly-strong equatorial cold tongue. Three-dimensional feedbacks between SST, convection zones, wind stress, and ocean circulation qualitatively similar to those responsible for El Niño are seen to play a role in creating such drift or in exacerbating weaknesses in parameterizations controlling one-dimensional, vertical-column processes such as cloud-radiative interaction or vertical mixing. We note many situations where the position of the cold tongue migrates or extends within the basin, with a warm pool developing in the eastern part of the basin in some instances. The observed convection zone in the eastern Pacific stays north of the equator in all seasons; in some models it migrates across the equator with season. The similarities between the fast mode of climate drift to interannual phenomena of comparable time scale implies that, unlike numerical weather prediction—in which correction of climate drift was only addressed as the models matured—interannual climate forecasting with coupled GCMs must address the accurate simulation of certain aspects of the climatology at a relatively early stage.

We find that there is little relation between the presence of climate drift and the existence of significant interannual variability, so long as the cold

tongue is present somewhere in the basin. Interannual variability tends to come in two varieties: cases in which anomalies in SST, wind, etc propagate in the longitudinal direction along the equator and cases in which anomalies develop as a standing oscillation in the cold tongue region. In the latter case, fine ocean model resolution is required near the equator and subsurface memory due to oceanic adjustment processes is believed to determine the time scales; in the former case, coarse ocean model resolution does not preclude interannual oscillations and the time scales of ocean wave dynamics are not essential to the period.

Figure 5 provides an example of interannual variability from one of the first coupled GCMs with a high-resolution tropical ocean component (Philander et al 1989, 1992; Philander et al in Table 2). While the spectrum of interannual time scales may not exactly match that observed (possibly due to the removal of the seasonal cycle in this model for hypothesis-testing purposes), the spatial form, again with dominant standing oscillations in SST and with subsurface phase lags, is reasonably close to the observed form; Chao & Philander (1993) also compare these results to the uncoupled ocean component forced with obsrved winds to provide a longer surrogate time series for the subsurface anomalies. A number of other CGCMs have variations on this spatial form, some having clearer propagation characteristics in SST, combined with significant subsurface phase lags (e.g. Nagai et al 1992, Latif et al 1993a).

The rich variety of coupled phenomena found in these models serves as an indication of the sensitivity of the coupled system and lends support to qualitative arguments that coupled feedbacks are crucial in establishing tropical climate features. Even the most important features, such as the extent and position of the equatorial cold tongue and western Pacific warm pool, are not guaranteed to be reproduced in coupled GCMs. The lack of robustness in these features does not necessarily imply major faults in the models since coupled feedbacks can turn a small deficiency in one of the components into a significant departure in the coupled climatology. For example, a tendency of the atmospheric model to give slightly weak easterlies can result in a weaker cold tongue which in turn further weakens the Trades. In some models this can lead to a permanent warm state, although in others, weak AGCM stresses do not adversely affect either climatology or interannual oscillations.

Because the behavior of the coupled system can be qualitatively different (and difficult to anticipate) from that of the individual components, coupling should be regarded as a crucial part of the testing and development procedure for AGCMs and OGCMs being used for climate studies. In particular, the simulation of the warm-pool/cold-tongue configuration in the equatorial Pacific can represent a stringent test of the combined effects

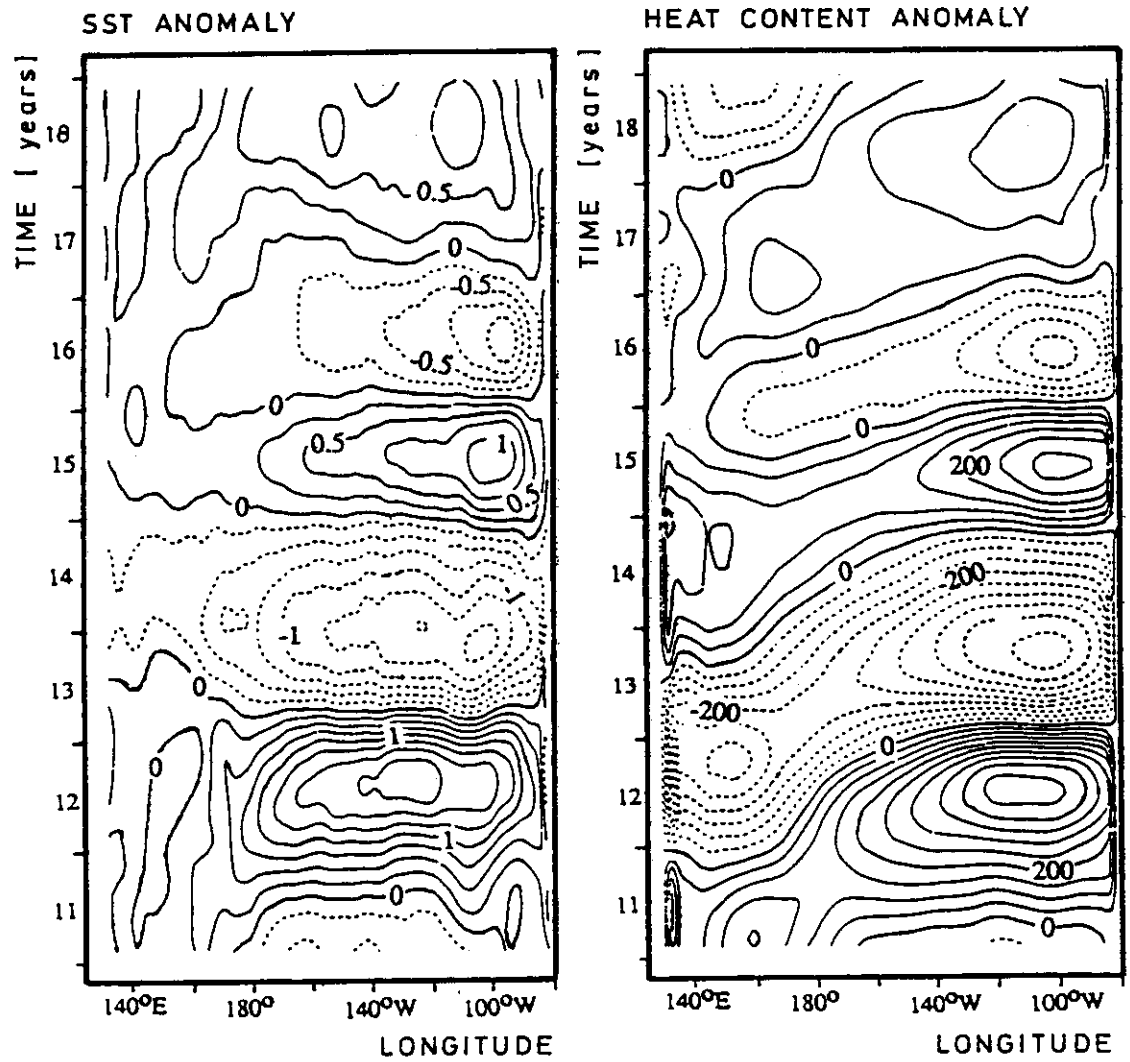

Figure 5 Time-longitude plot of anomalies along the equator from the Philander et al (1992) coupled GCM. (*Left*) SST (contour interval 0.25°C). (*Right*) heat content integrated above 300 m (contour interval 50 C° m). After Chao & Philander (1993). The data have been low-pass filtered to remove time scales less than 24 months.

of vertical-mixing parameterizations, interactive cloud-radiative schemes, and surface-flux parameterizations with the three-dimensional dynamics. The rate of improvement of recent model versions (both those in the table and currently unpublished models) is particularly encouraging in this respect.

Theory

CONTEXT AND HISTORY The considerable differences in the nature of the coupled variability produced by the different models above is related to

the sensitivity and the rich variety of flow regimes found in ICMs and simple models, which exhibit multiple mechanisms of coupled interaction. The character of the interannual variability in nonlinear models is largely determined by the first bifurcation from the climate state (Neelin 1990, Münnich et al 1991)—in other words by the leading unstable mode of the system linearized about the climatological state. Many of the most pressing questions about the range of coupled variability found in coupled models can thus be addressed by understanding the relation between flow regimes in the linear problem. To keep this multiparameter bifurcation problem tractable, the key is to choose a few crucial parameters that capture the range of behavior of interest, and to map out the connections among regimes close to that of the real system and those that provide useful simplifications.

In the literature, the search for simple prototype systems to provide conceptual analogs for the modes of coupled variability has led in a number of apparently contradictory directions, and it is desirable to bring these together. We approach this by presenting first a version of the CZ ICM scaled to highlight parameters used to show these connections succinctly. We derive three important simple models from this and discuss the differing idealizations. We then return to the ICM to show how the simple models relate to the connections between eigenmodes in the coupled parameter space. This completes the discussion of the primary bifurcation, i.e. how the period and spatial form of the ENSO cycle are determined and its maintenance through instability of the climatological state. We conclude with a discussion of higher bifurcations and describe what is known about the sources of irregularity in the ENSO cycle.

In ordering the presentation to emphasize a unified view, the historical aspects are necessarily simplified, so we preface with a brief overview of the literature (see also McCreary & Anderson 1991, Ghil et al 1991). Early theoretical work includes low-order models by McWilliams & Gent (1978) and some nonrotating coupled cases (Lau 1981a). Models by McCreary (1983) and McCreary & Anderson (1984) have often been omitted from recent citation because of the use of a discontinuous switch in their atmosphere, but elements of their discussion of basin adjustment processes have been incorporated in later work. Philander et al (1984) presented the first linear instability study in a coupled modified-shallow-water system, and refinements and additional mechanisms were elaborated numerically in Gill (1985), Yamagata (1985), Hirst (1986, 1988), Battisti & Hirst (1989), Wakata & Sarachik (1991), and analytically in Neelin (1991). Nonlinear solutions in ICMs were introduced in Cane & Zebiak (1985) and Zebiak & Cane (1987), in a regime now felt to approximate that of the observed, and by Anderson & McCreary (1985), Yamagata & Masumoto (1989) in

a different regime; hints at regime connections may be found in Xie et al (1989) and Wakata & Sarachik (1991).

Much of the terminology used in these papers is based on the Rossby and Kelvin modes of the uncoupled ocean in an infinite or periodic basin, presumably because these are most familiar to oceanographers. A significant step toward thinking in terms of the fully coupled problem was advanced by Schopf & Suarez (1988) and Suarez & Schopf (1988) using a simple model with a single spatial variable to explain the oscillation in their ICM; Battisti & Hirst (1989) showed that a version of this model could be fitted to a number of important aspects of the oscillation in the CZ model, and that the Hopf-bifurcation regime was the physically relevant one. Referred to hereafter as the *SSBH delayed-oscillator model*, it consists of a differential-delay equation representing the time evolution of SST averaged over a small eastern equatorial box, with a net growth tendency representing local positive feedback mechanisms due to coupling and a delayed negative feedback representing the equatorial-wave adjustment process; whether the latter can be interpreted literally in terms of off-equatorial Rossby wave packets reflecting from the western boundary has been the subject of debate (Graham & White 1988, Battisti 1989, Chao & Philander 1993). The model is designed to represent the regime in which SST variability occurs as a standing oscillation in the strongly-coupled eastern basin, and in which time scales of ocean wave dynamics provide the memory of the system essential to the oscillation.

On the other hand, there exists a large class of coupled regimes in which ocean wave dynamics is not essential to interannual oscillation. In an idealized limit (the *fast-wave limit*), coupled modes are associated with the time derivative of the SST equation, and hence referred to as *SST modes*. These do involve subsurface ocean dynamics, but the time-dependence of this component is secondary. A distorted-physics method for testing this (involving articicial multipliers on selected OGCM time derivatives) was employed in Neelin (1991) to show the relevance of this limit to oscillations in one flow regime of an HCM. Hirst (1986, 1988) and Neelin (1991) showed, by numerical and analytical methods respectively, that a number of physical processes cooperate in the destabilization of SST modes whereas they compete in terms of the direction of propagation. Propagation is essential to the period in these modes and they provide a good prototype for slowly-propagating modes in a number of intermediate models and GCMs (e.g. Anderson & McCreary 1985, Yamagata & Masumoto 1989, Meehl 1990b, Lau et al 1992).

Because the SSBH delayed-oscillator model is based on the SST equation, it was natural to hypothesize that nonpropagating SST modes away from the fast-wave limit might be perturbed by wave time scales to

produce standing oscillations. Such a connection is inherent in the analysis of Wakata & Sarachik (1991) in which the relation between a propagating regime of Hirst (1988) and a standing oscillation regime is demonstrated. In an apparent contradiction, two models aimed at producing more rigorous derivations of the SSBH delayed oscillator (Cane et al 1990 plus Münnich et al 1991, MCZ hereafter; and Schopf & Suarez 1990) emphasize a rather different limit. These models also assume that the coupling occurs at a single point rather than across all or most of the basin. SST-mode solutions in the fast-wave limit allow an analytical approach to the spatial structure of the coupled modes, inclusion of several growth mechanisms, and a determination of their relation to propagating regimes, but at the cost of eliminating subsurface memory. Jin & Neelin (1993a,b) and Neelin & Jin (1993; collectively JN hereafter) outlined the complementarity between these approaches and the usefulness of analytical prototypes which include solutions for the spatial structure of the coupled modes in various limits.

INTERMEDIATE COUPLED MODEL We present here the JN "stripped-down" version of the CZ ICM, as a basis for deriving simpler models and discussing flow regimes. We nondimensionalize to bring out a few *primary parameters* from among the many lurking in the coupled system. These are:

μ: the relative coupling coefficient—strength of the wind-stress feedback from the atmosphere per unit SST anomaly, scaled to be order unity for the strongest realistic coupling; for $\mu = 0$ the model is uncoupled.
δ: the relative adjustment time coefficient—measures the ratio of the time scale of oceanic adjustment by wave dynamics to the time scale of adjustment of SST by coupled feedback and damping processes. It is scaled to be order unity at standard values of dimensional coefficients.
δ_s: surface-layer coefficient. This parameter governs the strength of feedbacks due to vertical-shear currents and upwelling, (u_s, v_s, w_s), created by viscous transfer between the surface layer and the rest of the thermocline. As $\delta_s \to 0$ the effects of these feedbacks become negligible.

A modified shallow-water model with an embedded, fixed-depth mixed layer (Cane 1979, Schopf & Cane 1983) provides the ocean-dynamics component:

$$\begin{aligned}(\delta\partial_t + \varepsilon_m)u'_m 2 - yv'_m + \partial_x h' &= \tau' \\ yu'_m + \partial_y h' &= 0 \\ (\delta\partial_t + \varepsilon_m)h' + \partial_x u'_m + \partial_y v'_m &= 0 \end{aligned} \tag{1}$$

$$\varepsilon_s u'_s - y v'_s = \delta_s \tau'$$
$$\varepsilon_s v_s + y u'_s = 0, \tag{2}$$

where latitude, y, appears due to the nondimensionalized Coriolis force and the equations are applied here to departures (primed quantities), from a specified climatology (denoted by an overbar). Anomalous vertical mean currents above the thermocline, (u'_m, v'_m), and thermocline depth, h', are governed by the shallow-water component in the long-wave approximation (1), with suitable boundary conditions at basin boundaries (Gill & Clarke 1974); vertical shear currents, (u'_s, v'_s), are governed by local viscous equations (2). Both are driven by the zonal wind stress anomaly, τ'. The damping rates, ε_m and ε_s are not treated as primary parameters because the former is small and the latter can be largely absorbed into δ_s. For a more formal scaling see JN; for justification of several approximations, see Cane (1979) and CZ. Vertical velocities are given by the divergence of the horizontal velocities and the values of surface currents and upwelling into the surface layer by the sum of anomalous mean and shear contributions plus the climatology: $u = \bar{u} + u'_m + u'_s$, $w = \bar{w} + w'_m + w'_s$.

Because SST serves as a key interfacial variable, careful parameterization of processes that affect SST are largely responsible for the success of the CZ model. The direct effects of temperature variations in the surface layer on pressure gradients are neglected in (1), but a prognostic equation for SST is carried separately which contains all the essential nonlinearity of the CZ model:

$$\partial_t T + u\partial_x T + \mathrm{H}(w)w(T - T_{sub}) + v\partial_y T + \varepsilon_T(T - T_0) = 0 \tag{3}$$

in nondimensional form. Here T is total SST and H is an analytic version of the Heaviside function due to upstream differencing into the surface layer. The Newtonian cooling represents all physical processes that bring SST towards a radiative-convective-mixing equilibrium value, T_0. The subsurface temperature field, T_{sub}, characterizes values upwelled from the underlying shallow-water layer and is parameterized nonlinearly on the thermocline depth—deeper thermocline results in warmer T_{sub}. Motivated by the fact that the strongest SST response to upwelling, advection, and thermocline depth change are confined to a fairly narrow band along the equator for the phenonena of interest, Neelin (1991) applied this equation to the SST in an equatorial band, where each of the variables in (3) need only be evaluated at the equator, and where the $v\partial_y T$ term is replaced by a suitable upstream differencing. In the JN ICM, this captures all the essential behavior of the CZ model while permitting a number of analytical results to be generated in special cases.

The simple atmospheric models that provide a zeroth-order approximation to the wind-stress response to SST anomalies can be written

$$\tau' = \mu A(T'; x, y), \tag{4}$$

where μ is the coupling coefficient and $A(T'; x, y)$ is a linear but nonlocal function of T' over the entire basin. For a Gill (1980) model with a specified meridional profile of the forcing appropriate to the assumed SST y-dependence, A is a simple integral operator.

Coupling is carried out by a version of flux correction: running the ocean model with observed climatological wind stress to define the ocean climatological state ($\bar{u}$, $\bar{w}$, $\bar{T}$, . . .), then defining SST anomalies, T', with respect to this. A known climatological solution to the coupled system is thus constructed. For sufficiently small coupling, this state is unique and stable; interannual variability must arise by bifurcations from this state as μ increases.

USEFUL LIMITS We introduce terminology for limits that are useful for understanding how coupled modes relate to simpler cases and for comparing various theoretical models. The *weak-coupling limit* is reached at small μ, i.e. little wind-stress feedback per unit SST anomaly; these modes are found not to be good prototypes for fully coupled modes. At large μ, one obtains the *strong-coupling limit*. When the time scale of dynamical adjustment of the ocean is small compared to the time scale of SST change by coupled processes (i. e. small δ), one has the *fast-wave limit*; which is very useful for generating analytical results that provide understanding of spatial structure and growth characteristics. The *fast-SST limit* is reached at large δ; this is the converse to the fast-wave limit, i.e. sea surface temperature adjusts quickly compared to ocean dynamical processes.

In the uncoupled case or in the fast-wave limit, the modes of the ICM, linearized about its climatology, separate into a set associated purely with the time derivatives of the shallow-water equations, referred to as *ocean-dynamics modes*, and a set associated purely with the time derivative of the SST equation, referred to as *SST modes*. In an uncoupled, zonally-bounded basin, the ocean-dynamics modes consist of a set of ocean-basin modes (Cane & Moore 1981) and a scattering spectrum (JN). At low frequencies and basin scales, the ocean-dynamics modes are very different from the Rossby and Kelvin modes of the infinite-basin case. In the coupled system, the distinction between corresponding coupled modes is maintained in the idealized fast-wave and fast-SST limits, but in most of the parameter space the coupled modes will have a mixed nature, for which we use the descriptive term *mixed SST/ocean-dynamics modes* when it is

necessary to be specific; otherwise the term *coupled modes* is taken to imply this.

WIND-DRIVEN OCEAN RESPONSE Extensive theory exists for the adjustment of the uncoupled shallow-water ocean to time-varying winds (see Moore & Philander 1978, Cane & Sarachik 1983, McCreary 1985 for reviews). Much of it is phrased in terms of adjustment to abrupt changes in wind; a much better prototype for understanding interannual coupled oscillations is the case of forcing by low-frequency, time-periodic winds (Cane & Sarachik 1981, Philander & Pacanowski 1981). Figure 6 shows a time-longitude plot of thermocline perturbations along the equator for such a case. The western Pacific leads the eastern Pacific by between 90 and 180

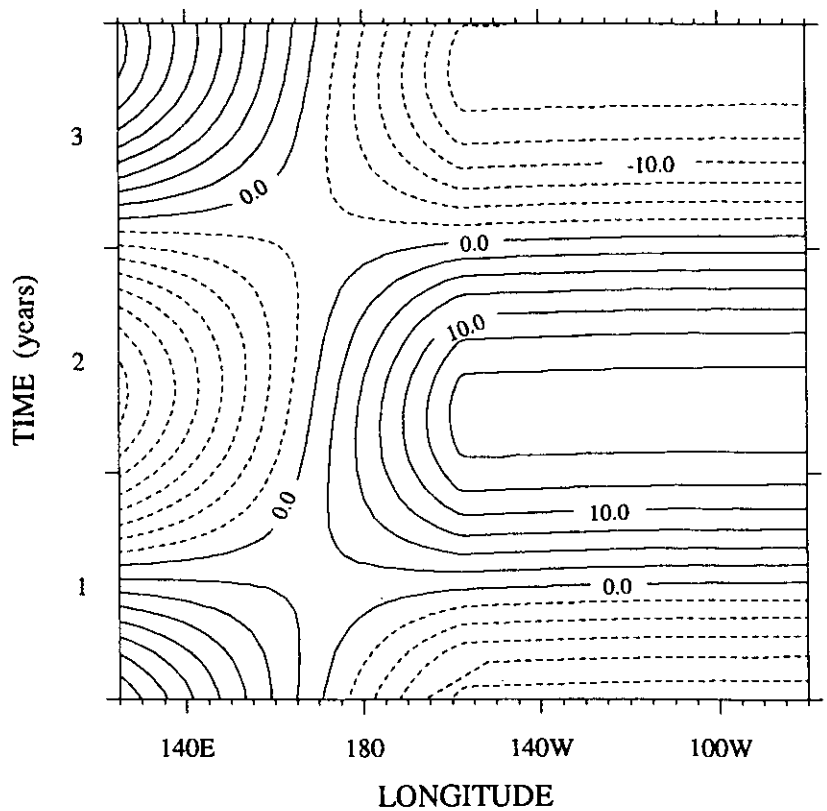

Figure 6 Time-longitude plot of thermocline depth anomalies along the equator from a shallow-water ocean model forced by specified wind stress: constant in longitude through the western half of the basin, zero in the eastern half, Gaussian in latitude (scale 5°), and periodic in time with period 3 years and amplitude 0.2 dyne/cm^2. Following Cane & Sarachik (1981) with specified modifications, and with frictional damping of time scale 0.5 yr in the ocean. Contour interval 2.5 m.

degrees in temporal phase. The fast-wave limit case, in which the ocean approaches equilibrium with the wind, would correspond to 180° phase difference between these, which would remove the apparent slow eastward "propagation." It should be emphasized that this is not a wave propagation in the sense of any individual free wave of the system, but rather the sum total of the ocean response which is not quite in equilibrium with the wind forcing. The slight departures from equilibrium, as measured by the difference from a 180° phase lag, characterize the oceanic memory which is so important to interannual variability.

SIMPLE MODELS: POINT COUPLING One special case where solutions of (1) can be carried forward is if the surface-layer feedbacks are dropped ($\delta_s = 0$) and if it is assumed that *coupling to the atmosphere occurs at a single point*, e.g. at the eastern boundary. The wind-stress magnitude is taken to be proportional to SST at that point and the spatial form of wind stress is fixed, for instance to be a patch of very small longitudinal extent (here placed at mid-basin for ease of presentation), with Gaussian y-dependence of curvature α. We give here an extended version of the MCZ model (or Schopf & Suarez 1990) using this approximation; the SST equation (3) and ocean shallow-water dynamics (1) can be reduced to

$$\delta^{-1}\partial_t T' + [(T' - T'_{\text{sub}}(h')] = 0 \tag{5a}$$

$$h'(t) = \sum_{j=1}^{\infty} a_j(\varepsilon_m)h'(t-4j) + \mu \sum_{j=0}^{\infty} b_j(\alpha, \varepsilon_m)T'(t-1/2-2j), \tag{5b}$$

where T' and h' are SST and thermocline depth anomalies at the eastern point, respectively, and the coefficients a_j, b_j summarize information about the ocean dynamics, boundary conditions, and parameters. The reduction of ocean dynamics to sums over discrete transit times results, of course, from the point-wise coupling assumptions. In contrast to (1), here time has been normalized by the time scale characterizing ocean dynamics (the Kelvin-wave basin-crossing time), so δ appears in the SST equation and the integer lag dependences on the past history of h' and T' are due to wave transit times across the basin with reflection at basin boundaries. This rescaling is because the MCZ model has been used primarily in the fast-SST limit ($\delta \to \infty$), which results in dropping the time derivative in (5a). In this case, (5) becomes an iterated map of high order for modes related to the time derivatives of the shallow-water equations, which yielded the lags.

A simpler delay equation which has proven influential in the field can be derived from the above by a series of simplifications which cannot be rigorously justified but which retain essential features of the dynamics:

(*i*) Set all $a_j = 0$ in (5b) while retaining the b_j, which amounts to removing eastern-boundary wave reflections while keeping those at the western boundary. This does irreparable damage to the uncoupled ocean dynamics, so the usefulness of this simplification depends on the coupling dominating the spatial structure of the mode—we show below how this comes about in an ICM. (*ii*) Move the wind stress to the point of coupling to SST (the position of the eastern boundary is now immaterial); this is reasonable when the coupled frequency is much less than the Kelvin transit time across the separation. (*iii*) Truncate the sum over b_j to only two terms—a single westward Rossby wave plus an eastward Kelvin wave. Because the series converges slowly, this can only be justified qualitatively. We present the model linearized about the climatology, since this determines the period and the location of the bifurcation:

$$\partial_t T' = (\mu b_0 - 1)T'(t) - \mu b_1 T'(t - 4\delta) \tag{6}$$

This is the *SSBH delayed-oscillator model.* Note that we have restored the time nondimensionalization used in (1–3). Nonlinear versions are straightforward to derive from (5) and differ significantly from that given by SSBH for more realistic $T_{sub}(h')$; $dT_{sub}/dh'|_0 = 1$ is used without loss of generality for this simple case. When the model is uncoupled ($\mu = 0$), the solution is a purely decaying mode whose eigenvalue is determined by the SST equation, i.e. an SST mode, in contrast to the MCZ model which also has uncoupled ocean modes. In the fast-wave limit ($\delta \to 0$), the model has stationary (i.e. nonoscillatory) SST modes which become unstable for coupling above $\mu = (b_0 - b_1)^{-1}$. For realistic values of δ, this unstable mode becomes oscillatory due to the adjustment time scales of subsurface ocean dynamics, here represented by a single delay. The SSBH model may thus be summarized as an SST-mode whose growth can be understood from the fast-wave limit, perturbed to give oscillation by aspects of ocean dynamics which are *not* characteristic of the uncoupled case. We will show below that this interpretation can be carried over to an ICM.

On the other hand, consider the modes of the extended MCZ model (Equation 5), linearized about climatology, with time dependence $\exp(\sigma t)$. The infinite series in (5b) can be summed exactly (Cane & Sarachik 1981) under certain conditions (note the contrast to the severe truncation of the SSBH model which has sometimes been interpreted too strongly in terms of individual waves). Equation (5b) becomes, in the simplest case:

$$[\sinh(2\sigma)/\sinh(\sigma)]h' = \mu T' \tag{5b'}$$

In the fast-SST limit, there is a singularity at $\mu = 2$, with two equal eigenvalues, demarcating the boundary between oscillatory eigenvalues below and stationary eigenvalues above, one of which is strongly growing.

In this case, the singularity leads to a codimension 2 (double-zero) bifurcation. When any other destabilizing process is added, the bifurcation is oscillatory (Hopf); with damping and no other destabilizing process it is stationary (transcritical)—but note that stationary bifurcations must be treated with caution since they are not robust to relaxation of assumptions used to construct the climatological state.) The oscillatory case is the one that applies to ENSO, but it is worth asking why the ocean dynamics "break" from oscillatory behavior, as would be expected of wave-related modes in a bounded basin, into a growing stationary mode. Consider the case where coupled feedback processes are very strong; then local interactions dominate nonlocal wave-propagation processes yielding pure growth—the mode grows too fast to be affected by weak return signals from the western boundary. The transition has to occur at moderate coupling. The remarkable feature which will be shown in an ICM below is that the stationary mode, even in the fast-SST limit, shares more characteristics with the SST mode in the fast-wave limit than with the uncoupled ocean modes. In fact, at strong coupling, the stationary mode eigensurface is continuously connected across the whole range of δ.

SIMPLE MODELS: FAST-WAVE LIMIT Although the time scale of subsurface dynamics is the dominant factor in setting the period of ENSO, the strong simplifications that occur in the fast-wave limit permit insight into spatial structure. Setting $\delta = 0$ in (1), i.e. assuming that oceanic adjustment occurs fast compared to other time scales, and considering that the damping ε_m is very weak, reduces the shallow-water equations to Sverdrup balance along the equator:

$$\partial_x h' = \tau' \tag{7}$$

with negligible vertical mean currents. The off-equatorial ocean solution plays a significant role which can be summarized in boundary conditions to (7) suitably derived as the limit to wave adjustment processes, as discussed in JN and in Hao et al (1993), both of which provide further analysis of this fast-wave limit case. The multiple coupled feedback mechanisms can be seen from a linearized version of the SST equation (3), with h' given by combining Equations (7) and (4) (see Neelin 1991).

A number of physical mechanisms contribute to destabilization of SST modes. However, these mechanisms tend to compete in terms of whether the mode will be purely growing or will propagate slowly along the equator. For instance, a warm SST anomaly will lead to westerly wind anomalies above and to the west of the warm SST, which will lead to eastward current anomalies and reduced upwelling and thus to a warming of SST which will both enhance the original anomaly and cause it to shift slightly west-

ward. In the ICM, these feedbacks are controlled by δ_s. On the other hand, the thermocline slope will tend to be reduced below and slightly to the east of the SST anomaly. The subsurface waters being carried to the surface will be warmer than normal, thus tending to enhance the initial anomaly. Since both the thermocline response and wind-stress response are nonlocal, the shape of the anomalies will evolve to satisfy basin boundary conditions, leading for a broad range of parameters to a stationary growing mode. Analytical results for both propagating and stationary cases can be obtained in the fast-wave limit (JN); Hao et al 1993 give nonlinear solutions. The mode with the largest spatial scale in the basin is always the most unstable, with SST and wind structure similar to observations. The larger SST anomalies in the east and central basin are produced partly by the shape of the climatological upwelling, and partly by purely dynamical effects, with east-west asymmetry introduced by the latitudinal derivative of the Coriolis force. The analytical results also indicate the role of the eastern boundary in keeping the mode from propagating; the point-coupling models emphasize the role of the western boundary on the ocean—but for spatial structure, eastern boundary effects enter mainly through the atmosphere.

The feedback loop described above sounds very similar to that described in the Bjerknes hypothesis. It gives the mechanism maintaining interannual variability and, suitably extended by the analytical results, the spatial form. However, it only gives the interannual period in regimes with coherent zonal propagation along the equator. This is a good prototype for the slowly-propagating modes in a number of coupled models (e.g. Meehl 1990b, Lau et al 1992), but to understand how this mode relates to the observed system, it is essential to see how time scales of subsurface ocean dynamics perturb it in the vicinity of the stationary regime to produce oscillations with standing-oscillatory SST anomalies.

PARAMETER DEPENDENCE OF LEADING MODES IN AN ICM A global picture of the connection of coupled modes in the ICM (1)–(3) can be delineated by tracing the behavior of the few leading (fastest-growing or slowest-decaying) eigenmodes as a function of parameters μ and δ, beginning with $\delta_s = 0$ for simplicity. In the fast-wave limit ($\delta = 0$), a stationary (i.e. purely growing) SST mode becomes unstable. Its spatial structure is suggestive: It looks like the warm phase of Figure 4, except that the thermocline component has eastern and western parts of the basin exactly out of phase, so there is no oscillation. As one moves from the fast-wave limit to realistic relative-time-scale ratios (larger δ) one finds that this stationary eigenmode is scarcely changed. In fact, for coupling values stronger than a certain threshold (where coupled processes dominate those associated with oceanic

wave propagation, as discussed above), the eigensurface extends without substantial change from the fast-wave limit all the way to the fast-SST limit. This is pivotal in understanding the coupled system because 1. it allows the spatial form and growth mechanisms of important coupled regimes to be understood from the fast-wave limit; and 2. it implies that modes associated with ocean dynamics must connect somehow to this strongly-growing mode.

To illustrate how this happens, Figure 7 shows a typical slice through parameter space as a function of coupling, for a realistic value of δ. The eigenvalues of the five leading modes are plotted as dots on the complex plane (growth-rate, frequency), for evenly spaced coupling values in the range $\mu = 0$ to 0.8. Left-right symmetry occurs because oscillatory modes always exist as conjugate pairs. The strongly growing stationary (i.e. non-oscillatory) branch in the strong-coupling range is indicated as "stationary regime" on the figure, since it is the only unstable mode in this parameter range. This is the mode that is so closely related to the SST mode in the fast-wave limit. At a slightly lower coupling value a singularity occurs where this is converted into an oscillatory mode—this singularity (corresponding to a codimension-2 double-zero bifurcation) extends as a curve in the μ-δ parameter plane connecting the eigensurface associated with the gravest SST mode to surfaces that are associated with ocean dynamics modes at low coupling. To the lower-coupling side of this singularity one finds the regime with oscillations that have a standing SST component (denoted in the figure as "standing-SST oscillatory regime'; SSO regime), corresponding to that shown in Figure 4 for the CZ ICM. The spatial form is similar to the stationary SST mode, and the mode is destabilized by the same coupling mechanisms, but subsurface oceanic dynamics provide the memory for the oscillation, characterized by temporal phase lag of the thermocline across the basin as in observations (Figure 3). This regime extends across a large range of δ, from $\delta = O(1)$ to the fast-SST limit.

In contrast, the connection of this standing-SST oscillation regime to the uncoupled case is complicated. In Figure 7, the SSO regime eigensurface eventually connects to one of the modes from the discretized scattering spectrum, but as it does so the mode rapidly changes in spatial form. When one includes variations in δ, one finds that the standing-oscillation regime connects, not to a single mode from the uncoupled oceanic dynamics spectrum, but to a series of them: The low coupling end of the branch attaches first to the lowest-frequency scattering mode (as in Figure 7), then to sequentially higher-frequency scattering modes, and finally at large δ, near the fast-SST limit, it connects to the gravest ocean basin mode, much as in the MCZ point-coupling model. These successive connections are

Fig. 7

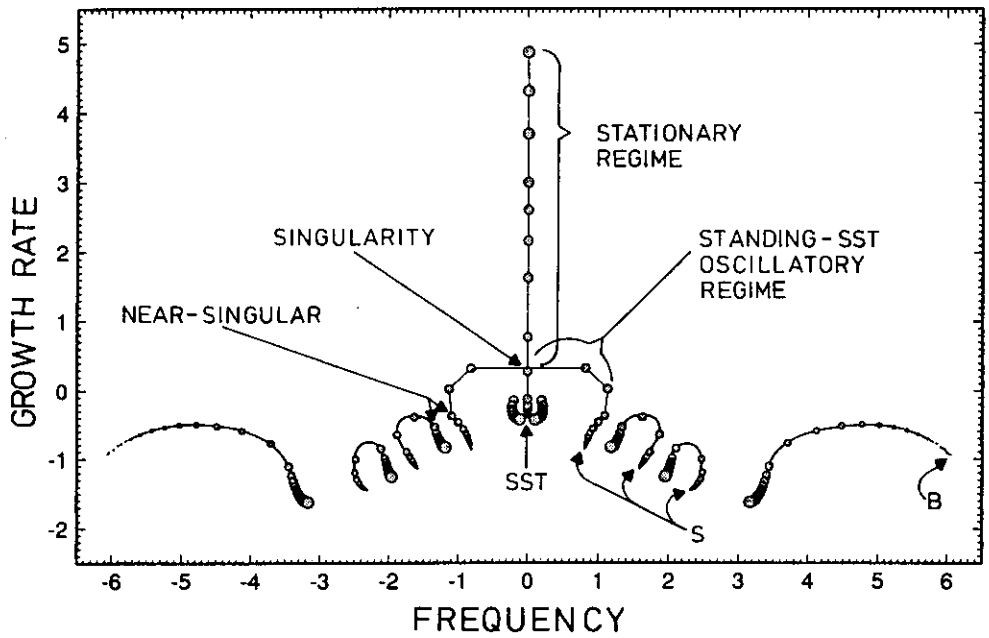

Figure 7 Eigenvalues of the five leading modes of the Jin & Neelin (1993a) intermediate coupled model as a function of coupling coefficient, μ, for a realistic value of the relative time scale coefficient, $\delta = 1.5$. Dots give frequency and growth rate of each mode on the complex plane, with dot size representing coupling for constant increments from $\mu = 0$ to $\mu = 0.8$. Eigenvalues trace out continuous paths as a function of coupling (indicated by interpolated lines for clarity). Uncoupled modes (ocean basin mode B, discretized scattering modes S, and an SST mode) are indicated at $\mu = 0$ (smallest dots). The modes have mixed character for larger μ: The purely growing mode which produces the *stationary regime*, indicated over the range of large μ, is closely related to the stationary SST mode; this is connected at a singularity to the important *standing-SST oscillatory regime* which extends over a range of moderate coupling values.

accomplished by a sequence of additional singularities; a "near-singular" point is shown, where the SSO regime connects to the next scattering mode at larger δ. However as δ varies, the characteristics of the SSO regime are almost completely insensitive to which uncoupled ocean mode it is attached to; its properties are fundamentally deterined by the coupling and it is thus best approached conceptually from the strong-coupling side.

It is thus much simpler to view the standing-oscillation regime as an extension of the strongly-growing stationary mode towards lower coupling, where ocean dynamics begin to regain some aspects of wavelike behavior. In this interpretation, one begins by understanding the spatial form and instability mechanisms of the mode in the fast-wave limit at fairly strong coupling. As one follows the stationary mode out to realistic values of the relative time-scale parameter and down to moderate coupling, it retains its form but acquires a frequency associated with "picking up"

a degree of freedom from among the low-frequency part of the scattering spectrum on the low-coupling side. This view is consistent, in terms of physical content, with the original interpretation of the SSBH delayed oscillator model (Equation 6) (as long as it is understood that the subsurface memory is not associated with individual waves). Furthermore, the smooth connection from the fast-wave limit to the fast-SST limit implies that the seemingly contradictory approaches to the problem represented by (6) and (5b′) are just alternative approximations to the same eigensurface.

Finally, to make the connection to propagating regimes such as occur in some of the models, which may be relevant to the differences in evolution of certain ENSO events, consider reintroducing a third parameter, such as δ_s. As this changes, it is easy to move smoothly and gradually from the standing-oscillation regime to a regime of the mixed SST/ocean-dynamics modes where propagation occurs during parts of the cycle and contributes to the period (JN, Kleeman 1993). The standing-oscillation regime provides the clearest case emphasizing the role of subsurface dynamics in determining periodicity; the fast-wave-limit propagating cases provide alternate simple cases in which periodicity is provided by zonal phase lags. Between these continuously connected regimes, both characteristics can coexist within the same coupled mode. There is thus no contradiction between evidence for importance of subsurface dynamics in the ENSO cycle and indications of other contributing mechanisms.

TRANSITIONS TO IRREGULARITY The modeling consensus is thus that ENSO dynamics are fundamentally oscillatory. In particular, for models whose uncoupled components have no internal variability, interannual variability arises as a forward Hopf bifurcation of the coupled system, yielding a limit cycle. The obvious question is then the source of irregularity in the observed cycle: (*a*) transition to chaotic behavior by higher bifurcations associated with the coupled dynamics, and/or (*b*) stochastic forcing by atmospheric "noise" from shorter-lived phenomena which do not depend on coupling?

With regard to internal dynamics, CZ pointed out early on that their model achieved a degree of irregularity through deterministic coupled dynamics alone. Disagreement by Battisti & Hirst (1989) over whether this was due to the CZ numerical implementation seems to have been settled in the larger picture in favor of the original finding; for instance, the smoothly posed, simpler version of JN also possesses irregular regimes. Explicit discussion of the bifurcation structure of the coupled system and secondary bifurcations to regimes of complex behavior was given in an HCM in Neelin (1990), but the first clear demonstration of a bifurcation

sequence into chaotic behavior was given by MCZ in the point-coupling model (5). An unfortunate footnote must be added for Vallis (1986), who attempted to raise these questions in an ad hoc model (now thought to lack essential physics) and instead illustrated the dangers of spurious chaos due to highly-truncated numerics (Vallis 1988). As to the scenario for the transition to chaos, MCZ cite the Ruelle-Takens-Newhouse scenario (e.g. Eckmann 1981) as a possibility, based upon their observing irregular behavior subsequent to one period doubling. However, it is clear that the presence of parametric forcing by the annual cycle plays an important role in the prevalence of chaotic regimes in parameter space (Zebiak & Cane 1987, MCZ) and in the widespread frequency-locked regimes (CZ, Battisti & Hirst 1989, Schopf & Suarez 1990, Barnett et al 1993). A "Devil's staircase" scenario (e.g. Jensen et al 1984) is among current postulates (F.-F. Jin et al, personal communication; E. Tziperman et al, personal communication).

On the stochastic forcing side, early discussions of ENSO were often phrased in terms of random wind events initiating an El Niño warm phase. Among modelers this has given way to the view that stochastic forcing more likely disrupts the cycle (or possibly excites a weakly-decaying oscillatory mode, if below the Hopf bifurcation). Zebiak (1989) indicates that such effects have only a minor impact in the CZ ICM; Latif & Villwock (1990) and T. P. Barnett et al (personal communication) indicate that the effects of randomized atmospheric forcing can be considerable on an uncoupled tropical ocean model. Problems in quantifying the importance of stochastic effects involve estimation of spatial coherence, which is extremely important to ocean response and to separation of the stochastic component from the atmospheric deterministic response to SST.

Prediction and Predictability

The underlying periodic aspects of ENSO and the above theoretical considerations imply a good deal of ENSO predictability. A hierarchy of ENSO prediction schemes has been developed which includes statistical and physical models (Inoue & O'Brien 1984, Cane et al 1986, Graham et al 1987a,b, Xu & von Storch 1990, Goswami & Shukla 1991, Keppene & Ghil 1992, Barnston & Ropelewski 1992, Latif et al 1993b, Penland & Magorian 1993). A more complete list of references can be found in the review papers by Barnett et al (1988) and Latif et al (1993c). The most succesful schemes, the coupled ocean-atmosphere models, show significant skill in predicting ENSO even at lead times beyond one year. Figure 8 shows the anomaly correlation of the observed with the predicted SST anomalies averaged over the region of greatest variability for the CZ ICM—the first coupled model used for ENSO forecasts. Comparable

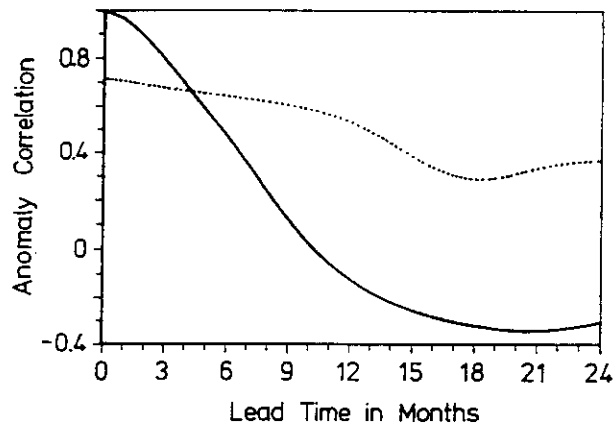

Figure 8 Skill scores of prediction ensembles as a function of lead time for forecasts by the Cane & Zebiak (1985) intermediate coupled model (*dotted curve*), compared with skill obtained by assuming persistence of anomalies (*solid curve*). The measure is correlation of predicted and observed SST averaged over the region of largest ENSO anomalies ($\pm 5°$ latitude, 150°W to 90°W longitude), during the period 1972 to 1991. Note that 0-month lead can differ from observed because SST data are not used in the initialization. Data from S. Zebiak (personal communication); for methodology see Cane et al (1986).

results have recently been obtained with CGCMs (Latif et al 1993b) and HCMs (Barnett et al 1993).

At lead times of a few months, the coupled models do not beat the persistence forecast which assumes that the SST anomalies remain constant throughout the forecast period. This is due to the fact that up to present no ocean observations are used in the initialization of the coupled models. Instead, the observed wind stresses are used to spin up to the ocean component, but errors in the forcing and the model formulation manifest themselves as considerable errors in the initial SST anomaly fields. Thus significant improvement of the forecasts at small lead times can be achieved by assimilating in situ ocean obervations (e.g. Leetmaa & Ji 1989) which are becoming increasingly available (e.g. Hayes et al 1991), and/or observations from space (e.g. Tai et al 1989). In the case of coupled GCMs, a further reduction of climate drift will greatly aid this process. Upper limits on predictability are an area of current investigation (Blumenthal 1991, Goswami & Shukla 1991, Keppenne & Ghil 1992).

THE EXTRATROPICAL PROBLEM

Already in the late 1950s and early 1960s possible large-scale air-sea interactions in midlatitudes over both the Pacific and Atlantic Oceans were described by several authors (e.g. Namias 1959, Bjerknes 1964). Theoretical work by Hasselmann (1976) showed that the ocean can convert

the white noise forcing by the atmosphere into a red noise SST spectrum through its large heat capacity. Such low-frequency SST anomalies can potentially feed back onto the atmospheric circulation. Recent modeling results suggest that the midlatitudinal atmosphere may indeed be significantly influenced by midlatitudinal SST anomalies, especially on interdecadal time scales (e.g. Hense et al 1990). The response characteristics, however, appear to be much more complex than in the tropics. Since the understanding of the extratropical problem is still at a rather low level, we restrict ourselves to pointing out four of the most important differences from the tropical problem.

First, the midlatitudinal circulation is influenced not only by midlatitudinal but also by tropical SST anomalies, as shown in many observational and modeling studies (e.g. Shukla & Wallace 1983, Lau 1985). A characteristic response pattern, the Pacific/North-America pattern, describing the response of the atmospheric winter circulation to tropical Pacific SST anomalies associated with the extremes in the ENSO cycle, has been identified (Wallace & Gutzler 1981) and exploited for short-range climate predictions for the North Pacific/North American region (Barnett & Preisendorfer 1987).

Second, both atmosphere and ocean have a much higher level of uncoupled internal variability. Uncoupled ocean models can produce decadal- or centennial-scale variations (e.g. Weaver et al 1991, Mikolajewicz & Maier-Reimer 1990). The effect of slowly-varying ocean boundary conditions on the atmosphere can be overwhelmed by the atmospheric noise level; for instance, Lau (1985), comparing AGCM runs with observed and climatological SST, found that observed SST variations produced a significant increase in atmospheric variability only in the tropics, while the midlatitudinal atmosphere exhibits a realistic level of interannual variability even in the case with climatological SST (Lau 1981b). Both effects make it difficult to assess the role of coupling on observed interannual to interdecadal variability (e.g. Gordon et al 1992). For instance, Delworth et al (1993) provide an analysis in a coupled GCM integration of Atlantic interdecadal variability involving changes in the overturning thermohaline circulation and advection-induced changes in density. While these phenomena have signatures in SST and air temperature, they are hypothesized to be uncoupled oceanic phenomena, driven by stochastic forcing from the atmosphere.

Third, the response of the general circulation in midlatitudes to SST anomalies (tropical and extratropical) is highly nonlinear (Kushnir & Lau 1992), while the response of the tropical atmosphere can be approximated by linear dynamics (e.g. Gill 1980). Experiments with general circulation models provide an opportunity to further investigate the relationship

between extratropical SST anomalies and atmospheric flow regimes. Palmer & Sun (1985) investigated the reponse of the atmosphere to SST anomalies in the northwestern Atlantic. They showed that the model response was consistent with data and concluded that a positive feedback between ocean and atmosphere is possible during certain times of the year which might contribute to persistent climate anomalies. Some evidence of impacts of extratropical SST anomalies on the general circulation is also provided by Lau & Nath (1990) and Kushnir & Lau (1992) but the relationships between midlatitudinal SSTs and atmospheric indices appear to be far more complicated than in the tropics, in part due to the importance of transient disturbances to the time-averaged response.

Finally, direct effects of local air-sea heat exchange on the ocean play a more active role at midlatitudes than in the tropics where SST anomalies result primarily from variations in the surface wind stress. Persistent large-scale midlatitudinal SST fluctuations can be identified in Atlantic, Pacific, and global time series (Wallace & Jiang 1987, Wallace et al 1990, Folland et al 1991, Ghil & Vautard 1991). These anomalies may be driven by anomalies in the surface heat flux (e.g. Alexander 1992a, Cayan 1992), at least on monthly-to-interannual time scales. Kushnir (1993) argues that ocean circulation is important on longer time scales. Part of the interannual variability of SST in the North Pacific is linked to the ENSO phenomenon (Weare et al 1976, Luksch et al 1990, Alexander 1992a) and results from changes in the atmospheric circulation over the North Pacific in response to tropical SST anomalies. During an El Niño (warm) phase, for instance, an anomalous low-pressure system develops over the North Pacific, thereby strengthening the Aleutian Low. The changes in surface wind stress and more importantly those in surface heat flux force negative SST anomalies in the central North Pacific; the reverse occurs during an ENSO cold phase. The temperature near the American west coast tends to vary in phase with the tropical anomaly and is probably related in part to coastal Kelvin waves, which are generated by the reflection of equatorial Kelvin wave packets. Anomalous warm air advection in response to the strengthening of the Aleutian Low also plays a significant role in the generation of these anomalies. Pitcher et al (1988) show that these North Pacific SST anomalies can contribute a considerable atmospheric response; on the other hand, Alexander (1992b) finds that the local ocean-atmosphere feedback tends to act as a damping on the North Pacific SST response to ENSO.

SUMMARY AND DISCUSSION

The past decade has seen our knowledge of ocean-atmosphere interaction for the tropical problem go from the level of hypothesis to that of a field

with rapidly developing theoretical and numerical modeling components. Theory for the El Niño/Southern Oscillation phenomenon has reached a relatively mature level for understanding the mechanisms contributing to the maintenance and period of the cycle, as they relate to the primary bifurcation from the climate state in models of different levels of complexity. The relationship between several regimes of interannual variability found in models has been largely understood, as has the complementary relationship between simple prototypes for the modes of coupled variability. These illustrate both the importance of subsurface ocean dynamics in providing the memory of the system, and the fundamental impact of coupling in determining the spatial character of these modes. The exact mechanism of the two apparent time scales in the ENSO signal and the dominant sources of irregularity in the cycle are not yet understood, although hypotheses have been posed in terms of the higher bifurcations of the coupled system or stochastic forcing due to uncoupled variability.

Models that capture the primary bifurcation in a realistic regime have been used to skillfully predict ENSO-related tropical Pacific SST anomalies at lead times out to a year. The potential for predictability beyond this is not yet known; a major area of current endeavor is ascertaining to what degree such tropical predictability can translate into useful midlatitude climate predictions on seasonal-to-interannual time scales.

Simulation of tropical climate and ENSO-related variability with coupled GCMs is improving at a rapid rate. The climate drift and variety of regimes of variability in earlier versions of these models are characteristic of the sensitivity of the coupled system and provide an apt demonstration that a coupled model is more complex than the sum of its uncoupled components. Because three-dimensional feedbacks tended to exacerbate relatively small errors in physical parameterizations in some of the early versions, small improvements in these parameterizations have in several cases provided highly encouraging improvements in simulation. This rapid learning curve for the tropical problem is partly the result of not needing to explicitly simulate the global thermohaline circulation which maintains the deep-ocean temperature and salinity through high-latitude convective sinking. Coupled GCMs for phenomena involving this circulation may have a longer development time to achieve accurate simulation without flux correction.

Exciting new areas within the tropical problem include: ocean-atmosphere interactions within the Atlantic and Indian basins, multi-basin interactions, and possible interactions with neighboring land processes (e.g. Southeast Asian and Indian Monsoon circulations, Tibetan plateau snow cover, Sahel rainfall, and South American convergence zones). Mon-

soon-ENSO interactions have already received considerable speculation (e.g. Yasunari & Seki 1992, Webster & Yang 1992); given the complexity of coupled processes in the tropical Pacific basin alone, unraveling next-order linkages to other subsystems will be a true challenge to models at all levels in the hierarchy. Circumstantial evidence from the coupled GCMs suggests the importance of coupled interactions in maintaining major features of the tropical climate and seasonal cycle, for instance, the warm-pool/cold-tongue configuration in the Pacific, and that the mechanisms involved may be qualitatively similar to those active in interannual variability. Developing a theoretical understanding of how these apply to the climatology would be a valuable asset both from a conceptual point of view, and for distinguishing the plausible from the speculative in tropical aspects of global-change scenarios.

While the midlatitude coupled problem is complicated by large internal variability of both atmosphere and ocean, there is reason to hope that the enthusiasm and experience that have accumulated for coupled interactions in the tropics will be carried to higher latitudes. There is growing attention to internal climate variability at decadal and longer time scales both in the tropics and extratropics, due to its importance in the problem of detection of anthropogenic warming and as a new frontier in simulation and theory. This will no doubt lead to a plethora of hypothesized mechanisms which may take decades to refute or verify due to the lack of long observational time series of dynamically-important quantities. Nonetheless, we can look forward to the need for a review of coupled ocean-atmosphere dynamics for the extratropical problem and new aspects of the tropical problem within a relatively few years.

ACKNOWLEDGMENTS

Support for this study has been provided by National Science Foundation ATM-9215090, Presidential Young Investigator award ATM-9158294, National Oceanographic and Atmospheric Administration NA16RC0178/26GP00114-01, CEC Environmental Programme EV5V-CT-0121, the Max-Planck-Institut für Meteorologie, and the Max-Planck Society (partial support during a sabbatical leave by JDN at MPIM). We thank M. Grunert and W. Weibel for assistance with graphics, and many colleagues for constructive comments.

Literature Cited

Alexander, M. A. 1992a. Midlatitude atmosphere-ocean interaction during El Niño. Part I: the North Pacific. *J. Climate* 5: 944–58

Alexander, M. A. 1992b. Midlatitude atmosphere-ocean interaction during El Niño. Part II: the Northern hemisphere atmosphere. *J. Climate* 5: 959–72

Allen, M. R., Davey, M. K. 1993. Empirical parameterization of tropical ocean-atmosphere coupling: the "inverse Gill problem." *J. Climate* 6: 509–30

Anderson, D. L. T., McCreary, J. P. 1985. Slowly propagating disturbances in a coupled ocean-atmosphere model. *J. Atmos. Sci.* 42: 615–29

Barnett, T. P. 1983. Interaction of the monsoon and Pacific Trade Wind system at interannual time scales. Part I: the equatorial zone. *Mon. Weather Rev.* 111: 756–73

Barnett, T. P. 1991. The interaction of multiple time scales in the tropical climate system. *J. Climate* 4: 269–85

Barnett, T. P., Graham, N., Cane, M., Zebiak, S., Dolan, S., O'Brien, J., Legler, D. 1988. On the prediction of El Niño of 1986–1987. *Science* 241: 192–96

Barnett, T. P., Latif, M., Graham, N., Flügel, M., Pazan, S., White, W. 1993. ENSO and ENSO-related predictability. Part I: prediction of equatorial Pacific sea surface temperature with a hybrid coupled ocean-atmosphere model. *J. Climate* 6: 1545–66

Barnett, T. P., Latif, M., Kirk, E., Roeckner, E. 1991. On ENSO physics. *J. Climate* 4: 487–515

Barnett, T. P., Preisendorfer, R. 1987. Origins and levels of monthly forecast skill for United States surface air temperatures determined by canonical correlation analysis. *Mon. Weather Rev.* 115: 1825–50

Barnston, A. G., Ropelewski, C. F. 1992. Prediction of ENSO episodes using canonical correlation analysis. *J. Climate* 5: 1316–45

Battisti, D. S. 1988. The dynamics and thermodynamics of a warming event in a coupled tropical atmosphere/ocean model. *J. Atmos. Sci.* 45: 2889–919

Battisti, D. S. 1989. On the role of off-equatorial oceanic Rossby waves during ENSO. *J. Phys. Oceanogr.* 19: 551–59

Battisti, D. S., Hirst, A. C. 1989. Interannual variability in the tropical atmosphere/ocean system: influence of the basic state, ocean geometry and nonlinearity. *J. Atmos. Sci.* 46: 1687–712

Berlage, H. P. 1957. Fluctuations in the general atmospheric circulation of more than one year, their nature and prognostic value. *K. Ned. Meteor. Inst. Meded. Verh.* 69: 152 pp.

Bjerknes, J. 1964. Atlantic air-sea interaction. *Adv. Geophys.* 10: 1–82

Bjerknes, J. 1969. Atmospheric teleconnections from the equatorial Pacific. *Mon. Weather Rev.* 97: 163–72

Blumenthal, M. B. 1991. Predictability of a coupled ocean-atmosphere model, *J. Climate* 4: 766–84

Bretherton, F. P. 1982. Ocean climate modeling. *Prog. Oceanogr.* 11: 93–129

Bryan, K., Manabe, S., Pacanowski, R. C. 1975. A global ocean-atmosphere climate model. Part II: the ocean circulation. *J. Phys. Oceanogr.* 5: 30–46

Bryan, K., Manabe, S., Spelman, M. J. 1988. Interhemispheric asymmetry in the transient response of a coupled ocean-atmosphere model to a CO_2 forcing. *J. Phys. Oceanogr.* 18: 851–67

Cane, M. A. 1979. The response of an equatorial ocean to simple wind stress patterns: I. Model formulation and analytic results. *J. Mar. Res.* 37: 233–52

Cane, M. A. 1986. El Niño. *Annu. Rev. Earth Planet. Sci.* 14: 43–70

Cane, M. A., Moore, D. W. 1981. A note on low-frequency equatorial basin modes. *J. Phys. Oceanogr.* 11: 1578–84

Cane, M. A., Münnich, M., Zebiak, S. E. 1990. A study of self-excited oscillations of the tropical ocean-atmosphere system. Part I: linear analysis. *J. Atmos. Sci.* 47: 1562–77

Cane, M. A., Sarachik, E. S. 1977. Forced baroclinic ocean motions: II. The linear equatorial bounded case. *J. Mar. Res.* 35: 395–432

Cane, M. A., Sarachik, E. S. 1981. The response of a linear baroclinic equatorial ocean to periodic forcing. *J. Mar. Res.* 39: 651–93

Cane, M. A., Sarachik, E. S. 1983. Equatorial oceanography. *Rev. Geophys. Space Phys.* 21: 1137–48

Cane, M. A., Zebiak, S. E. 1985. A theory for El Niño and the Southern Oscillation. *Science* 228: 1084–87

Cane, M. A., Zebiak, S. E., Dolan, S. C. 1986. Experimental forecasts of El Niño. *Nature* 321: 827–32

Cayan, D. R. 1992. Latent and sensible heat flux anomalies over the northern oceans: driving the sea surface temperature. *J. Phys. Oceanogr.* 22: 859–81

Chao, Y., Philander, S. G. H. 1993. On the structure of the Southern Oscillation. *J. Climate* 6: 450–69

Charnock, H., Philander, S. G. H., eds. 1989. The dynamics of the coupled atmosphere and ocean. *Proc. of a Royal Society Discussion Meeting*. London: R. Soc. 315 pp.

Cubasch, U., Hasselmann, K., Höck, H., Maier-Reimer, E., Mikolajewicz, U., et al. 1992. Time-dependent greenhouse warming computations with a coupled ocean-atmosphere model. *Climate Dyn.* 8: 55–69

Delworth, T. L., Manabe, S., Stouffer, R. J. 1993. Interdecadal variations of the ther-

mohaline circulation in a coupled ocean-atmosphere model. *J. Climate* In press
Deser C., Wallace J. M. 1990. Large-scale atmospheric circulation features of warm and cold episodes in the tropical Pacific. *J. Climate* 3: 1254–81
Dickinson, R. E. 1983. Land surface processes and climate-surface albedos and energy balance. *Adv. Geophys.* 25: 305–53
Eckmann, J. P. 1981. Roads to turbulence in dissipative dynamical systems. *Rev. Mod. Phys.* 53: 643–53
Endoh, M., Tokioka, T., Nagai, T. 1991. Tropical Pacific sea surface temperature variations in a coupled atmosphere-ocean general circulation model. *J. Mar. Syst.* 1: 293–98
Folland, C., Owen, J., Ward, M. N., Colman, A. 1991. Prediction of seasonal rainfall in the Sahel region using empirical and dynamical methods. *J. Forecasting* 10: 21–56
Gates, W. L., Han, Y. J., Schlesinger, M. E. 1985. The global climate simulated by a coupled atmosphere-ocean general circulation model: preliminary results. See Nihoul 1985, 40: 131–51
Gates, W. L., Mitchell, J. F. B., Boer, G. J., Cubasch, U., Meleshko, V. P. 1992. Climate modeling, climate prediction and model validation. In *Climate Change* 1992: *The supplementary report to the Intergovernmental Panel on Climate Change Scientific Assessment*, ed. J. T. Houghton, B.A. Callander, S.K. Varney, pp. 97–133. Cambridge: Univ. Cambridge Press
Gent, P. R., Cane, M. A. 1989. A reduced gravity, primitive equation model of the upper equatorial ocean. *J. Comput. Phys.* 81: 444–80
Gent, P. R., Tribbia, J. J. 1993. Simulation and predictability in a coupled TOGA model. *J. Climate* In press
Ghil, M., Kimoto, M., Neelin, J. D. 1991. Nonlinear dynamics and predictability in the atmospheric sciences. *Rev. Geophys.*, Suppl., pp. 46–55, U.S. Natl. Rep. to the Int. Union of Geodesy and Geophys. 1987–1990
Ghil, M., Vautard, R. 1991. Interdecadal oscillations and the warming trend in global temperature time series. *Nature* 350: 324–27
Gill, A. E., 1980. Some simple solutions for heat induced tropical circulation. *Q. J. R. Meteorol. Soc.* 106: 447–62
Gill, A. E., 1985. Elements of coupled ocean-atmosphere models for the tropics. See Nihoul 1985, 40: 303–28
Gill, A. E., Clarke, A. J. 1974. Wind-induced upwelling, coastal current, and sea-level changes. *Deep-Sea Res.* 21: 325–45
Gill, A. E., Rasmusson, E. M. 1983. The 1982–1983 climate anomaly in the equatorial Pacific. *Nature* 306: 229–34
Gordon, C. 1989. Tropical ocean-atmosphere interactions in a coupled model. *Phil. Trans. R. Soc. London Ser. A* 329: 207–23
Gordon, A. L., Zebiak, S. E., Bryan, K. 1992. Climate variability and the Atlantic Ocean. *EOS, Trans. Am. Geophys. Union* 73(15): 161
Goswami, B. N., Shukla, J. 1991. Predictability of a coupled ocean-atmosphere model. *J. Climate* 4: 3–22
Graham, N. E., Michaelsen, J., Barnett, T. P. 1987a. An investigation of the El Niño-Southern Oscillation cycle with statistical models. 1. Predictor field characteristics. *J. Geophys. Res.* 92: 14,251–70
Graham, N. E., Michaelsen, J., Barnett, T. P. 1987b. An investigation of the El Niño-Southern Oscillation cycle with statistical models. 2. Model results. *J. Geophys. Res.* 92: 14,271–89
Graham, N. E., White, W. B. 1988. The El Niño cycle: Pacific ocean-atmosphere system. *Science* 240: 1293–302
Graham, N. E., White, W. B. 1990. The role of the western boundary in the ENSO cycle: experiments with coupled models. *J. Phys. Oceanogr.* 20: 1935–48
Hao, Z., Neelin, J. D., Jin, F.-F. 1993. Nonlinear tropical air-sea interaction in the fast-wave limit. *J. Climate* 6: 1523–44
Hasselmann, K. 1976. Stochastic climate models. Part I: theory. *Tellus* 28: 289–305
Hasselmann, K. 1988. PIPs and POPs: the reduction of complex dynamical systems using Principal Interaction and Principal Oscillation Patterns. *J. Geophys. Res.* 93D: 11,015–21
Hayes, S. P., Mangum, L. J., Picaut, L. J., Sumi, A., Takeuchi, K. 1991. TOGA-TAO: a moored array for real-time measurements in the tropical Pacific ocean. *Bull. Am. Meteorol. Sci.* 72: 339
Hense, A., Glowienka-Hense, R., von Storch, H., Stähler, U. 1990. Northern Hemisphere atmospheric response to changes of Atlantic Ocean SST on decadal time scales: a GCM experiment. *Climate Dyn.* 4: 157–74
Hirst, A. C. 1986. Unstable and damped equatorial modes in simple coupled ocean-atmosphere models. *J. Atmos. Sci.* 43: 606–30
Hirst, A. C. 1988. Slow instabilities in tropical ocean basin-global atmosphere models. *J. Atmos. Sci.* 45: 830–52
Houghton, J. T., Jenkins, G. J., Ephraums, J. J., eds. 1990. *Climate Change: The Intergovernmental Panel on Climate Change Scientific Assessment*. Cambridge: Univ. Cambridge Press. 364 pp.

Houghton, R. W., Tourre, Y. 1992. Characteristics of low frequency sea surface temperature fluctuations in the tropical Atlantic. *J. Climate* 5: 765–71

Inoue, M., O'Brien, J. J. 1984. A forecasting model for the onset of a major El Niño. *Mon. Weather Rev.* 112: 2326–37

Jensen, M. H., Bak, P., Bohr, T. 1984. Transition to chaos by interaction of resonances in dissipative systems. Part I. Circle maps. *Phys. Rev. A* 30: 1960–69

Jin, F.-F., Neelin, J. D. 1993a. Modes of interannual tropical ocean-atmosphere interaction—a unified view. Part I: numerical results. *J. Atmos. Sci.* 50: 3477–503

Jin, F.-F., Neelin, J. D. 1993b. Modes of interannual tropical ocean-atmosphere interaction—a unified view. Part III: analytical results in fully-coupled cases. *J. Atmos. Sci.* 50: 3523–40

Keppenne, C. L., Ghil, M. 1992. Adaptive filtering and prediction of the Southern Oscillation index. *J. Geophys. Res.* 97: 20,449–54

Kleeman, R. 1993. On the dependence of hindcast skill on ocean thermodynamics in a coupled ocean-atmosphere model. *J. Climate* In press

Kushnir, Y. 1993. Interdecadal variations in North Atlantic sea surface temperature and associated atmospheric conditions. *J. Climate* 6: In press

Kushnir, Y., Lau, N. C. 1992. The general circulation model response to a North Pacific SST anomaly: dependence on time scale and pattern polarity. *J. Climate* 4: 271–83

Lamb, P. J., Peppler, R. A., Hastenrath, S. 1986. Interannual variability in the tropical Atlantic. *Nature* 322: 238–40

Latif, M., Barnett, T. P., Cane, M. A., Flügel, M., Graham, N. E., et al. 1993c. A review of ENSO prediction studies. *Climate Dyn.* In press

Latif, M., Biercamp, J., von Storch, H. 1988. The response of a coupled ocean-atmosphere general circulation model to wind bursts. *J. Atmos. Sci.* 45: 964–79

Latif, M., Graham, N. E. 1992. How much predictive skill is contained in the thermal structure of an OGCM? *J. Phys. Oceanogr.* 22: 951–62

Latif, M., Sterl, A., Maier-Reimer, E., Junge, M. M. 1993a. Climate variability in a coupled GCM. Part I: the tropical Pacific. *J. Climate* 6: 5–21

Latif, M., Sterl, A., Maier-Reimer, E., Junge, M. M. 1993b. Structure and predictability of the El Niño/Southern Oscillation phenomenon in a coupled ocean-atmosphere general circulation model. *J. Climate* 6: 700–8

Latif, M., Villwock, A. 1990. Interannual variability as simulated in coupled ocean-atmosphere models. *J. Mar. Syst.* 1: 51–60

Lau, K. M. 1981a. Oscillations in a simple equatorial climate system. *J. Atmos. Sci.* 38: 248–61

Lau, N. C. 1981b. A diagnostic study of recurrent meteorological anomalies appearing in a 15-year simulation with a GFDL general circulation model. *Mon. Weather Rev.* 109: 2287–311

Lau, N. C. 1985. Modelling the seasonal dependence of the atmospheric response to observed El Niños in 1962–76. *Mon. Weather Rev.* 113: 1970–96

Lau, N. C., Nath, M. J. 1990. A general circulation model study of the atmospheric response to extratropical SST anomalies observed during 1950–79. *J. Climate* 3: 965–89

Lau, N. C., Philander, S. G. H., Nath, M. J. 1992. Simulation of El Niño/Southern Oscillation phenomena with a low-resolution coupled general circulation model of the global ocean and atmosphere. *J. Climate* 5: 284–307

Leetmaa, A., Ji, M. 1989. Operational hindcasting of the tropical Pacific. *Dyn. Atmos. Oceans* 13: 465–90

Lindzen, R. S., Nigam, S. 1987. On the role of sea surface temperature gradients in forcing low level winds and convergence in the tropics. *J. Atmos. Sci.* 44: 2418–36

Lough, J. M. 1986. Tropical Atlantic sea surface temperature and rainfall variations in Subsaharan Africa. *Mon. Weather Rev.* 114: 561–70

Luksch, U., von Storch, H., Maier-Reimer, E. 1990. Modeling North Pacific SST anomalies as a response to anomalous atmospheric forcing. *J. Mar. Systems* 1: 155–68

Manabe, S., Bryan, K. 1969. Climate calculations with a combined ocean-atmosphere model. *J. Atmos. Sci.* 26: 786–89

Manabe, S., Bryan, K., Spelman, M. J. 1975. A global ocean-atmosphere climate model. Part I: the atmospheric circulation. *J. Phys. Oceanogr.* 5: 3–29

Manabe, S., Bryan, K., Spelman, M. J. 1979. A global ocean-atmosphere climate model with seasonal variation for future studies of climate sensitivity. *Dyn. Atmos. Oceans* 3: 393–426

Manabe, S., Bryan, K., Spelman, M. J. 1990. Transient response of a global ocean-atmosphere model to a doubling of atmospheric carbon dioxide. *J. Phys. Oceanogr.* 20: 722–49

Manabe, S., Spelman, M. J., Stouffer, R. J. 1992. Transient responses of a coupled ocean-atmosphere model to gradual

changes of atmospheric CO_2. Part II: seasonal response. *J. Climate* 5: 105–26
Manabe, S., Stouffer, R. J. 1988. Two stable equilibria of a coupled ocean-atmosphere model. *J. Climate* 1: 841–66
Matsuno, T. 1966. Quasi-geostrophic motions in the equatorial area. *J. Meteorol. Soc. Jpn.* Ser. II 44: 25–43
McCreary, J. P. 1976. Eastern tropical ocean response to changing wind systems with application to El Niño. *J. Phys. Oceanogr.* 6: 632–45
McCreary, J. P. 1983. A model of tropical ocean-atmosphere interaction. *Mon. Weather Rev.* 111: 370–87
McCreary, J. P. 1985. Modeling equatorial ocean circulation. *Annu. Rev. Fluid Mech.* 17: 359–409
McCreary, J. P., Anderson, D. L. T. 1984. A simple model of El Niño and the Southern Oscillation. *Mon. Weather Rev.* 112: 934–46
McCreary J. P., Anderson D. L. T. 1991. An overview of coupled ocean-atmosphere models of El Niño and the Southern Oscillation. *J. Geophys. Res.* 96: 3125–50
McWilliams, J. C., Gent, P. R. 1978. A coupled air and sea model for the tropical Pacific. *J. Atmos. Sci.* 35: 962–89
Mechoso, C. R., Kitoh, A., Moorthi, S., Arakawa, A. 1987. Numerical simulations of the atmospheric response to a sea surface temperature anomaly over the equatorial eastern Pacific ocean. *Mon. Weather Rev.* 115: 2936–56
Mechoso, C. R., Ma, C.-C., Farrara, J. D., Spahr, J., Moore, R. W. 1993. Parallelization and distribution of a coupled atmosphere-ocean general circulation model. *Mon. Weather Rev.* In press
Meehl, G. A. 1990a. Development of global coupled ocean-atmosphere general circulation models. *Climate Dyn.* 5: 19–33
Meehl, G. A. 1990b. Seasonal cycle forcing of El Niño-Southern Oscillation in a global coupled ocean-atmosphere GCM. *J. Climate* 3: 72–98
Mikolajewicz, U., Maier-Reimer, E. 1990. Internal secular variability in an ocean general circulation model. *Climate Dyn.* 4: 145–56
Mitchell, J. F. B. 1989. The "greenhouse effect" and climate change. *Rev. Geophys.* 27: 115–39
Moore, D. W. 1968. *Planetary-gravity waves in an equatorial ocean.* PhD thesis. Harvard Univ. 207 pp.
Moore, D. W., Philander, S. G. H. 1978. Modeling of the tropical oceanic circulation. In *The Sea*, ed. E. D. Goldberg et al, 6: 319–61. New York: Wiley-Intersci.
Münnich, M., Cane, M. A., Zebiak, S. E. 1991. A study of self-excited oscillations in a tropical ocean-atmosphere system. Part II: nonlinear cases. *J. Atmos. Sci.* 48: 1238–48
Nagai, T., Tokioka, T., Endoh, M., Kitamura, Y. 1992. El Niño-Southern oscillation simulated in an MRI atmosphere-ocean coupled general circulation model. *J. Climate* 5: 1202–33
Namias, J. 1959. Recent seasonal interactions between North Pacific waters and the overlying atmospheric circulation. *J. Geophys. Res.* 64: 631–46
Neelin, J. D. 1989a. A note on the interpretation of the Gill model. *J. Atmos. Sci.* 46: 2466–68
Neelin, J. D. 1989b. Interannual oscillations in an ocean general circulation model coupled to a simple atmosphere model. *Phil. Trans. R. Soc. London Ser. A* 329: 189–205
Neelin, J. D. 1990. A hybrid coupled general circulation model for El Niño studies. *J. Atmos. Sci.* 47: 674–93
Neelin, J. D. 1991. The slow sea surface temperature mode and the fast-wave limit: analytic theory for tropical interannual oscillations and experiments in a hybrid coupled model. *J. Atmos. Sci.* 48: 584–606
Neelin, J. D., Held, I. M. 1987. Modelling tropical convergence based on the moist static energy budget. *Mon. Weather Rev.* 115: 3–12
Neelin, J. D., Jin, F.-F. 1993. Modes of interannual tropical ocean-atmosphere interaction—a unified view. Part II: analytical results in the weak-coupling limit. *J. Atmos. Sci.* 50: 3504–22
Neelin, J. D., Latif, M., Allaart, M. A. F., Cane, M. A., Cubasch, U., et al. 1992. Tropical air-sea interaction in general circulation models. *Climate Dyn.* 7: 73–104
Nihoul, J. C. J., ed. 1985. *Coupled Ocean-Atmosphere Models.* Amsterdam: Elsevier Oceanogr. Ser.
Nihoul, J. C. J., ed. 1990. *Coupled Ocean-Atmosphere Modeling.* Amsterdam: Elsevier. 313 pp.
Palmer, T. N., Mansfield, D. A. 1986. A study of wintertime circulation amomalies during past El Niño events using a high-resolution general circulation model. Part I: influence of model climatology. *Q. J. R. Meteorol. Soc.* 112: 613–38
Palmer, T. N., Sun, Z.-B. 1985. A modeling and observational study of the relationship of sea surface temperature in the northwestern Atlantic and the atmospheric general circulation. *Q. J. R. Meteorol. Soc.* 111: 947–75
Penland, C., Magorian, T. 1993. Prediction of Niño-3 sea surface temperatures using linear inverse modeling. *J. Climate* 6: 1067–76

Philander, S. G. H. 1981. The response of the equatorial oceans to a relaxation of the trade winds. *J. Phys. Oceanogr.* 11: 176–89

Philander, S. G. H. 1990. *El Niño, La Niña, and the Southern Oscillation.* San Diego: Academic. 293 pp.

Philander, S. G. H., Chao, Y. 1991. On the contrast between the seasonal cycles of the equatorial Atlantic and Pacific oceans. *J. Phys. Oceanogr.* 21: 1399–406

Philander, S. G. H., Lau, N. C., Pacanowski, R. C., Nath, M. J. 1989. Two different simulations of Southern Oscillation and El Niño with coupled ocean-atmosphere general circulation models. *Phil. Trans. R. Soc. London Ser. A* 329: 167–78

Philander, S. G. H., Pacanowski, R. C. 1980. The generation of equatorial currents. *J. Geophys. Res.* 85: 1123–36

Philander, S. G. H., Pacanowski, R. C. 1981. Response of the equatorial ocean to periodic forcing. *J. Geophys. Res.* 86: 1903–16

Philander, S. G. H., Pacanowski, R. C., Lau, N. C., Nath, M. J. 1992. Simulation of ENSO with a global atmospheric GCM coupled to a high-resolution, tropical Pacific ocean GCM. *J. Climate* 5: 308–29

Philander, S. G. H., Yamagata, T., Pacanowski, R. C. 1984. Unstable air-sea interactions in the tropics. *J. Atmos. Sci.* 41: 604–13

Pitcher, E. J., Blackmon, M. L., Bates, G. T., Muñoz, S. 1988. The effect of North Pacific sea surface temperature anomalies on the January climate of a general circulation model. *J. Atmos. Sci.* 45: 173–88

Rasmusson, E. M. 1984. El Niño: the ocean/atmosphere connection. *Oceanus* 27: 5–13

Rasmusson, E. M., Carpenter, T. H. 1982. Variations in tropical sea surface temperature and surface wind fields associated with the Southern Oscillation/El Niño. *Mon. Weather Rev.* 110: 354–84

Rasmusson, E. M., Wallace, J. M 1983. Meteorological aspects of El Niño/ Southern Oscillation. *Science* 222: 1195–202

Rasmusson, E. M., Wang, X., Ropelewski, C. F. 1990. The biennial component of ENSO variability. *J. Mar. Syst.* 1: 71–96

Ropelewski, C. F., Halpert, M. S., Wang, X. 1992. Observed tropospheric biennial variability and its relation to the Southern Oscillation. *J. Climate* 5: 594–614

Sausen, R., Barthels, K., Hasselmann, K. 1988. Coupled ocean-atmosphere models with flux correction. *Climate Dyn.* 2: 154–63

Schlesinger, M. E., ed. 1990. *Climate-Ocean Interaction.* Dordrecht: Kluwer. 385 pp.

Schlesinger, M. E., Gates, W. L., Han, Y. J. 1985. The role of the ocean in CO_2-induced climate change: preliminary results from the OSU coupled atmosphere-ocean general circulation model. See Nihoul 1985, 40: 447–78

Schopf, P. S., Cane, M. A. 1983. On equatorial dynamics, mixed layer physics and sea surface temperature. *J. Phys. Oceanogr.* 13: 917–35

Schopf, P. S., Suarez M. J. 1988. Vacillations in a coupled ocean-atmosphere model. *J. Atmos. Sci.* 45: 549–66

Schopf, P. S., Suarez, M. J. 1990. Ocean wave dynamics and the time scale of ENSO. *J. Phys. Oceanogr.* 20: 629–45

Seager, R., Zebiak, S. E., Cane, M. A. 1988. A model of the tropical Pacific sea surface temperature climatology. *J. Geophys. Res.* 93: 1265–80

Servain, J. 1991. Simple climatic indices for the tropical Atlantic Ocean and some applications. *J. Geophys. Res.* 96: 15137–46

Servain, J., Legler, D. M. 1986. Empirical orthogonal function analyses of tropical Atlantic sea surface temperature and wind stress: 1964–1979. *J. Geophys. Res.* 91: 14181–91

Shukla, J., Fennessey, M. J. 1988. Prediction of time-mean atmospheric circulation and rainfall: influence of Pacific sea surface temperature anomaly. *J. Atmos. Sci.* 45: 9–28

Shukla, J., Wallace, J. M. 1983. Numerical simulation of the atmospheric response to equatorial Pacific sea surface temperature anomalies. *J. Atmos. Sci.* 40: 1613–30

Sperber, K. R., Hameed, S. 1991. Southern Oscillation in the OSU coupled upper ocean-atmosphere GCM. *Climate Dyn.* 6: 83–97

Sperber, K. R., Hameed, S., Gates, W. L., Potter, G. L. 1987. Southern Oscillation simulated in a global climate model. *Nature* 329: 140–42

Stouffer, R. J., Manabe, S., Bryan, K. 1989. Interhemispheric asymmetry in climate response to a gradual increase of atmospheric CO_2. *Nature* 342: 660–62

Suarez, M. J., Schopf, P. S. 1988. A delayed action oscillator for ENSO. *J. Atmos. Sci.* 45: 3283–87

Tai, C. K., White, W. B., Pazan S. E. 1989. Geosat crossover analysis in the tropical Pacific. 2. Verification analysis of altimetric sea level maps with expendable bathythermograph and island sea level data. *J. Geophys. Res.* 94C: 897–908

Trenberth, K. E., ed. 1993. *Climate System Modeling.* New York: Cambridge Univ. Press. 817 pp.

Vallis, G. K., 1986: El Niño: a chaotic dynamical system? *Science* 232: 243–45
Vallis, G. K. 1988. Conceptual models of El Niño and the Southern Oscillation. *J. Geophys. Res.* 93C: 13,979–91
Wakata, Y., Sarachik, E. S. 1991. Unstable coupled atmosphere-ocean basin modes in the presence of a spatially varying basic state. *J. Atmos. Sci.* 48: 2060–77
Walker, G. T. 1923. Correlation in seasonal variations of weather, VIII: a preliminary study of world weather. *Mem. Indian Meteorol. Dep.* 24: 75–131
Wallace, J. M., Gutzler, D. S. 1981. Teleconnections in the potential height field during the Northern Hemisphere winter. *Mon. Weather Rev.* 109: 784–812
Wallace, J. M., Jiang, Q. 1987. On the observed structure of the interannual variability of the atmosphere/ocean climate system. In *Atmospheric and Oceanic Variability*, ed. H. Cattle, pp. 17–43. London: Roy. Meteorol. Soc.
Wallace, J. M., Smith, C., Jiang, Q. 1990. Spatial patterns of atmosphere-ocean interaction in the northern winter. *J. Climate* 3: 990–98
Washington, W. M., Meehl, G. A. 1989. Climate sensitivity due to increased CO_2: experiments with a coupled atmosphere and ocean general circulation model. *Climate Dyn.* 4: 1–38
Washington, W. M., Parkinson, C. L. 1986. *An Introduction to Three-Dimensional Climate Modeling*. Mill Valley, Calif: Univ. Sci. Books. 422 pp.
Washington, W. M., Semtner, A. J., Meehl, G. A., Knight, D. J., Mayer, T. A. 1980. A general circulation experiment with a coupled atmosphere, ocean and sea ice model. *J. Phys. Oceanogr.* 10: 1887–908
Weare, B., Navato, A., Newell, R. F. 1976. Empirical Orthogonal analysis of Pacific Ocean sea surface temperatures. *J. Phys. Oceanogr.* 6: 671–78
Weaver, A. J., Sarachik, E. S., Marotzke, J. 1991. Freshwater flux forcing of decadal and interdecadal oceanic variability. *Nature* 353: 836–38
Webster, P. J., Yang, S. 1992. Monsoon and ENSO: selectively interactive systems. *Q. J. R. Meteorol. Soc.* 118: 877–926
Wolter, K. 1989. Modes of tropical circulation, Southern Oscillation, and Sahel rainfall anomalies. *J. Climate* 8: 149–72
Xie, S.-P., Kubokawa, A., Hanawa, K. 1989. Oscillations with two feedback processes in a coupled ocean-atmosphere model. *J. Climate* 2: 946–64
Xu, J.-S., von Storch, H. 1990. Predicting the state of the Southern Oscillation using principal-oscillation-pattern analysis. *J. Climate* 3: 1316–29
Yamagata, T. 1985. Stability of a simple air-sea coupled model in the tropics. See Nihoul 1985, pp. 637–57
Yamagata, T., Masumoto, Y. 1989. A simple ocean-atmosphere coupled model for the origin of warm El Niño Southern Oscillation event. *Phil. Trans. R. Soc. London Ser. A* 329: 225–36
Yasunari, T., Seki, Y. 1992. Role of Asian monsoon on the interannual variability of the global climate system. *J. Meteorol. Soc. Jpn.* 70: 177–89
Zebiak, S. E. 1986. Atmospheric convergence feedback in a simple model for El Niño. *Mon. Weather Rev.* 114: 1263–71
Zebiak, S. E. 1989. On the 30–60 day oscillation and prediction of El Niño. *J. Climate* 2: 1381–87
Zebiak, S. E. 1993. Air-sea interaction in the equatorial Atlantic region. *J. Climate* 6: 1567–86
Zebiak, S. E., Cane, M. A. 1987. A model El Niño Southern Oscillation. *Mon. Weather Rev.* 115: 2262–78